Friedrich-Schiller-Universität Jena
Physikalisch-Astronomische Fakultät
Thüringer Landessternwarte Tautenburg

Extended Diffuse Radio Emission
in
Merging Galaxy Clusters

Dissertation

To fulfill the requirements for the Degree of
“doctor rerum naturalium” (Dr. rer. nat.)

Submitted to
the **Council of Faculty of Physics & Astronomy**
of the **Friedrich-Schiller-Universität Jena**

by **M.Sc. Cosmos Dumba**

born on **19.06.1981** in **Kyambogo, Uganda**

Name: Cosmos Dumba
Date of birth: 19th June 1981 in Kyambogo, Uganda
Matriculation Number: 155428

First Referee: Prof. Dr. Artie Hatzes
Thüringer Landessternwarte, Tautenburg, Germany
Second Referee: Prof. Dr. Marcus Brüggen
Universität Hamburg, Germany
Third Referee: Univ.-Prof. Dr. Sabine Schindler
Private Universität für Gesundheitswissenschaften,
Medizinische Informatik und Technik (UMIT), Austria
& Universität Innsbruck, Austria
Date of defense: 24.01.2019

Ehrenwörtliche Erklärung

Ich erkläre hiermit ehrenwörtlich, dass ich die vorliegende Arbeit selbständig, ohne unzulässige Hilfe Dritter und ohne Benutzung anderer als der angegebenen Hilfsmittel und Literatur angefertigt habe. Die aus anderen Quellen direkt oder indirekt übernommenen Daten und Konzepte sind unter Angabe der Quelle gekennzeichnet. Bei der Auswahl und Auswertung folgenden Materials haben mir die nachstehend aufgeführten Personen in der jeweils beschriebenen Weise unentgeltlich geholfen:

1. Dr. Matthias Hoeft – Betreuung der vorliegenden Arbeit
2. Dr. Timothy W. Shimwell – Bereitstellung der Daten der LOFAR HBA Beobachtung von Abell 1430
3. Dr. Alexander Drabent, Dr. Andreas Horneffer und Dr. David Rafferty – Unterstützung bei der Nutzung der LOFAR Software zur Kalibration der Daten

Weitere Personen waren an der inhaltlich-materiellen Erstellung der vorliegenden Arbeit nicht beteiligt. Insbesondere habe ich hierfür nicht die entgeltliche Hilfe von Vermittlungs- bzw. Beratungsdiensten (Promotionsberater oder andere Personen) in Anspruch genommen. Niemand hat von mir unmittelbar oder mittelbar geldwerte Leistungen für Arbeiten erhalten, die im Zusammenhang mit dem Inhalt der vorgelegten Dissertation stehen. Die Arbeit wurde bisher weder im In- noch im Ausland in gleicher oder ähnlicher Form einer anderen Prüfungsbehörde vorgelegt. Die geltende Promotionsordnung der Physikalisch-Astronomischen Fakultät ist mir bekannt. Ich versichere ehrenwörtlich, dass ich nach bestem Wissen die reine Wahrheit gesagt und nichts verschwiegen habe.

Ort, Datum	Unterschrift d. Verfassers
Jena, 25.09.2018	

"*The most energetic phenomena in the universe should also be the loudest. As radio astronomers, we listen carefully using gigantic radio telescopes; this helps us better understand what is going on in there.*"

Abstract

Galaxy clusters are the most massive gravitationally bound systems in the universe which grow through mergers with other clusters, galaxy groups, and accretion of gas. The mergers generate shocks and turbulence in the intra-cluster medium (ICM). Along the shock edges, particles are accelerated to relativistic energies through multiple crossings at the shock front. The extended diffuse emission sources formed as a result are commonly classified as radio halos and radio relics. The precise nature and origin of the relativistic particles is nevertheless not well understood.

We study the nature of the radio relic candidate in Abell 115. We obtain it's spectral properties using radio continuum observations at 150 MHz with LOFAR, 610 MHz with the GMRT, and 1.5 GHz with the VLA. We confirm it's nature as a radio relic. Polarization analyses suggest that part of the large scale synchrotron source is embedded in a region of high ICM density.

We show for the first time that the galaxy cluster A1430 hosts a two-component radio halo using radio continuum observations at 150 MHz with LOFAR. We obtain the spectral index of the radio halo and derive estimates of the radio power at 1.4 GHz. By comparing the surface brightness of the X-ray gas with the radio halo, we conclude that a part of the radio halo could be produced via turbulence and the rest lies in a region compressed by the merger via adiabatic compression.

Using a 100-m single dish radio telescope, we investigated the properties of radio synchroton sources in the galaxy clusters PSZ1-G108, Abell 746, 0809+39, and Abell 1367. We detected the polarised flux at 4.85 GHz in all the sources that were previously labelled as radio relics. The radio spectra of the integreted emission below 4.85 GHz can be well fitted with a single power law for all the radio relics. Polarisation observations of radio synchrotron sources not only confirm relic candidates, but also offer a method of measuring the strength and geometry of the shock front.

The discovery of the radio halo in Abell 1430 shows that the LOFAR Two-meter Sky Survey will help in the discovery of many more extended radio synchrotron sources. The single dish observations of the galaxy clusters PSZ1-G108, Abell 746, 0809+39, and Abell 1367 show that radio relics' spectral properties are well represented by a single power-law below 5GHz.

Zusammenfassung

Galaxienhaufen sind die massivsten gravitativ gebundenen Systeme im Universum. Sie wachsen durch Verschmelzung mit anderen Haufen oder mit Galaxiengruppen, sowie durch die Akkretion von Gas und dunkler Materie. Wenn Galaxienhaufen verschmelzen entstehen Stoßwellen und Turbulenz im Intra-Cluster-Medium (ICM). An den Stoßwellen können Elektronen und Protonen durch vielfaches Durchqueren der Front auf relativistische Energien beschleunigt werden. Auch die Turbulenz ist in der Lage Elektronen und Protonen auf relativistische Energien zu beschleunigen. Die so beschleunigten Elektronen sind eine Quelle von Synchrotronstrahlung.

Die Synchrotronstrahlung der in Folge von Verschmelzungen beschleunigten Elektronen wird als Radiorelikt bzw. als Radiohalo beobachtet. Röntgenbeobachtungen von Galaxienhaufen, in denen sich die Radiorelikte und Radiohalos befinden, zeigen, dass diese Cluster in der Regel sehr massiv sind. Für die meisten Galaxienhaufen mit einem Halo oder einem Relikt ist anhand der Verteilung der Röntgenemission auch der Vorgang des Verschmelzens klar zu erkennen. Viele Details des Vorgangs der Beschleunigung von Elektronen im Galaxienhaufen auf relativistische Energien sind jedoch noch unverstanden. In dieser Arbeit stellen wir Multifrequenzbeobachtungen von zwei Galaxienhaufen vor, von denen einer ein Radiorelikt und der andere ein Radiohalo aufweist. Ziel der Arbeit ist es, die Eigenschaften und den Ursprung solcher großräumiger Synchrotronemission besser zu verstehen.

Wir versuchen, die Natur der bekannten Radioemission in Abell 115 sicher festzulegen. Wir charakterisieren seine Spektralindex- und Polarisationseigenschaften. Um dies zu erreichen, analysierten wir Beobachtungen bei 150 MHz durchgeführt mit LOFAR, bei 610 MHz mit dem GMRT und bei 1,5 GHz mit dem VLA. Die Beobachtungen bei 1,5 GHz wurden im Vollpolarisationsmodus durchgeführt, um die Polarisationseigenschaften des Reliktes zu untersuchen. Wir bestätigen die Natur der großskaligen Quelle als Radiorelikt. Wir argumentieren, dass das Radiorelikt in A115 durch eine nicht-axiale Verschmelzung hervorgerufen wurde. Polarisationsanalysen deuten darauf hin, dass ein Teil der großräumigen Synchrotronemission in einer Region mit sehr geringer ICM-Dichte liegt.

Das Relikt und seine Ausrichtung passt zur Untersuchung von großräumigen Synchrotronquellen in weniger dichten Umgebungen von Galaxienhaufen. Bereits beantragt und bewilligte Breitbandbeobachtungen mit dem VLA bei 1,5 GHz werden es erlauben, die Polarisationseigenschaften des Relikts genauer zu untersuchen.

Wir zeigen auch zum ersten Mal, dass der Galaxienhaufen Abell 1430 ein Radiohalo mit mindestens zwei Komponenten beherbergt. Dazu haben wir mit LOFAR Kontinuumsmessungen bei 150 MHz durchgeführt und 1,5 GHz Archivdaten des VLA analysiert. Dies erlaubt den spektralen Index der Radioemission des Halos zu bestimmen. Wir schätzen die Radioleuchtkraft des Halos bei 1,4 GHz. Dies zeigt, dass frühere Untersuchungen nicht empfindlich genug waren, um den Halo zu erkennen. Durch den Vergleich der Oberflächenhelligkeit der Röntgenemission mit der Verteilung der Emission des Halos kommen wir zu dem Schluss, dass ein Teil des Radiohalos (A1430W) durch Turbulenz erzeugt werden kann. Der andere Teil befindet sich in der Region zwischen den Haufenzentren und wird durch die Verschmelzung der beiden Haufenteile gerade komprimiert.

Mit dem 100-m-Radioteleskop in Effelsberg untersuchten wir die Eigenschaften von Synchronquellen in den Galaxienhaufen PSZ1-G108, Abell 746, und Abell 1367, sowie der Quelle 0809+39. Wir haben polarisierten Fluss bei 4,85 GHz in allen Quellen entdeckt, die zuvor als Radiorelikte bezeichnet wurden. Die Radiospektren der integrierten Emission unter 4,85 GHz können mit einem Potenzgesetz für alle Radiorelikte gut beschrieben werden. Polarisationsbeobachtungen von Radiosynchrotronquellen bestätigen nicht nur Reliktkandidaten, sondern bieten auch eine Methode zur Messung der Stärke und Geometrie der Stoßfront.

Die Entdeckung des Radiohalos in Abell 1430 zeigt, dass mit dem LOFAR-Two-Metre-Sky-Survey die Entdeckung vieler weiterer zu erwarten ist. Die Beobachtungen der Quellen PSZ1-G108, Abell 746, 0809+39 und Abell 1367 mit Effelsberg zeigen, dass die spektralen Flussverteilung von Radiorelikten unterhalb von etwa 5 GHz durch ein einziges Potenzgesetz gut repräsentiert sind. Dies zeigt auch, dass Single-Dish-Teleskope gut geeignete Werkzeuge sind, um Reliktkandidaten zu bestätigen und nach neuen Reliktkandidaten zu suchen.

Acknowledgements

This work was made possible through the financial support of a stipend received from both the Deutsche Akademisher Austaushdienst and the Thüringer Landessternwarte, Tautenburg. I am especially indebted to Dr. Matthias Hoeft, my principle supervisor at TLS, and Prof. Dr. Artie Hartzes, Director of the Thüringer Landessternwarte, Tautenburg, who have been supportive throughout the whole period during my study in Germany. Your support has been vital in the completion of this work.

I am grateful to all those with whom I have had the pleasure to work with during my study at TLS, and to those with whom we have shared wonderful memories during my stay in Germany. Special thanks go to Dr. Alexander Drabent, Dr. Kamlesh Rajpurohit, Mr. Jakob Gelszinis, who as members of the radio astronomy group at TLS, worked hand in hand with me to make this a success. You read through my work, had the time to discuss with me some of my findings to make this work marvellous.

Nobody has been more important to me in the pursuit of this work than the dear members of my family. I thank my parents, whose unconditional love are with me in whatever good things I pursue. Most importantly, I wish to thank my loving and supportive wife, Flavia, and wonderful daughter Britta, who provide unending inspiration.

Low frequency radio analyses and the scientific conclusions drawn from them are based on observations made by the LOFAR telescope. LOFAR is designed, constructed and operated by ASTRON. The LOFAR data used in this work was in part processed on the Dutch national e-infrastructure with the support of SURF Cooperative through grant e-infra 160022 & 160152. The X-ray analyses and the scientific conclusions drawn from them are based on observations made by the *Chandra X-ray Observatory* which is operated by the Smithsonian Astrophysical Observatory on behalf of NASA.

Contents

List of Figures

List of Tables

List of Abbreviations

ACIS	Advanced CCD Imaging Spectrometer
AGN	Active Galactic Nuclei
ASCA	Advanced Satellite for Cosmology and Astrophysics
ASKAP	Australian Square Kilometer Array Pathfinder
ATCA	Australia Telescope Compact Array
AXAF	Advanced X-ray Astrophysics Facility
BCG	Brightest Cluster Galaxy
CASA	Common Astronomy Software Applications Package
CCD	Charge-Coupled Device
CDRLQs	Core-Dominated Radio Line Quasars
CMB(R)	Cosmic Microwave Background (Radiation)
CXC	Chandra X-Ray Center
DEC	Declination
DPPP	Default Pre-Processing Pipeline
ESA	European Space Agency
EMSS	Extended Medium Sensitivity Survey
EMU	Evolutionary Map of the Universe
ESO	European Southern Observatory
EVLA	Extended Very Large Array
FRG	First Ranked Galaxy
FWHM	Full Width at Half Maximum

GLOW	German Long Wavelength
GMRT	Giant Metrewave Radio Telescope
HBA	High-Band Antenna
HEASARC	High Energy Astrophysics Science Archive Center
HPBW	Half Power Beam Width
IC	Inverse-Compton
ICM	Intra-Cluster Medium
LAS	Largest Angular Scale
LBA	Low-Band Antenna
LLS	Largest Linear Size
LOFAR	LOw Frequency ARray
LOS	Line Of Sight
LoTSS	LOFAR Two-metre Sky Survey
MACS	MAssive Cluster Survey
MHD	Magnetohydrodynamics
MIT	Massachusetts Institute of Technology
NASA	National Aeronautics and Space Administration
NAT	Narrow Angle Tail galaxy
NORAS	Northern ROSAT All-Sky Survey
NRAO	National Radio Astronomy Observatory
NVSS	NRAO VLA Sky Survey
PKS	Parkes 2700-MHZ Survey
POSSUM	Polarisation Sky Survey of the Universes Magnetism
(P)SZ	(Planck) Sunyaev Zel'dovich
RA	Right Ascention
RASS	ROSAT All Sky Survey

REFLEX	ROSAT-ESO Flux Limited X-Ray
RFI	Radio Frequency Interference
RI	Radio Interferometry
RM	Rotation Measure
ROSAT	Röntgensatellit
SAO	Smithsonian Astrophysical Observatory
SB	Surface Brightness
SDP	Standard Default/Data Pipeline
SDSS	Sloan Digital Sky Survey
SKA	Square Kilometer Array
SMART	Stretch Mesh Attached to Rope Trusses
STScI	Space Telescope Science Institute
TB	Terabyte
TGSS	TIFR GMRT Sky Survey
TLS	Thüringer Landessternwarte
UV	Ultra Violet
VLA	Very Large Array
WENSS	Westerbork Northern Sky Survey
WSRT	Westerbork Synthesis Radio Telescope
XMM-Newton	X-ray Multi-Mirror Mission Newton

To Britta, Flavia & Teddy - *"Alle Guten Dinge sind Drei"*

Chapter 1

From Dark Matter Clumps to Merger Shocks & Turbulence

The study of radio emitting sources in galaxy clusters is one of the ways in which we can understand a variety of physical processes in galaxy clusters. With the appropriate theoretical framework, a better understanding of these physical processes can help us improve our measurements of the known contents in the clusters. For extended synchrotron emission, where the radio photons emanate from relativistic particles spiralling around magnetic field lines, we can study the properties of the magnetic field and the particle acceleration mechanisms (Vallee, 1990; Pfrommer and Dursi, 2010; Böhringer et al., 2016).

In this thesis, we study the properties of extended diffuse synchrotron sources using a telescope that is designed to operate at low frequencies, the LOw Frequency ARray (LOFAR) (van Haarlem et al., 2013). We complement our studies with observations from the Giant Meter-wave Radio Telescope (GMRT) at 610 MHz, and the Very Large Array (VLA) at 1.4 GHz. We also put to use observations of the fields in the X-ray and optical. X-ray observations reveal the nature of the intra-cluster medium (ICM); correlations with X-ray surface brightness help in understanding the origin of the diffuse synchrotron sources. Optical studies show the location of all member galaxies, their velocity distribution, and with deep observations, the Dark Matter (DM) distribution in the field.

This chapter will introduce to the reader the general composition of clusters of galaxies; concentrating on the intra-cluster medium (ICM) in more detail. We describe how the ICM is used to identify the dynamical state of a galaxy cluster. In addition, we expound on what radio emission in clusters of galaxies

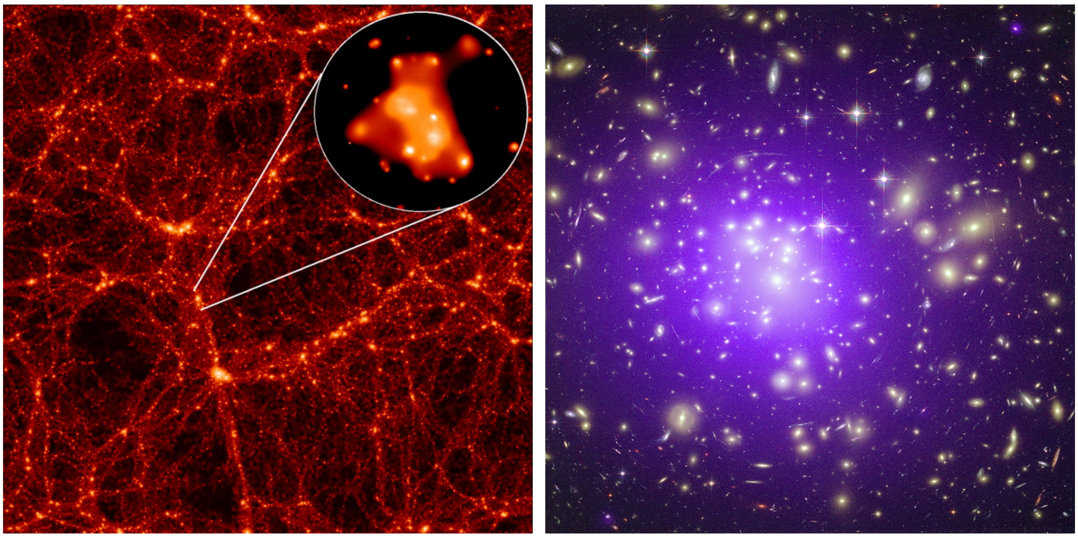

FIGURE 1.1: *Left:* XMM-Newton X-ray image of a galaxy cluster from the study is superimposed onto a simulation of a large volume of the Universe to illustrate the formation of galaxy clusters in the densest parts of the large scale universe. Credit: Virgo consortium; (Jenkins et al., 1998). *Right:* Abell 1689 in X-ray (blueish) and Optical (redish). Credit: X-ray: NASA/CXC/MIT ; Optical: NASA/STScI.

entails. Extended diffuse radio sources have been found to reside predominantly in massive merging galaxy clusters (see e.g., Feretti et al., 2012); therefore we discuss the theories that explain the production of relativistic particles in dynamically active galaxy clusters. The magnetic field strength being the key ingredient in the process of synchrotron radiation, we discuss magnetic fields in galaxy clusters and how the magnetic field strength is either measured or estimated.

1.1 Clusters of Galaxies

Galaxy clusters are the largest gravitationally bound structures in the universe hosting from a few tens to several hundreds of galaxies (Abell, 1958; Abell et al., 1989). They can grow through the in-fall of either smaller clusters into a larger one or by direct mergers of similarly sized clusters. They also grow through the accretion of gas and the infall of galaxies into the potential well of the dark matter halo.

In structure formation, galaxy clusters are the largest known gravitationally bound structures, making them good tools to use when probing cosmological parameters (e.g., the density parameter and the Hubble constant). Under the influence of gravity, structures will form when small perturbations in the primordial density distribution cause dark matter to become overdense in certain regions (Peebles, 1993). These are the regions in which galaxy clusters reside. A slice of the Millenium simulation (see fig. 1.1) shows the "nodes" where dark matter clumps and the "filaments" that connect these dark matter clumps (Springel et al., 2005). With the nodes acting as potential wells, the baryonic matter falls into such regions and thus forming galaxies and clusters of galaxies in the long run (Jenkins et al., 1998; Evrard and Gioia, 2002). The growth of these clumps results into gravitational attraction between the clumps themselves and consequently causing mergers between the galaxy clusters. These cluster mergers are the most energetic events in the observable universe. Considering the most massive clusters (which have masses of about a few $10^{15}\,\mathrm{M}_{\odot}$), the energy dissipated into the ICM during such an event is about $10^{63} - 10^{64}$ ergs.

Observationally, they can be seen as large (∼Mpc) concentrations of a hot X-ray emitting gas, an overdensity in the galaxy distribution, a large-scale alteration in the shape of background galaxies caused by a large-scale gravitational field, and as a Sunyaev-Zel'dovich decrement in the cosmic microwave background (CMB) signal (Sunyaev and Zel'dovich, 1972; Staniszewski et al., 2009).

The composition of matter in galaxy clusters is known to be as follows: Dark matter ($\sim 80\%$), the ICM ($\sim 15 - 17\%$), which is visible in X-rays (Byram et al., 1966; Gursky et al., 1971). The other $3 - 5\%$ is the baryonic matter in the stars and galaxies. This shows that most of the matter in galaxy clusters is invisible, i.e., dark matter. However, most of the information we have about the clusters is obtained from the visible (baryonic) matter because telescopes detect photons from/of the baryonic matter. The dark matter (non-baryonic) is only inferred from its gravitational interaction with matter. This emission radiated by the baryonic matter (X-ray gas and galaxies) can either be thermal or non-thermal in nature. It is termed thermal if the radiation is generated by the thermal motion of the charged particles in the matter and non-thermal if the radiation is given off by particles for reasons other than their thermal energy. For frequencies below a few GHz, synchrotron emission (where the radiation is due to charged particles spiralling around magnetic field lines at relativistic speeds) is described by

$$S_\nu \propto \nu^{-\alpha}, \tag{1.1}$$

where S_ν, ν, and α are the flux density, frequency and spectral index respectively.

We detect this radiation when observing with radio telescopes. This thesis will highlight a few aspects that improve our understanding of radio emission observed in galaxy clusters. We study two merging galaxy clusters: A1430, which hosts a two-component radio halo; A115, which hosts a large scale radio relic that resides in a low-ICM-density environment. It is for example not easy to explain why extended radio synchrotron sources are so rare in dense environments (see e.g., Vazza et al., 2012), how such sources can be found in poor clusters (see e.g., Subrahmanyan et al., 2003) and why the shocks traced by these sources are not found in some systems (see e.g., Ogrean et al., 2016).

1.2 The Intra-Cluster Medium (ICM)

The ICM is the baryonic component with the highest mass in a galaxy cluster since only about a tenth of the universe's baryons reside in stars and galaxies. X-ray telescopes are therefore very useful in identifying and studying galaxy clusters. This has indeed been demonstrated by the success of all-sky X-ray surveys like the *UHURU* sky survey (Giacconi et al., 1972), the Extended Medium Sensitivity Survey (EMSS) with the *Einstein Observatory* (Gioia et al., 1990), the *ROSAT* All-Sky Survey (RASS: Voges, 1992; Ebeling et al., 1996), the *ROSAT* follow up, the ROSAT-ESO Flux LimitEd X-ray (REFLEX) Survey (Böhringer et al., 2001), and the MAssive Cluster Survey (MACS: Ebeling et al., 2001).

In this framework, observations of clusters of galaxies in the X-ray play a significant role. Gursky et al. (1972) showed that galaxy clusters are the most extended luminous X-ray sources in the sky. The X-ray emission had already been interpreted as thermal bremsstrahlung from the hot ICM (Felten et al., 1966). The X-ray spectra reveal that the hot gas contains heavy elements which could have probably been injected there through supernovae explosions and/or galactic winds. The gas is heated by the conversion of the large potential energy during the infall of the gas into deep potential wells where clusters are forming. The large potential energy is converted into kinetic energy by compression, shocks and turbulent energy, which results in a substantial heating of the in-falling gas. The compressed gas forms an extended gaseous halo which fills the cluster volume. The expected typical temperature is given by

$$k_B T \simeq \mu m_p \sigma_v^2 \simeq 6 \left(\frac{\sigma_v}{10^3 \mathrm{km\,s^{-1}}} \right)^2 \mathrm{keV}, \tag{1.2}$$

where $\mu, m_p,$ and σ_v are the mean molecular weight, proton mass, and velocity dispersion.

Equation (1.2) implies that temperatures of $\sim 1 - 10\,\mathrm{keV}\,(10^7 - 10^8\,\mathrm{K})$, when the typical velocities of galaxies (in the range of 300 to $1,200\,\mathrm{km\,s^{-1}}$), are used. The thermal bremsstrahlung emissivity of such a hot plasma at frequency ν scales as

$$\epsilon_\nu \propto n_e n_i g(\nu, T) T^{-1/2} \exp\big(- h\nu / k_B T \big), \tag{1.3}$$

where n_e and n_i are the electron and ion number densities respectively, and $g(\nu, T)$ is the Gaunt factor[1]. Considering an astrophysical plasma dominated by hydrogen, such that $n_e \sim n_i$, and assuming that n_e is equal to the number of protons, n_p,

$$\epsilon_\nu \propto n_e n_i = n_p^2 = \rho_g^2. \tag{1.4}$$

The typical central electron density of the medium is low ($n_e \sim 10^{-3} - 10^{-1}\,\mathrm{cm^{-3}}$), making it an optically thin medium in the optical (Valentijn, 1979).

The overall electron density profile can be described by a radial profile called the β-*model*, which was introduced by Cavaliere and Fusco-Femiano (1976) as

$$\rho_g(r) = \rho_{g,0} \left[1 + \left(\frac{r}{r_c} \right)^2 \right]^{-3\beta/2}, \tag{1.5}$$

where β is the ratio of the specific kinetic energies of the galaxies and the gas; r and r_c are the radius and core radius of the distribution, respectively.

The X-ray surface brightness (SB) profile observed at the projected radius R, $S_X(R)$, is shown to be the projection on the sky of the plasma emissivity, ϵ_ν, as

$$S_X(R) = \int_R^\infty \frac{\epsilon_\nu dr^2}{\sqrt{(r^2 - R^2)}}, \tag{1.6}$$

Assuming isothermality and a β-model for the gas density (see eq. (1.5)), the surface brightness is described by Sarazin (1986) and Ettori (2000) as

---

[1] The Gaunt factor ranges from 1 to about 10 in the radio domain.

$$S_X(R) = S_X(0)\left[1 + \left(\frac{R}{r_c}\right)^2\right]^{-3\beta+0.5} \tag{1.7}$$

Studies of the X-ray morphologies of galaxy clusters have led to categorisation of the dynamical state of galaxy clusters: active, and relaxed (or sometimes called cooling core clusters (see e.g., Molendi and Pizzolato, 2001; Chen et al., 2007; Hudson et al., 2010)). Relaxed clusters are characterised by a sudden drop in electron temperature in the core where the density peaks. The temperature profile drops to $\sim$ 2.5 keV in the centre from $\sim$ 8.5 keV in the peripheral regions. A classic example of such a galaxy cluster is the Perseus cluster (Sanders et al., 2005). The active clusters on the other hand are those that exhibit signs of merging activity. One of the most striking example of such a cluster being the "Bullet cluster" 1ES 0657 − 55.8 (Tucker et al., 1998) with an average electron temperature of $kT = 17.4 \pm 2.5$ keV, the hottest known X-ray cluster to date. Clusters that are characterised by irregular morphologies and enhanced temperature regions; yet do not show enough evidence of ongoing merger activity are considered to have experienced a merger in the past; the only trace left is the morphology and enhanced temperature structure.

During merger events, the expectation is that the ICM halos of the sub-clusters interact and subsequently generate shock waves across the entire cluster region. As a consequence of this, some models predict that a fraction of the thermal electrons filling the volume will be accelerated and will therefore produce a population of relativistic electrons. This is called the "(re)acceleration scenario" or "primary electrons" model. Other models predict that the interaction of cosmic-ray protons with the thermal protons could produce a cascade of particles that could lead to the presence of relativistic particles (this is called the "secondary electrons" model). These ideas, together with others will be discussed in section 1.4. It is however worth noting that a key aspect to consider is the dynamics of the galaxy cluster. Parameters that are used to estimate how dynamically active a galaxy cluster is are thus first discussed in section 1.2.1.

---

[2] http://chandra.harvard.edu/photo/category/galaxyclusters.html

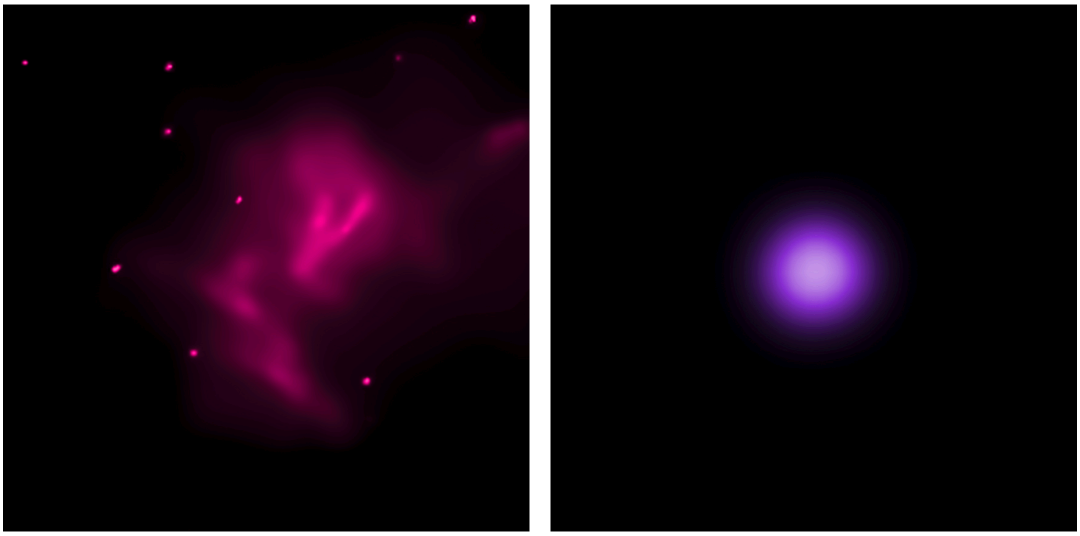

(a) MACS J0717 (b) Cl J1001

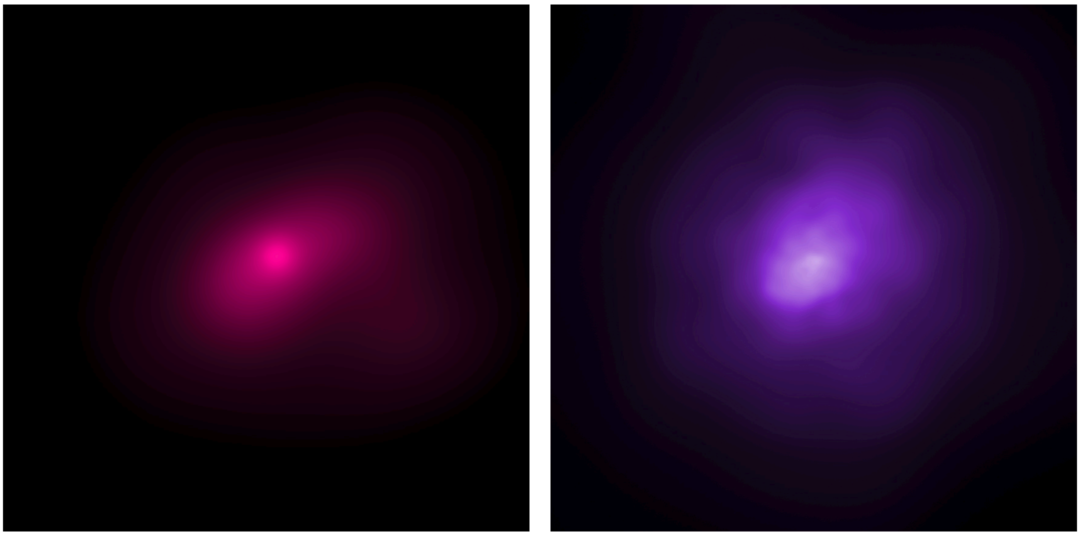

(c) MACS J0152 (d) ZwCl 3146

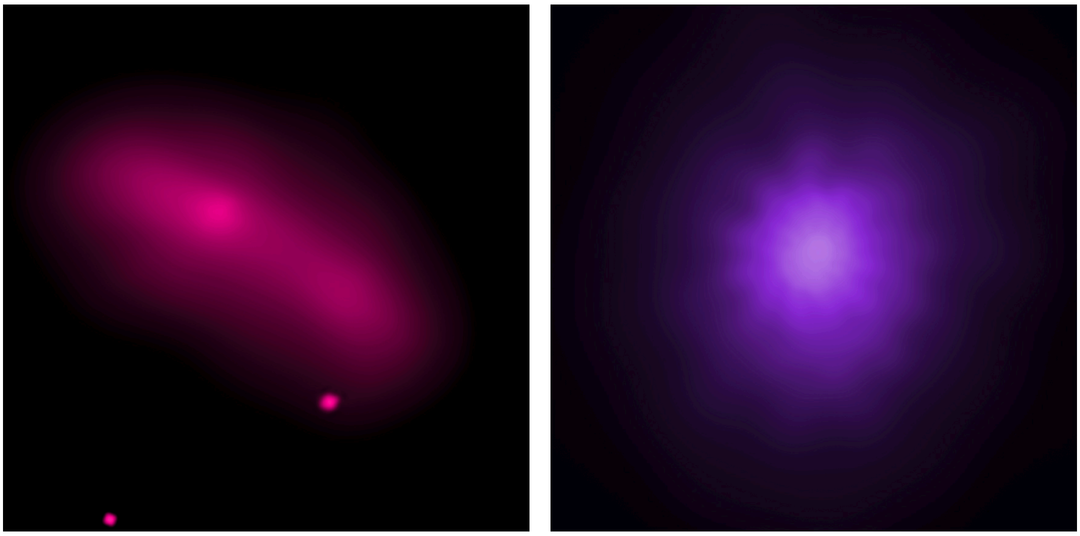

(e) MACS J0416 (f) A 1835

FIGURE 1.2: Disturbed (merging) on the left versus relaxed (cool core or non-merging) systems on the right. Credit: *Chandra* Frontier fields photo album[2].

1.2.1 X-ray morphological estimators

X-ray morphological estimators were established after a need to accurately characterise the dynamical state of galaxy clusters. An absence of substructure would indicate relaxed clusters while the presence of substructure indicates a disturbed system. Previous estimators were visual; optical images were compared with their corresponding X-ray images in order to identify substructures in the clusters (Baier et al., 1996; Kolokotronis et al., 2001). The approach would be slow with the forthcoming X-ray surveys in which several clusters would have to be observed in a short amount of time. The earlier quantitative X-ray morphological indicators were on the other hand used primarily by theorists who were testing cosmological models. They compared X-ray morphological measurements with those they obtained from hydrodynamical simulations of similar clusters (Mohr et al., 1995; Suwa et al., 2003). The precision needed by the estimators in order to match that of the surveys was still lacking. Rasia et al. (2013) discussed several high precision estimators that are still robust in classifying the dynamical state of galaxy clusters. Parekh et al. (2015) investigated these parameters further concluding that a combination of parameters is more useful when characterising the X-ray gas. A description of all parameters used is found in appendix A. In this work, we use the first three i.e the centroid shift, w, the light concentration, c, and the power ratios, P_i/P_0. These three parameters describe well all features of the X-ray gas.

1.3 Radio Emission in Galaxy Clusters

In the radio domain, galaxy clusters have a significant number of sources. They can either be galaxies or "patches of emission" that are not associated with any particular galaxy. The galaxies are either starburst galaxies or active galaxies. The active galaxies that are extended in the radio image are classified according to the Fanaroff-Riley (FR) scheme into FRI and FRII types (Fanaroff and Riley, 1974).

Radio galaxies come in a variety of types, from compact radio galaxies to extended radio galaxies, whose jets and lobes can extend up to distances of megaparsec scales. In order to classify a radio source as a radio galaxy, the detection of a bright optical galaxy close to the core or centre of the corresponding radio structure is required. When the emission of a radio galaxy in a galaxy cluster extends well beyond the optical boundaries of the host galaxy, it will interact with the ICM. Simulations show that the ICM is turbulent, filled with shocks and fast moving winds; they influence the morphology of the radio lobes. This means that the ICM can modify the shape of the radio lobes (e.g, by advection with the ICM), confining the radio lobes and sometimes fostering the feeding of the active nucleus of the galaxy. As a consequence, radio galaxies with long and bent radio lobes have been called tailed radio galaxies, a classical example of how the ICM interacts with the radio galaxies (Miley et al., 1972). The tailed radio galaxies are further classified depending on how wide the angle between the two tails is: Narrow Angle Tail (NAT) for a narrow angle and Wide Angle Tail (WAT) for a wide angle (Rudnick and Owen, 1976). The morphology is said to result from ram pressure confining the lobes as the fast moving galaxy falls deeper into the denser ICM.

Nonetheless, observations of galaxy clusters with radio telescopes have shown that there is some radio emission that is detected without any associated optical galaxy. Moreover, this radio emission is diffuse in nature making it more difficult to detect at higher radio frequencies. This type of emission is usually extended in size ($d \sim$ Mpc scale). The extent of this emission, coupled with a non-detection of a possible galaxy counterpart, suggests that the generation of this type of emission is instead related to the thermal (or non-thermal) plasma of the galaxy cluster. This type of emission is what we call extended diffuse radio emission (later classified as *radio relics* and *radio halos* depending on their properties). In this thesis, we shall highlight why observing at frequencies lower that 1.4 GHz is crucial in order to enrich studies of diffuse radio emission sources in galaxy clusters. We shall also show that observations at higher frequencies are still vital for particular study purposes.

1.4 Large Scale Diffuse Synchrotron Emission in Galaxy Clusters

The search for extended diffuse synchrotron emission has shown that only 30 percent of galaxy clusters host the large scale (Mpc in size) diffuse synchrotron emission that is not related to any particular galaxy (see e.g., Ferrari et al.,

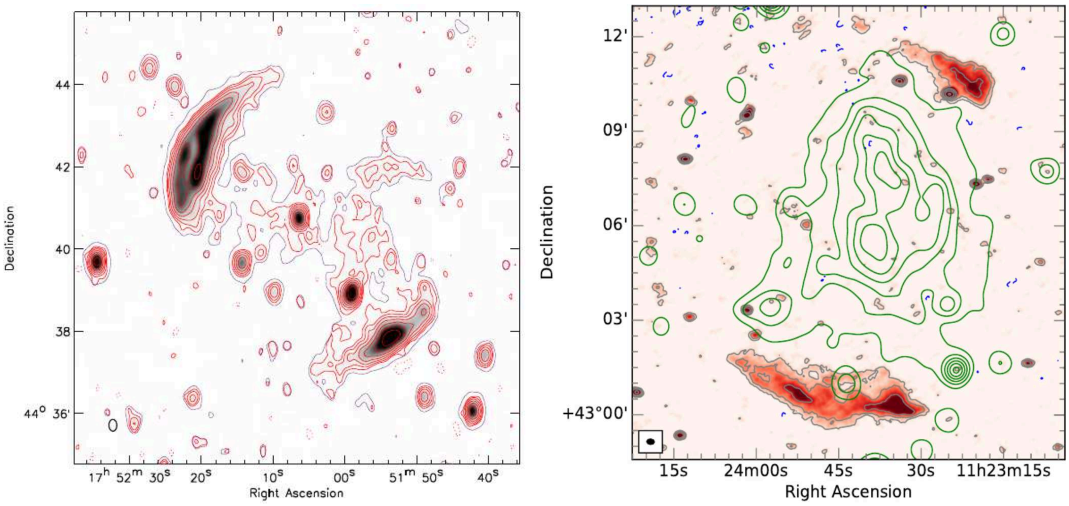

(a) MACS J1752.0 relics (van Weeren et al., 2012a) (b) A1240 double radio relics (Hoang et al., 2018)

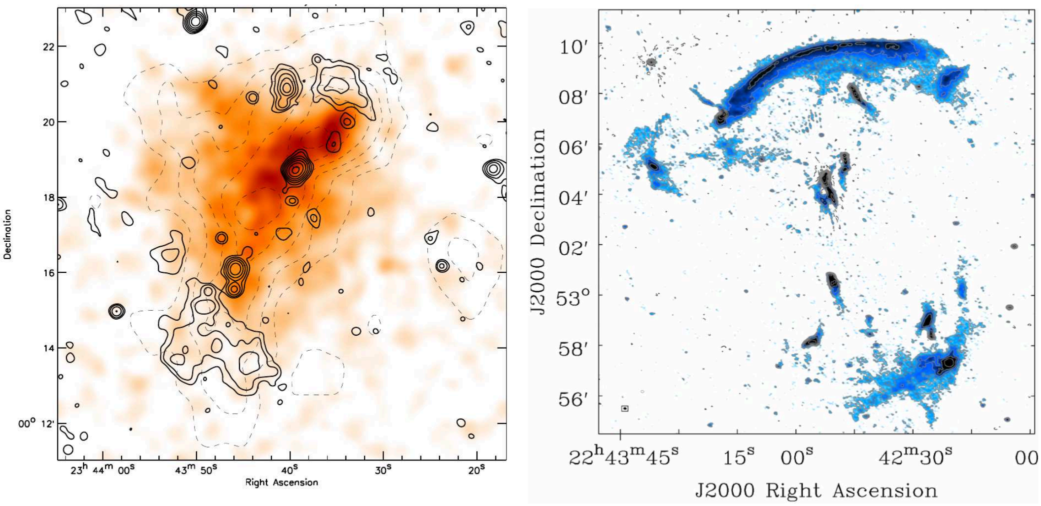

(c) ZwCl2341.1 double relics (van Weeren et al., 2009)) (d) The "*sausage*" relics (Hoang et al., 2017)

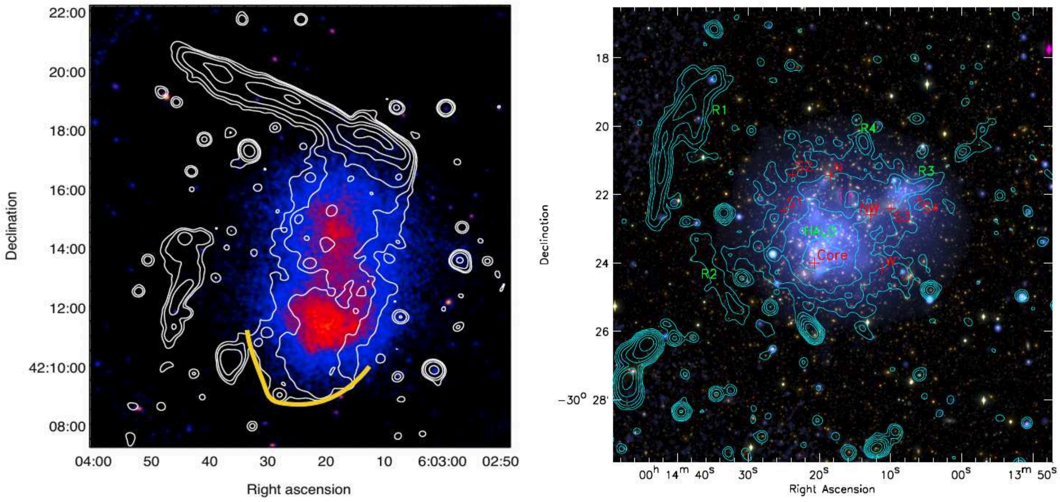

(e) The "*toothbrush*" relic (Rajpurohit et al., 2018) (f) A2744 radio halo and relic (Pearce et al., 2017)

FIGURE 1.3: Galaxy clusters hosting extended diffuse radio emission. Radio relics are seen in the peripheral regions of the cluster; radio halos, when present, are seen at the cluster centre (see e.g., the radio halos in (e) and (f)).

2008; Brüggen et al., 2012; Feretti et al., 2012). This fraction, though small, has led to the conclusion that relativistic electrons and weak magnetic fields ($B \sim \mu\mathrm{G}$) are present in the intra-cluster medium (ICM). Nonetheless, the source producing the relativistic particles that give rise to such large scale synchrotron emission is still debatable. This is due to the fact that it is challenging to explain how such large structures can form yet the radiative lifetime of the emitting electrons is relatively short. The short lifetime is, in part, due to synchrotron losses. Another factor is due to their interaction with the cosmic microwave background (CMB) relativistic photons.
For a medium of a few µG, the dominating process responsible for energy losses would be synchrotron emission. The lifetime of a relativistic electron[3] that loses energy via synchrotron emission can be, according to Longair (1981), approximated by:

$$\tau \approx \frac{2 \times 10^{12}}{\gamma[(1+z)^4 + \left(\frac{B}{3.3\,\mu\mathrm{G}}\right)^2]}\ \mathrm{yrs}\,. \tag{1.8}$$

This results in a short lifetime ($\tau \sim 10^8\,\mathrm{yrs}$, for $\gamma \sim 10^4$) meaning that the electrons are produced in-situ (locally everywhere) or/and if seed electrons in a region are (re-)accelerated to relativistic energies (Jaffe, 1977). The physical mechanisms that support the two ideas are different and generally result in different classes of sources. These sources generally have a low surface brightness and a steep spectral index distribution described by Equation 1.1 where $\alpha \leqslant -1.0$. The steep radio spectral index observed signifies that the emitting particles lose their energy faster. In some cases a steepening at higher frequencies is observed, which is a consequence of Compton-synchrotron losses[4].

These radio synchrotron sources (*radio relics & radio halos*) are found mainly in unrelaxed (sometimes called disturbed or merging) clusters, suggesting that cluster mergers play a vital role in their formation. Properties of the galaxy clusters in which most of the sources are located are key to understanding the physical process behind their production. Indeed, many studies have shown that mergers drive shocks and turbulence in the ICM which eventually lead to the amplification of the magnetic field and to the acceleration of highly-energetic

---

[3] In this case $\gamma < 10^8$

[4] This is the manifestation of a fact that the most energetic particles lose their energy faster than the least energetic ones.

particles (Dolag et al., 2002; Subramanian et al., 2006; Hoeft et al., 2008; Ryu et al., 2008). We describe in detail what radio halos are and the theories that explain their possible origin in 1.4.1. Radio relics and the theories that explain how such large scale synchrotron structures can be produced are described in section 1.4.2.

1.4.1 Radio Halos

Radio halos are extended low SB radio sources that are found in the central regions of galaxy clusters. The radio morphology for most halos is regular and traces that of the denser ICM. The first such object to be discovered was the radio halo in the Coma cluster (Peebles, 1970; Willson, 1970; Schlickeiser et al., 1987; Giovannini et al., 1993; Thierbach et al., 2003; Bonafede et al., 2010). Over 60 radio halos have now been discovered. In chapter 4, we report the discovery of yet another previously unknown radio halo. Figure 1.3 e & f show the radio halos in the *Toothbrush* and A2744 galaxy clusters. The images show how smooth the radio halo morphologies are and how they trace the ICM. Although the ICM is magnetic in nature, observations of radio halos have found very little ($\sim 5\%$) or no polarisation (Feretti et al., 1998; Bacchi et al., 2003). The only successful detections of polarised emission connected with a radio halo have been found in the galaxy clusters A2255 (Govoni et al., 2005; Pizzo et al., 2011) and MACS J0717.5+3745 (Bonafede et al., 2009). The general consensus is that radio halo emission is depolarised. The difficulty to detect and study halo emission in detail is due to their very low SB, steep spectra and large angular sizes.

The galaxy clusters that host radio halos are very few ($\sim 5\%$) if one considers only those not farther than $z = 0.2$ (Giovannini et al., 1999). Nevertheless, when one selects only massive galaxy clusters ($L_{\mathrm{X}} > 10^{45}\mathrm{erg\,s^{-1}}$), at the very least 30% of these galaxy clusters are found to host radio halos as shown from the GMRT Radio Halo Survey, in which a limited cluster sample was carefully studied (Venturi et al., 2007; Venturi et al., 2008; Kale et al., 2013). This fraction confirmed that the formation of radio halos detected so far depends on the cluster X-ray luminosity (Cassano et al., 2008). Indeed, it has been found that the halos in high X-ray luminous clusters have corresponding high radio luminosities (see e.g., Liang et al., 2000; Bacchi et al., 2003; Brunetti, 2006; Cassano et al., 2006; Brunetti et al., 2009; Rudnick and Lemmerman, 2009). This consequently explains the weak or no detection of radio halos with lower radio power by the current generation of radio telescopes.

Brunetti et al. (2009) compared the non-thermal radio power at 1.4 GHz ($P_{1.4\,\mathrm{GHz}}$) of all clusters hosting radio halos with their X-ray thermal luminosity and found that they lie on a tight correlation. However, when those from the GMRT radio halo survey that did not contain a radio halo are included, the scatter plot showed a clear separation, with the radio-quiet clusters falling below the correlation. This difference in the non-thermal properties between these clusters can be explained if we assume an evolutionary stage in which the radio-quiet clusters are the less massive systems that are in their early phase of merging where synchrotron emission is still increasing. The radio-loud clusters are the massive systems, with an on-going merger which is supplying energy to the relativistic electrons. Indeed, radio-quiet systems are typically less massive and more relaxed than their counterparts (see e.g., Venturi et al., 2008) and must have had their last major merger much earlier giving the relativistic electrons sufficient time to lose energy.

That being said, there have been a few cases where radio halos in under-luminous X-ray clusters have been found (see e.g., Giovannini et al., 2009; Brown et al., 2011; Giovannini et al., 2011).

Origin of Radio Halos

Radio halos are Mpc scale sized radio sources whose size plays a crucial role in understanding their origin. It is not possible to assume that the relativistic electrons that fill this whole volume are from the jets of radio galaxies. This is because the diffusion velocities in the ICM are driven by Alfven waves ($v_e \leq 100\,\mathrm{km\,s^{-1}}$)[5]. This therefore implies that the time required to diffuse through a $\sim$ Mpc distance in the cluster is approximately the Hubble time. This is much larger than the time the electrons have to radiate ($t \sim 10^8 - 10^9$ years). The models that have been developed to satisfy these conditions are:

---

[5] This is the group drift velocity.

(i) Turbulent Acceleration

This is the widely accepted model, also called the *primary model.* It postulates that the turbulence generated during cluster mergers amplifies the magnetic field strength to µG values increasing the efficiency with which the thermal electrons can be accelerated to relativistic (∼GeV) energies (see e.g., Jaffe, 1977; Harris, 1980; Schlickeiser et al., 1987; Tribble, 1993; Brunetti et al., 2001; Petrosian, 2001; Fujita et al., 2003). The acceleration of particles by turbulence is due to the resonant scattering of these particles by turbulent waves, which therefore lead to stochastic energisation of the electrons (see e.g., Brunetti et al., 2004; Lazarian, 2006; Brunetti and Lazarian, 2007).

Indeed, observations have shown that most of the radio halos observed so far reside in merging galaxy clusters. The dynamic state of the galaxy clusters is studied in X-ray where the X-ray thermal gas distributions for merging galaxy clusters is seen to be extremely disturbed (see fig. 1.2 (a), (b), and (c)). This is described quantitatively using parameters called X-ray morphological parameters as described in section 1.2.1. Indeed, Cassano et al. (2010) and Buote (2001) show that clusters that are morphologically disturbed are much more likely to host radio halos than those that are not.

Although a cluster merger can release energies of up to $10^{64}\mathrm{erg\,s^{-1}}$, Petrosian (2001) argue that the process by which this energy is used to reaccelerate thermal electrons is extremely inefficient. Thus, Brunetti et al. (2001) suggest that the process is done stepwise: first, an initial injection of relativistic seed electrons into the ICM, followed by the reacceleration of these seed electrons to relativistic energies.

(ii) $p-p$ Collisions

This is an alternative model that explains the existence of radio halos in galaxy clusters; it is sometimes called *secondary model.* This postulates that the electrons emitting in radio halos can be produced by the inelastic proton-proton collisions within the ICM. It was first proposed by Dennison (1980) and later rigorously developed by Blasi and Colafrancesco (1999). Due to the large diffusion time-scales of relativistic protons in the ICM, a pile-up is eminent, increasing the probability of having inelastic $p-p$ collisions between the relativistic protons and thermal protons. In turn, a continuous production of charged pions ($\pi^{\pm}$) and neutral pions (π^0) takes place. Dermer (1986) argue that these pions could then decay into secondary electrons and positrons radiating off γ rays as a consequence.

Indeed, many authors have considered these postulates in numerical simulations (see e.g., Dolag and Enßlin, 2000; Miniati et al., 2001; Pfrommer et al., 2008; Donnert et al., 2010). The production of secondary particles by $p-p$ collisions is described in Blasi and Colafrancesco (1999) as

$$\begin{aligned} p_{\rm CR} + p_{\rm ICM} &\to \pi^0 + \pi^+ + \pi^- + ... \\ \pi^0 &\to 2\gamma \\ \pi^{\pm} &\to \mu + \nu_{\mu} \\ \mu^{\pm} &\to e^{\pm} + \mu_{\nu} + \nu e. \end{aligned} \tag{1.9}$$

This interaction requires only a threshold energy of 300 MeV. It is expected that the protons in the cluster are accelerated to $E > 1$ TeV, and therefore the spectra of the relativistic electrons will have maximum energies of $E \geq 100$ GeV. This means that the resulting spectrum should follow a single power-law in the radio frequencies that we can access. However, spectral steepening has been observed in the spectra of some well studied radio halos (Thierbach et al., 2003; Dallacasa et al., 2009). In addition, we expect to find relativistic protons in all galaxy clusters implying that all galaxy clusters should host radio halos, which is not the case. Only a small fraction of galaxy clusters host radio halos (see e.g., Feretti et al., 2012; Kale et al., 2015). It is however noted that the *secondary-electron* model predictions are more challenging to be observed than those from the *primary-electron* model (Brunetti and Lazarian, 2011). For this, we need more sensitive radio observations of galaxy clusters to detect the emission from these secondary electrons. With the new generation telescopes (e.g., LOFAR, SKA, VLA), we expect to discover some of these faint sources.

The production of γ rays as another secondary consequence of the $p-p$ collisions has been another subject of scrutiny. Gamma ray observations of galaxy clusters have not yet been able to detect gamma rays, only managing to set upper limits (Reimer et al., 2003; Ackermann et al., 2010; Jeltema and Profumo, 2011). We therefore do not consider this scenario in our discussions.

1.4.2 Radio relics

In the context of large scale diffuse synchrotron sources in galaxy clusters, *radio relics* are those peculiar and elongated objects usually found in the outskirts of the galaxy clusters. Although some are arc-like in nature (e.g., the *sausage* relic (van Weeren et al., 2010; Stroe et al., 2013)), some are irregular in shape, roundish (e.g., in A1664: (Govoni et al., 2001)) while others have an orientation that is challenging to explain (see e.g., the *toothbrush* (van Weeren et al., 2012b; Rajpurohit et al., 2018)). Besides the morphology, they are characterised by a low surface brightness, a steep integrated spectral index ($\alpha \geq 1$), and a high degree of polarisation that can be up to 60% (see e.g., the *toothbrush* relic Kierdorf et al. (2017) and Rajpurohit (2018)). The sizes can vary with some clusters hosting multiple relics of varying sizes. Some clusters host double radio relics, located at opposite ends to each other (see e.g., A3667 (Rottgering et al., 1997; Johnston-Hollitt et al., 2002; Bonafede et al., 2009; Bonafede et al., 2012)) while others host radio relics and a radio halo (e.g., in A2256 (Clarke and Ensslin, 2006)). There are also a number of clusters that host double radio relics but do not have a radio halo (Bonafede et al., 2017). Their location and peculiar morphology suggests that they may be related to both minor or off-axis mergers as well as major-merger events. Indeed, relics are found in both merging systems and relaxed systems (see e.g., (Feretti et al., 2012)). The occurrence of radio relics in a sample from the NRAO[6] VLA Sky Survey (NVSS) showed that the fraction is higher in clusters with a high X-ray luminosity (Giovannini et al., 1999). It is also noted that galaxy clusters that host radio relics are predominantly merging galaxy clusters (Feretti et al., 2012).

Although Kempner et al. (2004) subdivided radio relics into three classes: *radio gischt, radio phoenices,* and *Active Galactic Nuclei (AGN) relics*, we use the term radio relics here to mean: (1) the *radio gischt* which are believed to be resulting from synchrotron emission from electrons (re-)accelerated in merger and/or accretion shocks (Ensslin and Biermann, 1998; Kang and Ryu, 2011) and (2) the *radio phoenices*, usually smaller structures (although they can also be large), believed to result from the re-acceleration of fossil plasma electrons via adiabatic compression (Enßlin and Gopal-Krishna, 2001; Enßlin and Brüggen, 2002). The fossil plasma could be from formerly active radio galaxies where the AGN creating the radio lobes has switched off. Examples of such radio relics are

---

[6] The NRAO is the National Radio Astronomy Observatory located in Charlottesville, Virginia (USA).

in the galaxy clusters A2443 (Cohen and Clarke, 2011), and A1033 (Gasperin et al., 2017).

Origin of Radio Relics

The origin of radio relics is currently attributed to shocks that travel outwards during and after a merger event. This has been shown by the discovery of radio relics in relaxed systems as well where minor or off-axis mergers take place. The presence of such shocks at the locations where radio relics are found has been shown by some X-ray observations via density and/or temperature jumps (Markevitch et al., 2002; Krivonos et al., 2003; Markevitch et al., 2005; Giacintucci et al., 2008; Russel, 2010; Finoguenov et al., 2010). However, radio relics are usually located in the cluster outskirts where the ICM density is very low. Akamatsu et al. (2011) show that the detection of shocks in the X-ray is very challenging when the ICM density is low. Indeed, the X-ray shock that is traced by the clear arc-shaped large scale radio relic, a text book example, the *sausage* relic, was only discovered recently (Akamatsu and Kawahara, 2013). In a review by Brüggen et al. (2012), only a few clear X-ray detections are reported.

The most widely accepted scenario that explains how such giant radio relics are produced entails the acceleration of particles in the shock regions. The elongated structure and the perpendicular alignment with a merger axis are in agreement with such a scenario. Smaller relics could however be produced via adiabatic compression of fossil plasma. The descriptions of these two scenarios are:

(i) Shock Acceleration

The theory that is used to explain a number of astrophysical shocks is the Diffusive Shock Acceleration (DSA) where particles are accelerated through shocks during cluster mergers (Krymskii, 1977; Drury, 1983; Blandford and Eichler, 1987). It is a first order Fermi process where the acceleration of electrons takes place across the shock. The electrons gain the energy by diffusing through the shock, bouncing off the two shock surfaces multiple times gaining energy (up to GeV) after each reflection (Blandford and Eichler, 1987; Jones and Ellison, 1991).

The shock Mach number can be derived from the power-law distribution that describes the relativistic momenta to which the shock has Fermi-accelerated the particles:

$$g(p) \propto p^{-\delta_{\text{inj}}}, \tag{1.10}$$

where $\delta_{\text{inj}} = \frac{3C}{C-1}$, C, the compression ratio described by the density jump as $C = \frac{\eta_{\text{down}}}{\eta_{\text{up}}}$. For a perfect gas, the canonical shock jump conditions will lead to an equation of the form:

$$\frac{1}{C} = \frac{\gamma_H - 1}{\gamma_H + 1} + \frac{2}{(\gamma_H + 1)M^2}, \tag{1.11}$$

where γ_H is a dimensionless measure of the specific heat ratio and M is the Mach number.

Combining eq. (1.10) and eq. (1.11) and assuming $\gamma_H = 5/3$ yields a relation between the particle injection index and the shock Mach number. This is given by

$$\delta_{\text{inj}} = \frac{4M^2}{M^2 - 1}. \tag{1.12}$$

The synchrotron radiation spectrum produced by the above population of electrons will have a spectral index described by

$$\alpha_{\text{inj}} = \frac{3}{2(C-1)} = -\frac{1}{2} + \frac{M^2+1}{M^2-1}. \tag{1.13}$$

The single power-law spectrum will then be given by the spectral index $\alpha_{\text{obs}} = \alpha_{\text{inj}} + 0.5$. We can therefore derive the expected shock Mach numbers with accurate spectral index measurements at hand.

Cosmological simulations have shown that the shocks are actually quite common in clusters (Vazza et al., 2009a; Vazza et al., 2009b), but are also relatively weak, with Mach numbers $M \sim 4$ (Ryu and Kang, 2003; Kang and Jones, 2007; Hoeft et al., 2008; Vazza et al., 2009a). Gabici and Blasi (2003) however show that $M \sim 3-4$ are sufficient to reproduce the observed radio relics. Kang and Ryu (2011) then showed that the low mach number shocks were rather not strong enough to accelerate thermal electrons to relativistic energies but needed to find an already existing pool of mildly relativistic electrons that could have been previously energised by a past merger activity. This fine tuning has led to a debate whether DSA is actually the process responsible for the origin of radio relics (Vazza and Brüggen, 2014; Vazza et al., 2015; Vazza et al., 2016)

(ii) Adiabatic Compression

Shocks can also adiabatically compress and trigger the re-energisation of relic plasma left behind by previously active galaxies (Enßlin and Gopal-Krishna, 2001; Enßlin and Brüggen, 2002). Indeed, simulations have shown that radio plasma cocoons that are filled with plasma are radio brightened when a shock passes through them (Slee et al., 2001). The degree of polarisation is also found to be relatively high in such scenarios, with the electric field vectors aligning perpendicularly to the shock surface. In such scenarios, we would expect the spectrum of the already aged plasma to be simply shifted to higher energies without modifying the slope. Observations of radio relics have indeed shown spectral index maps that are steepening downstream (see e.g., a review by Feretti et al. (2012) and for a most recent example in A1033 by Gasperin et al. (2017)).

Table 1.1: Observational properties of Halos, Relics, and mini-Halos

Type	Location	Size	α	Polarisation	Example
Halo	Central	$\geq$ Mpc	≥ 1.0	$< 5\%$	A2744, A2255, Coma
Relic	Periphery	$\sim$Mpc	≥ 1.0	$10 - 50\%$	A1240, ZwCl 2341.1, *toothbrush*
mini-Halo	Central	≤ 0.5 Mpc	≥ 1.0	No	Perseus, A2626, PKS 0745-191

1.4.3 Radio mini-halos

Unlike radio halos, mini-halos are much smaller in size ($d \sim 100 - 500\,\text{kpc}$) and located at the centre of cooling core clusters. Cooling core clusters are relaxed systems implying that mini-halos are not associated with merging clusters. Typical examples are like in the Perseus cluster (Sijbring, 1993), Virgo cluster (Owen et al., 2000), A2626 (Gitti et al., 2004), and PKS 0745-191 (Baum and O'Dea, 1991). Nonetheless, there are also peculiar examples where merger activity is observed (see e.g., A2142: Markevitch et al. (2000)). Most mini halos surround a powerful radio galaxy but the example in A2142 does not have one making some considering it a *small halo*. The presence of a powerful radio galaxy raised arguments about its role in the formation of mini-halos. Gitti et al. (2002) argued that they are not connected to the central radio galaxy in terms of particle diffusion but are instead associated with the ICM in the cooling flow region. Indeed, the radio power of mini-halos is correlated with the cooling flow power (Gitti et al., 2004)

Origin of radio mini-halos

The current models that explain the existence of mini-halos are similar to those for radio halos. One idea is that the primary electrons are undergoing re-acceleration continuously due to MHD turbulence triggered by the cooling flow region (Gitti et al., 2002). Another idea is that the relativistic electrons are of secondary origin and are thus produced by the interaction of cosmic ray protons with the ambient thermal protons (Pfrommer and Enßlin, 2004). Observations favour the electron re-acceleration model when the spectral behaviour is studied (see e.g., the Perseus mini-halo (Sijbring, 1993)). The models predict a spectral steepening radially and at high frequencies. Nevertheless, the number of mini-halos studied is still low making it difficult to draw conclusions (Feretti et al., 2012).

1.5 Magnetic Fields in Galaxy Clusters

The large scale synchrotron sources in galaxy clusters (*radio halos* and *radio relics*) are attributed to the presence of large-scale magnetic fields that are distributed throughout the cluster ICM. The radiative lifetime of the high energy electrons is proportional to $1B^2$ where B is the magnetic field strength, making the magnetic field strength a key parameter whose precise understanding and measurement are vital. This makes it easier to constrain the properties of the relativistic electrons in clusters. There are a few methods used to measure and/or estimate the magnetic field strength.

1.5.1 Equipartition Magnetic Field

One argument that is used to estimate the strength of the magnetic field is the equipartition of energy. It postulates that the cosmic ray energy density when equal to the magnetic energy density yields volume-averaged field strengths of $B \sim 0.1 - 1$µG (Govoni and Feretti, 2004). This is based on the assumption that in a synchrotron source, the total energy is given by the energy of the relativistic particles (U_e for electrons and U_p for protons) plus the magnetic field energy (U_B),

$$U_{\rm total} = U_e + U_p + U_B. \tag{1.14}$$

The total magnetic energy U_B is given by

$$U_B = \int_V u_D dV \equiv \frac{B^2}{8\pi}\Phi V, \tag{1.15}$$

where Φ defines the fraction of the source volume occupied by the magnetic field.

The energy contained in the electrons, U_e, can be expressed as a function of the synchrotron luminosity, L_{syn}, by

$$U_e = f(\alpha, \nu_1, \nu_2) L_{syn} B^{-3/2}, \tag{1.16}$$

where $f(\alpha, \nu_1, \nu_2) = \left(\frac{2\alpha-2}{2\alpha-1}\right)\frac{\nu_1^{(1-2\alpha)/2} - \nu_2^{(1-2\alpha)/2}}{\nu_1^{(1-\alpha)} - \nu_2^{(1-\alpha)}}$, a factor computed for a particular spectral index value and between frequencies ν_1 & ν_2.

The energy contained in the protons, U_p, can be related to that contained in the electrons, U_e, by $U_p = kU_e$, where k is a factor ranging between 0 and 1.

The condition for the minimum energy is obtained when the contributions of the magnetic field and relativistic particles are approximately equal, i.e

$$U_B = \frac{3}{4}(1+k)U_e. \tag{1.17}$$

The minimum energy is known as the equipartition value for this reason. We therefore derive a magnetic field value for which the total energy is at its minimum. The magnetic field value obtained is therefore called the *equipartition magnetic field.*

To obtain the *equipartition magnetic field* using observables, we express the total minimum energy $U_{\rm min} = \frac{U_{\rm min}}{V\Phi}\,{\rm erg\,cm^{-3}}$ after assuming $\Phi = 1$, the same volume of particles and the magnetic field, and applying the $\rm k-correction$ as

$$u_{\rm min} = f(\alpha, \nu_1, \nu_2) \cdot (1+k)^{\frac{4}{7}} (\nu_0)^{\frac{4\alpha}{7}} (1+z)^{\frac{(12+4\alpha)}{7}} I_0^{\frac{4}{7}} d^{\frac{-4}{7}}\ {\rm erg\,cm^{-3}}, \tag{1.18}$$

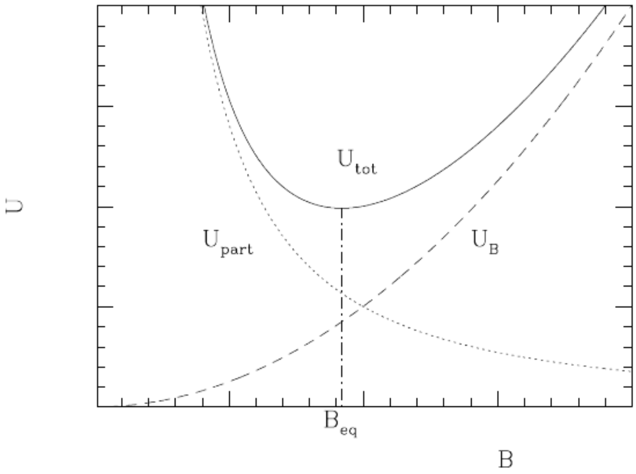

FIGURE 1.4: Trend of the energy content in a synchrotron radio source (in arbitrary units). The magnetic field energy, $U_B \propto B^2$, while the energy density in the relativistic particles (protons and electrons), $U_{\rm part} = U{\rm e} + U{\rm p} \propto {\rm B}^{-3/2}$. The equipartition magnetic field, $B_{\rm eq}$ is the magnetic field when the total energy, $U_{\rm tot}$, is minimum.

where the factor at the front is computed for the value of α.

For $\alpha = 0.7, \nu_1 = 10\,{\rm MHz}, {\rm and}\, \nu_2 = 100\,{\rm GHz}$, the factor is given by

$$f(\alpha, \nu_1, \nu_2) = 1.23 \times 10^{-12}. \tag{1.19}$$

The k values assumed for clusters are $k = 0\,({\rm or}\, k = 1)$. The magnetic field at which this minimum value of the total energy content is obtained is then derived from

$$B_{eq} = \left(\frac{24\pi}{7} u_{\rm min}\right)^{\frac{1}{2}} \ {\rm erg}^{\frac{1}{2}}\ {\rm cm}^{-\frac{3}{2}}. \tag{1.20}$$

It should be noted here that there are several assumptions involved in this estimate. For example, if the population of relativistic electrons is not in equilibrium, the assumption of minimum energy itself will not be valid. The ratio of relativistic electron energy to proton energy is uncertain since direct measurements of relativistic protons are difficult. The volume filling factor Φ is also uncertain since studies of the magnetic field in galaxy clusters are challenging.

Values of the magnetic field strength estimate obtained using the equipartition argument are lower than those obtained through Faraday rotation measures (see e.g., Feretti et al., 1995; Beck et al., 2003; Thierbach et al., 2003).

1.5.2 Faraday Rotation Measure

Another way is to study the radio emission of radio galaxies that reside in or behind the cluster. The rotation of the electro-magnetic vectors of the polarised emission is used to infer the strength of the magnetic field for a known ICM density through a process called Faraday rotation measure. This is the tendency of the plane of linearly polarised light travelling through a magneto-ionic medium (e.g., the ICM) to be rotated by an amount ($\Delta_\chi = RM\lambda^2$) that is proportional to the strength of the magnetic field along the line of sight and the gas density. We then define the "Faraday Rotation Measure" (RM) as

$$RM = \frac{e^2}{2\pi m_e^2 c^4} \int_0^L n_e \vec{B} \cdot \mathrm{d}\vec{l}, \tag{1.21}$$

which is written numerically as,

$$RM = 812 \int_0^L n_e B_\parallel \cdot \mathrm{d}\vec{l} \, \mathrm{rad\,m^{-2}}, \tag{1.22}$$

where n_e & B are in units of cm^{-3} and µG respectively while l is in kpc.

The RMs of these galaxies are measured at different frequencies and used to infer the average magnetic field of the galaxy cluster once the contribution from our Galaxy is subtracted.

Equation 1.22 is then used to obtain the magnetic field distribution of the whole cluster region using a set of galaxies at multiple locations assuming a density profile $n_e(r)$. The RMs of each galaxy will provide the magnetic field strength in the local region. The inferred magnetic fields from RMs are typically 1-10 µG for merging galaxy clusters and 10-40 µG for relaxed clusters (see e.g., Kim et al., 1991; Carilli and Taylor, 2002; Govoni and Feretti, 2004). This however raises the possibility that galaxies deep in the ICM are probing only local field strength and not that of the bulk of the ICM. Carilli and Taylor (2002) avoid this issue by using only background galaxies whose line of sight incorporates the bulk of the ICM. However, only a handful of clusters have a set of background radio galaxies whose RMs have been measured (Kim et al., 1990; Clarke et al., 2001).

Nevertheless, one well studied example can provide reliable estimates with which a few models can be tested. Dolag et al. (2001) show from simulations that the magnetic field strength is roughly symmetrical in the cluster tracing gas density along radial lines from the cluster centroid. A well studied example in this case is the Coma cluster where multiple RMs of cluster members have been obtained. The field strength is inferred to be that that peaks at the centre of the cluster at 4.7 µG falling off as $n_{th}^{0.5}$, n_{th} being the ICM distribution as measured in the X-ray (Bonafede et al., 2010). From this analogy, the magnetic field model can be inferred to other clusters where RM studies are not yet or cannot be performed (Vacca et al., 2012). The inferred magnetic field strengths are however lower than expected and do not match the observed level of synchrotron radiation (Jeltema and Fermi LAT Collaboration, 2010; Brunetti et al., 2012).

1.5.3 Synchrotron/Inverse-Compton Flux Ratio

It is suggested that the non-thermal hard X-ray emission observed in several galaxy clusters is due to IC emission from the same relativistic electrons responsible for the radio halos. In this case, the ratio between the radio emission flux and that from the hard X-ray emission can be used to estimate the magnetic field strength by

$$\frac{b_{sync}}{b_{IC}} = \frac{U_B}{U_{CMB}} \approx 0.095(1+z)^4\left(\frac{B}{1\mu\text{G}}\right)^2. \tag{1.23}$$

Although this method is the most unbiased, we lack a good knowledge of the hard X-ray emission. A well-studied example where this method has been used is the Coma cluster where a magnetic field strength $B \sim 0.15\,\mu$G is obtained (Fusco-Femiano et al., 1999). The value is an order of magnitude lower than that obtained using Faraday rotation measure.

1.6 This thesis

Radio halos and radio relics are still poorly understood. Although about 100 radio halos and radio relics have been detected to date, a lot more were expected from the large scale surveys that were conducted to detect them. For the NVSS, the biggest shortfall is believed to have been the lack of short-spacings in the D-configuration, making the sensitivity to emission larger than 15′ poor. For low redshift sources, the angular size for a Mpc sized object will be very large (e.g., for $z = 0.1, \mathrm{LAS}(\theta_\mathrm{b}) \sim 10')$[7]. The Coma cluster ($z = 0.02$) hosts a giant radio

---

[7] LAS is the linear angular scale

halo that was not visible in the NVSS due to this reason. A secondary reason for the shortfall comes from the primary model that describes the formation of radio halos. A steepening of the radio spectrum at higher frequencies is expected, making it possible that synchrotron sources were simply missed (Dallacasa et al., 2009). We therefore utilise the LOFAR telescope, especially the LoTSS survey, in which a large fraction of previously undetectable sources are detectable. In addition, the spectra of radio halos at lower frequencies is poorly known. Only a few sources have been studied in detail with multi-frequency observations (Feretti et al., 2012). We therefore observed a radio relic and a radio halo at LOFAR frequencies to study these two unique synchrotron sources in detail.

We discuss the multi-frequency observations of the radio relic in the galaxy cluster A115 in chapter 3. The relic morphology is inclined in a way similar to that of the *toothbrush* (see e.g., Rajpurohit et al., 2018), making it a useful site for studying the magnetic field in galaxy clusters. The close proximity of a very bright 3C source in the field also helps us show how high-dynamic range imaging is crucial in order to study the radio sky in detail.

A new discovery of a giant radio halo in the merging galaxy cluster A1430 is presented in chapter 4. This discovery highlights how low frequency studies are vital in improving our understanding synchrotron radio sources at lower frequencies. From this study, we highlight the importance of observing merging clusters at low frequencies.

Cassano et al. (2010) predicted that the *Tier 1* LOFAR Sky Survey (LoTSS) will discover about 350 giant radio halos at a redshift below 0.6 and that half of them are not visible at high frequencies since they are steep spectrum sources. This has not been achieved yet in the current discoveries. One possibility could be that minor mergers are either not as common as previously thought or cannot produce bright enough synchrotron sources. This means that the current radio halos and relics are reproduced by only the most extreme and energetic mergers. These cases can be studied not only at the low frequency regime but also at higher frequencies, since the sources should still be bright at these frequencies. Since the spectra of such sources is expected to have a cut off at higher frequencies, high frequency studies are useful in understanding the physics of such events. We therefore plan to use high frequency studies to test model predictions and shed more light on the origin of radio halos and radio relics. For this, four galaxy clusters, A746, A1367, PSZ1-G108+39, and 0809+39 have been observed using the *Effelsberg* 100 m single dish radio telescope. An overview of the sample is written in chapter 5.

Chapter 2

Telescopes Used and their Data Reduction Processes

Radio telescopes are used to receive the faint radio emission emitted by extraterrestrial radio sources. Although radio telescopes are of various shapes and sizes, they primarily consist of an antenna system and a sensitive receiver that amplifies the signal to a measurable quantity. The design of a radio telescope is often influenced by the wavelength range of scientific pursuit. This is because the telescope reflecting surface has to meet the minimum requirements for the proper reflection of the waves (see e.g., Legg, 1998; Yang et al., 2003). This is noticeable in the designs of telescopes that are used to receive mm wavelength signals. These telescopes consist of dishes that are much more polished than those that are used to receive cm wavelength signals. However, at meter wavelengths, the telescope reflecting surfaces are often wire-meshed since that is polished enough for waves of a few meters in wavelength to be reflected. This reduces the construction costs significantly (see e.g., Kraus, 1956).

The signals received by a telescope are used to obtain information about the observed view-able field and the sources therein. In order to study the observed field in clear detail, one vital property of any telescope is its resolution, how much fine detail it can resolve in the field (see e.g., Harrower, 1962). This property is described using

$$\theta(\text{radians}) \propto \frac{\lambda}{\mathrm{D}}, \tag{2.1}$$

where λ is the wavelength of the wave in meters and D is the diameter of the reflector in meters.

Equation 2.1 shows that an increase in the wavelength of the wave, λ, necessitates an increase in the diameter of the reflector as well, in order to maintain the same resolution. This angular resolution is important in order to be able to discretise particular features in an observed object and thus is important for imaging. When θ is expressed in arcseconds, equation 2.1[1] becomes,

$$\theta(\text{arcseconds}) = \frac{2.1 \times 10^5 \lambda}{\text{D}}. \tag{2.2}$$

This means that a human eye, which operates at visible light of $\sim 580\,\text{nm}$, and whose lens' aperture diameter ranges from $2 \sim 8\,\text{mm}$ (depending on the time of the day), has an angular resolution of about 17 seconds of arc. In order for a single dish radio telescope operating at 21 cm (1.4 GHz) to have a similar resolution as that of the eye, the dish diameter should be 2.5 km. At a wavelength of about 2 m (150 MHz), the diameter of the dish should be 24 km, which is technically unachievable. One of the largest and fully steerable single dish radio telescopes, the Effelsberg radio telescope in Bonn, Germany, has a diameter of 100 m. This means that for the 21 cm (1.4 GHz) receiver, the angular resolution is $\sim$ 440 arcseconds. This telescope can only resolve sources larger than this value. This lack of high resolution for even the largest radio telescopes in the world is compensated by using interferometers. These are arrays of multiple antennas whose signals are combined to mimic a single dish telescope whose reflector diameter is equivalent to the separation of the individual antennas of the array. This chapter will describe how a simple interferometer works, and how vital interferometers are for high resolution observations. The interferometers whose data we obtained shall also be described in this chapter under section 2.1. Since each radio telescope has specific details on how to calibrate its data, we describe how the data obtained from each of the telescopes that we used is calibrated, in sections 2.2 and 2.3.

2.1 Radio Interferometric Telescopes (Arrays)

The concept of radio interferometers was developed in order to allow radio telescopes achieve a resolution high enough for studies of structures with

---

[1] 1 radian = 206265 arcsecs

Band	ν (GHz)
4	0.074
P	0.35
L	1.5
S	3.0
C	6.0
X	10.0
Ku	15.0
K	22.0
Ka	33.0
Q	45.0

TABLE 2.1: A closer look at the VLA dishes (left); VLA receiver bands with their corresponding central frequencies (right). Image Credit: Alex Savello

arcsecond and sub-arcsecond scales. This makes it possible to study sources like galaxies and molecular clouds in detail. The principle of operation is similar to that of equation 2.1, alterating the diameter to denote a baseline, the distance between two individual antennas. The equation, in a simplified form, is written as

$$\theta(\text{radians}) \propto \frac{\lambda}{\mathrm{B}}, \tag{2.3}$$

where B is the separation of two individual telescope antennas. The larger the separation, B, the smaller the angular resolution, θ becomes. In principle, most arrays have more than two antennas, from around 8 to 30 antennas arranged in a pattern with which the various baselines can fill the visibility plane as the earth rotates. We have obtained data from three interferometric radio telescopes that operate at different wavelengths. Although the principle of operation of an interferometer is the same for all, their designs are different. A brief description of these radio telescopes is given in the following sections: Section 2.1.1 for the Very Large Array in Soccoro, New Mexico; section 2.1.2 for the Giant Meterwave Radio Telescope in Pune, India; section 2.1.3 for the Low Frequency Array whose core is near Exloo, the Netherlands.

2.1.1 The Very Large Array (VLA)

The VLA is a radio interferometer located in the plains of San Agustin in New Mexico, northwest of Socorro. This location is suited for radio observations since there are no major cities in the neighbourhood. Additionally, the plains

Configuration	B_{max} (km)	B_{min} (km)	θ_{HPBW}	θ_{LAS}
A	36.4	0.68	1.3 arcsec	36 arcsec
B	11.4	0.21	4.3 arcsec	120 arcsec
C	3.40	0.035	14 arcsec	970 arcsec
D	1.04	0.035	46 arcsec	970 arcsec

TABLE 2.2: Properties of the VLA at 1.4 GHz (21cm)

are surrounded by cliffs of rock that block off any remnant radio interference created by man-made devices situated in the neighbouring cities.

The interferometer consists of twenty seven 25 meter usable antennas placed in a Y-shaped pattern that can be used in 4 different configurations (A, B, C, and D) in which the spacing between the antennas is varied. The left panel of table 2.1 shows a closer look at some of the telescope dishes set up in the D-configuration. In addition to the different configurations, the telescope can be used with up to 10 bands that range in frequency from 74 MHz to 45 GHz (Napier et al., 1983).

The right panel of table 2.1 shows the 10 VLA receivers. The varying spacing between antennas makes it possible to have a maximum resolution of 0.04 arcseconds for the highest frequency band. For the purpose of this thesis, we shall only describe the telescope's properties in the L-Band which covers the frequency range from 1 GHz to 2 GHz. Table 2.2 shows the properties of the telescope at 1.4 GHz in detail.

For each year, the array is set up in two configurations, one after the other; therefore observing the same field using all configurations will take up to 2 years. From late 2013, an upgrade to the receivers makes it possible to observe with a wider frequency bandwidth. The scientific results in this thesis are obtained from data obtained after the upgrade. Archival data from the older narrower bandwidth data are also used to complement our results. Both observations were done using the L-Band receiver whose central frequency is 1.5 GHz. In order to confirm the properties of a source that is discovered with an observation at a particular frequency, follow up observations at other frequencies are usually carried out. We proposed to observe the same field at a lower frequency, 610 MHz, using another interferometer located in Pune, India; its description follows in section 2.1.2.

Figure 2.1: The GMRT radio telescope array consisting of thirty 45 m diameter antennas. Image Credit: The GMRT web page

2.1.2 The Giant Meterwave Radio Telescope (GMRT)

The GMRT is an interferometer consisting of 30 antennas spread out in a Y-shaped pattern with the longest baseline of 25 km. The diameter of each antenna is 45 m. In order to improve the telescope sensitivity to extended diffuse emission, 14 of the antennas are placed randomly in the core of the array within an area of 1 km squared (Swarup, 1990).

The telescope is located at a distance of about 10 km east of the Narayangaon town, along the Pune-Nasik highway. The design of the antennas is based on a concept called **S**tretch **M**esh **A**ttached to **R**ope **T**russes (SMART), making it light in weight and thus the low-cost 45 m diameter dishes.
The larger diameter of the antennas gives them an added advantage of having a collecting area three times more the than that of the VLA at the same frequency.

Band	ν (MHz)
1	50
2	153
3	233
4	325
5	610
6	1420

Table 2.3: Bands

The 6 frequency bands operated by the telescope array are listed in table 2.3. This gives the array a range in angular resolution from 60 seconds of arc for the lowest frequency to 2 seconds of arc for the highest frequency. For each band, dual polarisation outputs are offered. For studies where polarisation is not required, dual band observations are possible. For the study of Abell 115 at lower frequencies, we opted for a dual band observation in which we obtained data from both the 610 and 233 MHz recievers. Details of the data properties and quality will be discussed in the data reduction section. With data at three frequencies, reliable spectral analyses can be performed. It was later noticed that the GMRT data at 233 MHz was not of a quality that could enable a scientific analysis. This prompted us to request for an observation of the field using an interferometer that operates at much lower frequencies than most interferometers in the world, the LOw Frequency ARray telescope. A description of this spectacular array is provided in section 2.1.3.

2.1.3 The LOw Frequency ARray (LOFAR)

The LOFAR telescope is an interferometer whose core is located near Exloo in the Netherlands with the other stations being located within a radius of up to 80 km for those in the Netherlands, and for international stations as far as France, Germany, Ireland, Latvia, Poland, Sweden and the UK (Röttgering, 2003; van Haarlem et al., 2013). Another station is planned to be located in Mediccina, Italy (see e.g., ASTRON news)[2].

A total of 76 stations that are categorised as core, remote, and international operate in unison making it currently the largest radio telescope in the world (see fig. 2.2 (e) for an overview of all the station locations). Stations categorised as international are located outside of the Netherlands.

For each station, the electromagnetic signals are received by multiple dipoles (see fig. 2.2 (a)). The signals from all the dipoles under use are combined by beam forming to reduce the data rate and processing required. The observing frequency of the LOFAR telescope is between 15 MHz and 240 MHz, excluding the 87-108 MHz FM radio band. The frequency range necessitated a wide sensitivity range which is challenging for a single antenna type. Two types of antennas are therefore used: the Low-Band Antennas (LBAs) optimised for 30-80 MHz, and the High-Band Antennas (HBAs), optimised for 120-240 MHz. Within a station, the LBAs are placed in a pseudo-random way, with exponentially increasing distances (V. Cappellen et al., 2006).

The diameter of an LBA field is approximately 81 meters with each LBA consisting of one dipole per polarisation. The HBA *tiles* are placed as a dense and regular array with a size of about 41 meters in diameter for the remote stations. In the core stations, the HBA field is split into two arrays with a diameter of 31 meters each (see fig. 2.2 (b) for a remote station HBA field).

Each HBA is a compound element (which we call a *tile*) where 16 dual polarised antenna elements are combined using analogue beam forming per polarisation. The size of each HBA *tile* (4x4 dual-polarised dipoles) makes the effective area

---

[2] `http://www.astron.nl/lofar-crosses-alps-italy-joins`

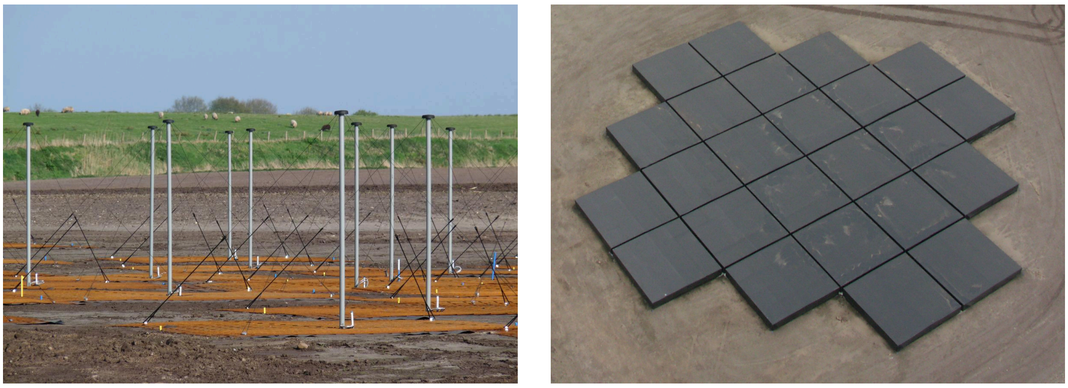

(a) Lateral view of a few of the LBA dipoles (b) Core station HBA field with 24 *tiles*

(c) LOFAR core, also called the *Superterp* (d) Core station setup with both HBA & LBA fields

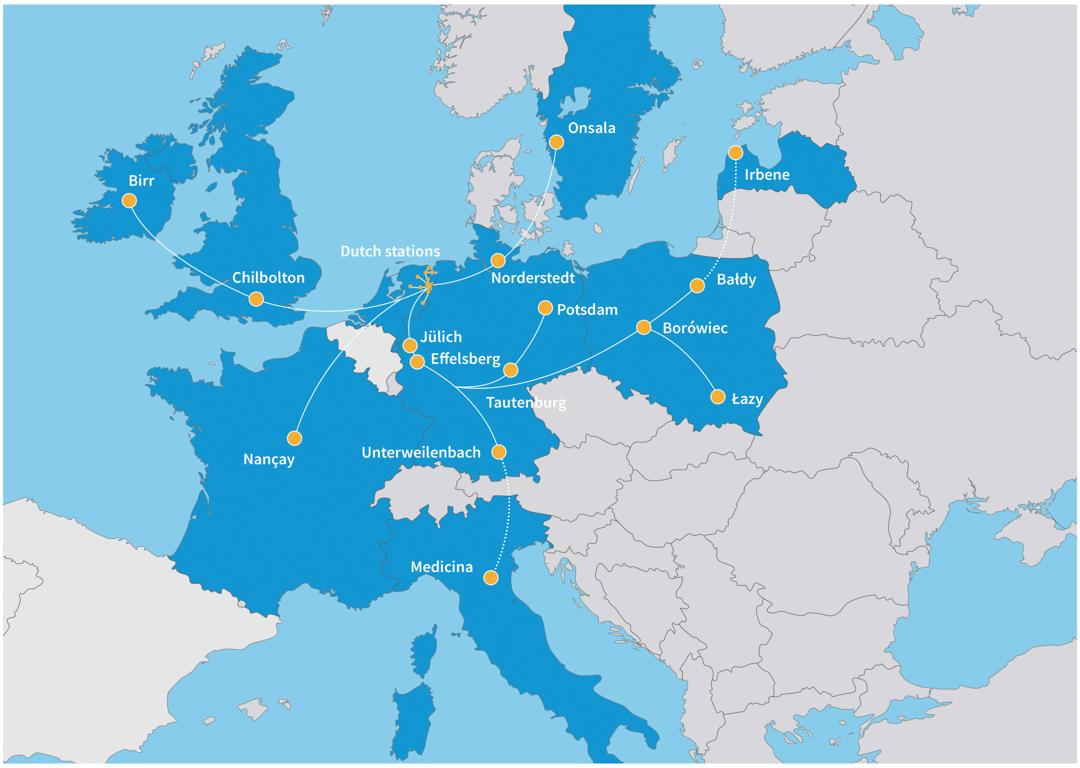

(e) Overview of all stations of the LOFAR telescope, dotted connections showing those under construction

Figure 2.2: An overview of the LOFAR antenna types, station setups, and array extension over the European continent. All Images' credit: ASTRON.

of the LBA and HBA roughly equal. After pre-filtering, amplification and, for the HBA, beamforming, the signals from LBA and HBA are transported over coaxial cables to station cabinets that process and send the data to a centralised high computing facility in the Netherlands for correlation with other stations.

A LOFAR station consists of both the LBA field and HBA field, with the difference being the number of dipole antennas for the core, remote and international stations. International stations have up to 96 dipole antennas for each field while remote and core stations have 48 and 24 dipole antennas per field, respectively. We use only the core and remote stations since the maximum baseline they provide is sufficient to produce a resolution comparable to that obtained with the GMRT and VLA arrays.

At the frequencies in which the LOFAR array operates, it is currently the most sensitive interferometer in the world. It is being used as a precursor for the forthcoming Square Kilometer Array (SKA) that is under construction in Australia and South Africa. With the number of dipole antennas involved for all stations, data transfer, storage, and computation stretch the limits of the current computer technology. Each station needs to transfer data with speeds of up to 10 Gb per second to the correlator located in Groningen, Netherlands. The correlator then needs to process the data at speeds of up to tens of TeraFLOPS. For a standard 8 hour observation, data of up to 20 TB is stored, making data handling challenging for the standard computing facilities. To overcome this, super-computing facilities across Europe are used both for storage and pre-processing before we can download pre-processed data of less than 5 TB.

Excluding international stations[3], the core and remote stations are placed in a manner that 120 km is the longest baseline. At a central frequency of 150 MHz for the HBA, this baseline provides a resolution of up to 3.6 seconds of arc. With such a resolution, we are able to match similar structural details in all the images obtained at other frequencies. Although the LOFAR telescope has a lower band, the LBA, we have not yet obtained data using these antennas. An observation at these ultra low frequencies is planned.

The three telescopes described before operate with different receivers designed for different frequency bands. The data obtained from these telescopes is therefore treated differently, sometimes with different software packages, in order to cater for the different formats and handling requirements of each data

---

[3] For our research purpose, we do not need such long baselines.

set. A general description of how interferometric data is treated will be described in section 2.2, where the specific tasks for the different packages of software used are described.

2.2 VLA & GMRT Data Reduction

Data reduction for radio astronomy involves obtaining an accurate representation of the sky brightness distribution from the induced voltages measured by the antennas' receivers. For an interferometer, it includes summing up all these voltages from each dipole antenna so that the result is a representation of what a single dish telescope with a diameter equivalent to the separation of the individual antennas reproduces. In order to obtain an accurate representation of the sky brightness, obstructions to the wave propagation from the sky have to be mitigated. In addition, interferences caused by the receiver unit electronics have to be suppressed. An equation that describes the handling of all these contributions, for all polarisations, is called the Radio Interferometry Measurement Equation (RIME: Hamaker et al., 1996) as described in section 2.2.1.

2.2.1 The Radio Interferometer Measurement Equation

This formulation assumes that the radiation propagates from a single point. This means that if we take z to be the direction of propagation, we can define the propagation of the electric field of the source as

$$\mathbf{e} = \begin{pmatrix} e_x \\ e_y \end{pmatrix}. \tag{2.4}$$

Assuming that the propagation of the wave is linear enables us to describe the propagation using a 2×2 matrix. This means that the voltages induced by the electric field and measured by each antenna, or station, will also be linear with respect to e. Thus for each antenna, the voltages are described by

$$\mathbf{v}_i = \mathbf{J}_i \mathbf{e}. \tag{2.5}$$

For a single baseline with antenna 1 and 2:

$$\mathbf{v}_1 = \mathbf{J}_1\mathbf{e}, \tag{2.6}$$

$$\mathbf{v}_2 = \mathbf{J}_2\mathbf{e}, \tag{2.7}$$

where **J** is a term that is solved for during calibration. This is the term that describes the electronic response of the signal plus additional atmospheric effects encountered along its path. The interferometer measures cross correlations between the two voltages, i.e

$$v_{xx} = \langle v_{1x}v^*_{2x}\rangle \tag{2.8}$$

$$v_{xy} = \langle v_{1x}v^*_{2y}\rangle \tag{2.9}$$

$$v_{yx} = \langle v_{1y}v^*_{2x}\rangle \tag{2.10}$$

$$v_{yy} = \langle v_{1y}v^*_{2y}\rangle. \tag{2.11}$$

The combined measured voltage, which is called the visibility, can thus be written in matrix form as

$$\mathbf{V}_{12} = \begin{pmatrix} v_{xx}v_{xy} \\ v_{yx}v_{yy} \end{pmatrix}. \tag{2.12}$$

In terms of the electronic response of the signal, we can represent the visibility of the two antennas as

$$\mathbf{V}_{12} = \langle(\mathbf{J}_1\mathbf{e})(\mathbf{J}_2\mathbf{e})^T\rangle = \mathbf{J}_1\langle\mathbf{e}\mathbf{e}^T\rangle\mathbf{J}_2^T, \tag{2.13}$$

where the convolved term $\langle\mathbf{e}\mathbf{e}^T\rangle$ represents the brightness of the source and can be simply written as **B**. The final representation of the visibility of the two antennas can therefore be written as

$$\mathbf{V}_{12} = \mathbf{J}_1\mathbf{B}\mathbf{J}_2^T. \tag{2.14}$$

Equation 2.14 is known as the radio interferometer measurement equation (Hamaker et al., 1996; Sault et al., 1996; Hamaker, 2000; Hamaker, 2006). Each of the terms are matrices where the **J**s are called Jones matrices. The Jones matrices are a product of all the terms that describe the full signal path. These terms are multiplied in a specific order, which is the actual order of effects that the signal has to deal with as it propagates from the source (Sault et al., 1996). These terms are called Jones terms since each of them can be represented by a simple Jones matrix. Appendix B shows all the generic Jones terms with a description of each term.

The measurement equation reproduces the correlated antenna gains for each baseline ($\vec{b} = \vec{b_x} + \vec{b_y}$) shown as a complex number whose real & imaginary parts are the amplitude & phase at a given position in (u, v) space where $u = \frac{\vec{b_x}}{\lambda}$ and $v = \frac{\vec{b_y}}{\lambda}$. The (u, v) is a plane that is traced by the baselines as the earth rotates. The resulting voltage pattern will thus be represented by $\mathbf{V}(u, v)$. In order to obtain the sky brightness, $\mathbf{I}_\nu(l, m)$, where $l = \sin\theta_x$ and $m = \sin\theta_y$, we need to perform a Fourier Transform. This enables us to obtain an image that portrays the sky brightness distribution. The formulation is written as

$$\mathbf{V}_\nu(u, v) = \int \mathbf{I}_\nu(l, m) e^{2\pi i(ul+vm)} \mathbf{d}l\mathbf{d}m. \tag{2.15}$$

Equation 2.15 is unique for each baseline length and orientation. In order to sample the entire (u, v) plane in the most uniform way, we need to sum up all the possible baselines available for the different orientations achieved. To achieve this, a process that utilises the earth's rotation, called aperture synthesis is used. Data retrieved from the telescope will thus have a sampled (u, v) plane. The steps that are followed after the data has been retrieved from the observatory are described in sections 2.2.2 to 2.2.4.

2.2.2 Flagging

The data retrieved from the radio observatory is not free of unwanted signals. This is because the receivers will be sensitive to any radiation that propagates within that frequency band; this could be signals from the infrastructure of mobile communication, wind turbines, emergency service communication systems, etc. The data, or a part of it, can also be corrupted during the observation process due to faulty receivers, faulty connections with the correlator, non-operational antennas, etc. The process of getting rid of this unwanted signal in the data is what we refer to as flagging. Generally, all data from radio telescopes (including arrays) will require some flagging. It has become good practice for easily indentifiable unwanted signals to be removed even before a standard calibration has begun. Since observatories take records of all failures during the observation, most observatories will either provide a record of all known faults during the observation or remove the unwanted signal from the data before providing one with their requested data. The data obtained will still require additional scrutiny in order to excise the sections affected by Radio Frequency Interference (RFI) that were not identified by the observatory data pre-processing software. We flagged out unwanted signals using the `AOFlagger`, a software designed specifically to handle RFI identification and excision (Offringa, 2010; Offringa et al., 2012).

2.2.3 Phase and Flux Calibration

Since observed visibilities are always different from the true visibilities, we need to estimate the effects that could have caused this difference and perform a correction to the observed visibilities in order for them to match the true visibilities. This difference is caused by the inhomogeneity of the sky and the earth's surface making each receiver of the array subject to have a different ray path length to the source. This is corrected for by calculating the additional time delays needed for each receiver in order for the signal from a single source to arrive at the receiver (or correlator) at the same time. In addition, since the earth will rotate during the observation, experiencing a different atmosphere with time, the correction has to also be made periodically at well chosen time intervals. This is the calibration of the phases and fluxes. The delay correction and the flux density correction are performed by observing calibrators[4] through out the observing run. A flux calibrator is usually observed at the beginning and at the end of the observation while a phase calibrator will be observed at well chosen time intervals during the observation. Calibrators are observed simultaneously with the field as their already known flux densities do not vary strongly with time. The calibrators are isolated, small-diameter radio sources (mostly core-dominated, radio-loud quasars (CDRLQs)) making it sensible to be treated as constant flux point sources whose positions are known with high precision. The differences between the amplitude and phase of the observed data and the known data can be used to calculate an initial correction to the phase and amplitude of the source. The phase calibrator is used to correct the amplitude and phase over time, compensating for the changing atmospheric effects (refraction,

---

[4] These are bright sources in the sky whose properties are well known and are used to estimate the properties of the sources in the field whose properties we do not know yet.

absorption and rotation of the plane of polarisation) and the change in the path length and therefore time delays of the incident radio waves due to the elevation of the source. The flux calibrator is then used to correct for differences between the real flux density of the source and the observed flux density. The final corrections made are then applied to the data.

Labelling true visibilities as $\overline{\mathbf{V}}_{ij}(t)$ and the observed visibilities as $\mathbf{V}_{ij}(t)$, the calibration process follows the relation;

$$\overline{\mathbf{V}}_{ij}(t) = \overline{\mathbf{G}}_{ij}(t)\mathbf{V}_{ij}(t) + \epsilon_{ij}(t) + \eta_{ij}(t). \tag{2.16}$$

where $\overline{\mathbf{G}}_{ij}(t)$ is the baseline based complex gain, $\epsilon_{ij}(t)$ is a baseline based offset, and $\eta_{ij}(t)$ is the stochastic complex noise at the time of observation represented by t (Sault et al., 1996).

2.2.4 Imaging and Self-Calibration

Once the data has been calibrated well, an image of the field is created by applying a Fourier transform to the *uv* data. The image is improved using procedures (e.g., `CLEAN`: Högbom, 1974) which deconvolve the brightest point in the initial map with a point source, then deconvolve the next brightest, and so on, for a given number of iterations. When the final image achieved is not deep enough, a procedure known as *self-calibration* is performed (Hamaker, 2000; Hamaker, 2006). In this procedure, the final cleaned image (instead of the calibrators) is used to calibrate the *uv* data so that more corrections are made, thus termed *self-calibration.* When subsequent phase *self-calibrations* are combined and applied, the real structure, though very faint, is revealed. With no further improvement, an amplitude *self-calibration* is performed to correct the flux density. All final total intensity maps from interferometric data in this study were *self-calibrated.*

2.3 LOFAR Data Reduction

Unlike the GMRT and VLA, LOFAR is a “software” telescope with no moving parts (Bell et al., 2000). The direction of the sky to be observed is selected by means of computing individual delays for each station dipole so that the station beam is sensitive (for the most part) to that part of the sky. Due to such a novel technique, high time resolutions are required making the data volumes huge. This led to the development of techniques on how to handle data which have never been used before. These techniques follow the general RIME equation, albeit with special ways on how to handle huge volumes of data (e.g., splitting the data in chunks, performing the calibration for each chunk individually, and then combining the solutions before applying to target data). A brief overview of these techniques is discussed in sections 2.3.1 and 2.3.2.

2.3.1 Phase and Flux Calibration: `pre-FACTOR`

This consists of parsets (information scripts) that are run through a `generic pipeline` to do the initial phase and flux calibration. It is named `pre-FACTOR` since it sets up the data for a more rigorous calibration and imaging performed by another set of parsets called `FACTOR`. The main issues corrected for here are: (1) clock-TEC separation and then transferring the solutions obtained from the target to the calibrator, (2) flagging and averaging of amplitude solutions, (3) plotting diagnostic plots which are used for further investigation, and (4) performing a direction independent imaging of the field which in turn creates an initial sky model of the field to be used when performing direction dependent imaging.

2.3.2 Imaging and Self-Calibration: `FACTOR`

This is a set of parsets developed to perform direction dependent high-resolution imaging for LOFAR-HBA data. The scheme is described in detail by van Weeren et al. (2016) and Williams et al. (2016). The overall idea is to divide the pointing on the sky into facets using the Voronoi tessellation scheme (e.g., Senechal, 1993; Okabe, 2000), where by each facet contains a radio source that is bright enough to act as a calibrator for that region. The area covered by facets is limited by the maximum image size allowed by the user for a given facet. This is done to prevent having very large facets, which in time will require a huge amount of memory during the imaging step. A facet-by-facet imaging and self-calibration is then performed with the initial sky-model from the direction independent images acting as the initial sky model. When all facets have been imaged, a mosaic of all facet images is made

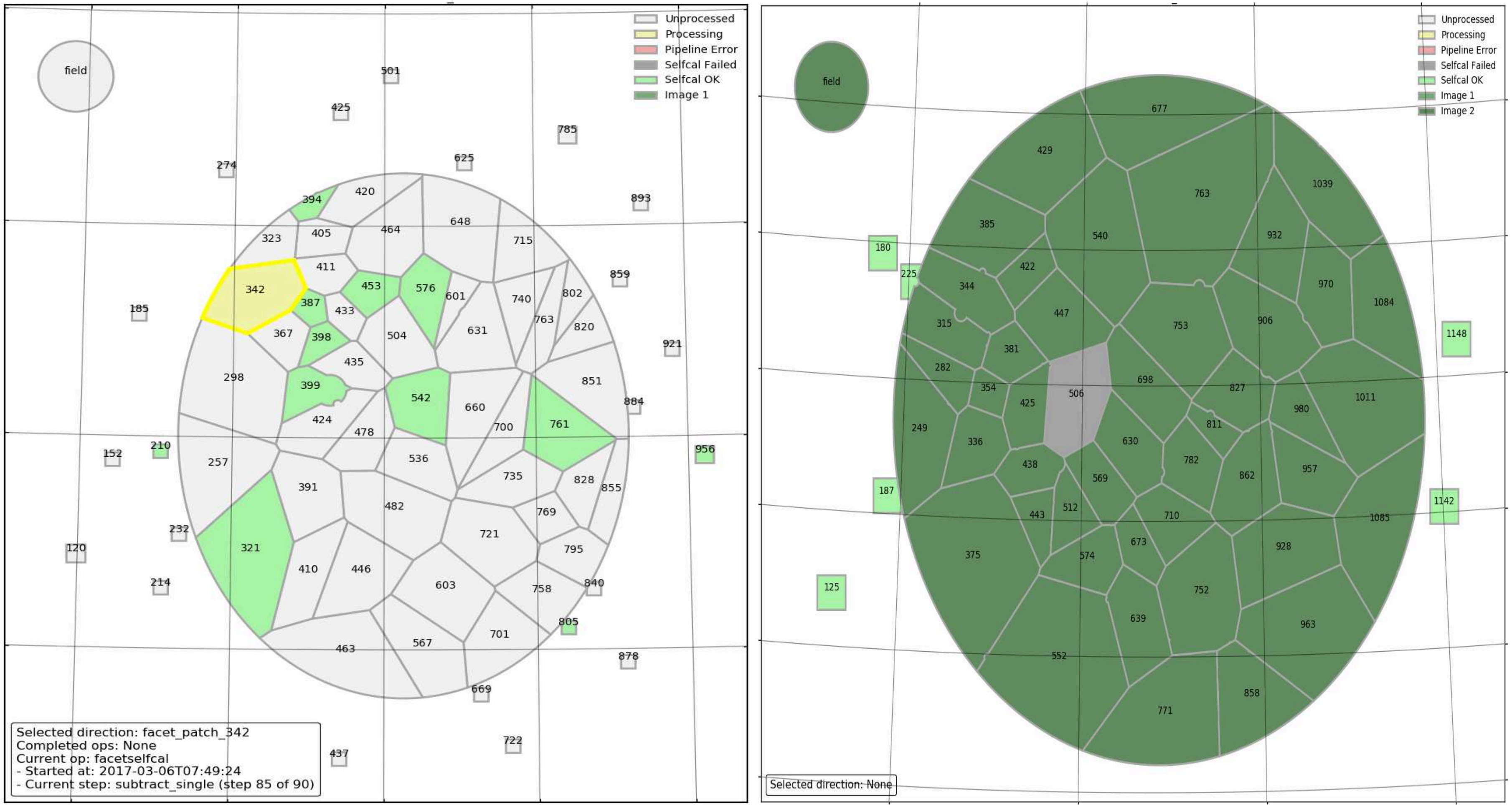

```
Selected direction: facet_patch_342
Completed ops: None
Current op: facetselfcal
- Started at: 2017-03-06T07:49:24
- Current step: subtract_single (step 85 of 90)
```

```
Selected direction: None
```

Figure 2.3: Facets generated by `FACTOR` for the A115 (left) and A1430 (right) fields. The A115 galaxy cluster lies in facet 399 while A1430 lies in the facet 509.

to obtain a low-noise high-resolution map of the whole field. The facet that includes a particular source of interest can then be investigated thoroughly, sometimes with other radio astronomy data processing tools like `CASA`. Figure 2.3 shows the facets generated for A115 (left) and A1430 (right), the green colour showing those facets with which self-calibration and imaging has already been performed. The imaging and self-calibration procedure may vary depending on either the data quality or the dynamic range needed for a field. Fields with very bright (a few Jy) sources require a high dynamic range imaging strategy in order to achieve low noise images. We describe the imaging and self-calibration procedures used for the two fields, A115 (in **chapter 3** section 3.2.4) and A1430 (in **chapter 4** section 4.2).

2.4 Single-Dish Telescopes

A single dish telescope is one consisting of a parabolic reflector which focuses the incoming radio signal onto a receiver/detector. It should be noted here that there can be different setups of the signal path; in some cases having multiple reflectors and/or different ways the receivers are mounted.

Single dish telescopes range in sizes from those that are small enough to be launched in space to some with a diameter of a few tens of meters. In section 2.4.1 we describe the 100 m fully steerable radio telescope in Effelsberg, Germany (see fig. B.1) with which we carried out observations on six galaxy clusters.

2.4.1 The *Effelsberg* Single Dish Radio Telescope

As early as the late 1960s, Hachenberg et al. (1973) were able to highlight how important such a telescope would be for studies of extragalactic radio sources. The success of which is reported by Murdin (2000) and Wielebinski et al. (2011). Although interferometers are very useful in radio astronomy for higher resolution studies, we describe instances where a single-dish telescope would be crucial. These include among others:

Sensitivity: A single-dish telescopes will provide a large collecting area as opposed to antennas of interferometers. The interferometer having dishes with the largest diameter is the GMRT, with a dish diameter of 45 m. The larger the diameter of the dish, the more radio energy it can collect and focus to the receiver. This means that for very faint sources, telescopes with very large diameter dishes will be able to detect their emission. It should be noted that the sensitivity of a telescope is also dependent on other factors such as the system noise in the electronics of the receiver (Burke and Graham-Smith, 1997).

Instrumentation: For specialised detectors, it will be much cheaper to construct one unit that is mountable on single-dish telescopes as opposed to interferometers where one has to mount the detectors on all array antennas.

Availability: For astronomers, there are more single-dish telescopes available for observations than interferometers (arrays). This is clearly seen especially for those in the southern hemisphere where the only interferometer that can be used is the Australian Telescope Compact Array (ATCA). This is in part, due to the costs involved in constructing arrays and also due to the multi-use single dish telescopes can be, especially for use in satellite navigation & telecommunication. In many other countries, single-dish telescopes that were previously used for satellite navigation & telecommunication have been converted to be used for research adding to the number of available single-dish telescopes to astronomers.

Ease of use: The data we obtain from single-dish telescopes does not need correlation keeping the computational resources needed at a minimum.

2.4.2 *Effelsberg* 100 m Telescope Data Reduction

Unlike interferometers where the data from an individual antenna needs to be correlated with others to form the array beam, a single-dish telescope will simply transform the data stream (time series) into a two-dimensional map. For each radio telescope, a system specific to the telescope is used to generate the raw data. For the 100 m Effelsberg radio telescope, the data are preprocessed with a package called "`Toolbox`" (see Müller et al., 2017, Appendix A). The basic steps followed to reduce data from a single-dish are: (1) Removing radio-frequency interference (RFI) in the raw continuum data stream from the output channels of the polarimeter, (2) Calibration of all Stokes parameters ($\mathcal{I}$, $\mathcal{Q}$, $\mathcal{U}$) by applying the *Mueller Matrix*, (3) Interpolation of the raw data with a *sinc* weighting function into square pixels and combining them into maps, and (4) Generating additional maps for the sidereal time and the parallactic angle for each pixel in the map to allow for the transformation of maps from the horizontal

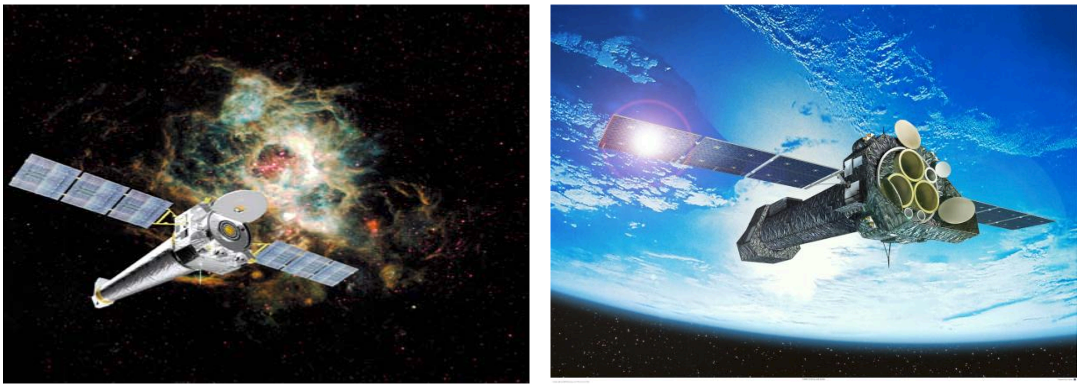

(a) The *Chandra* X-ray Observatory (b) ESA's *XMM-Newton* X-ray Telescope

FIGURE 2.4: Artistic illustration of the *Chandra* spacecraft in orbit (left), Credit: *Chandra* X-ray Obs.; *XMM-Newton* (right), Credit: ESA/XMM-Newton

coordinate system to the equatorial coordinate system. This is done only for maps scanned in the azimuth direction.

The data generated by "`Toolbox`" is then reduced preferably with the `NOD3` package described by Müller et al. (2017). The analysis of the final maps can be done with any other software of choice after the maps have been rotated and transformed to a coordinate system of one's choice.

2.5 X-ray Telescopes

An X-ray telescope is one that observes the very faint astronomical sources in the X-ray spectrum. They are launched to the outside of the earth's atmosphere because the earth's atmosphere absorbs all the X-ray radiation from astronomical sources (e.g., for the purpose of our study, the ICM in galaxy clusters). In this work, we use data recorded by two X-ray telescopes; the *Chandra* X-ray telescope (Garmire, 1999; Rajiva, 1999; Weisskopf, 1999) and the *XMM-Newton* X-ray telescope (Barré et al., 1999; de Chambure et al., 1999). The data was crucial in the analysis of correlations between the radio synchrotron emission and the thermal X-ray gas.

2.5.1 *Chandra* X-ray Observatory

The *Chandra* X-ray Observatory (see fig. 2.4 (a)) is a telescope operated by NASA[5] specially designed to detect X-ray emission from very hot regions of the Universe such as exploded stars, clusters of galaxies, and matter around black holes. It was launched on July 23, 1999 to an altitude of 139,000 km in space. The Smithsonian's Astrophysical Observatory (SAO) in Cambridge, MA, hosts the *Chandra* X-ray Centre which operates the satellite, processes the data, and distributes it to scientists around the world for analysis.

2.5.2 *XMM-Newton* X-ray Telescope

XMM-Newton (see fig. 2.4 (b)) is a European Space Agency's (ESA) X-ray Multi-Mirror Mission (*XMM-Newton*) that was launched by an Ariane 504 on December 10th 1999. *XMM-Newton* is ESA's second cornerstone of the Horizon 2000 Science Programme. It carries 3 high throughout X-ray telescopes with an unprecedented effective area, and an optical monitor, the first flown on a X-ray observatory (Jansen et al., 2001). The large collecting area and ability to make long uninterrupted exposures provide highly sensitive observations. The *XMM-Newton* telescopes have been built by Carl Zeiss (Oberkochen, Germany), Kayser-Threde (Munich, Germany) and Media Lario (Bosisio Parini, Italy). X-ray tests were performed in the PANTER test facility of the Max-Plank-Institut für extraterrestrische Physik.

2.6 X-ray Data Reduction

X-ray data is recorded in events' files. An *events* file contains information about the position, energy and time of each photon detected by the instrument (Lumb and Holland, 1988). Position information is useful for image construction while energy information is used to extract spectra. The initial data, called *raw* data; are pre-processed using a pipeline that is instrument specific. This means that *raw* data files from two different X-ray telescopes are treated differently. We will describe briefly the pipelines for both telescopes in sections 2.6.1 and 2.6.2.

---

[5] The National Aeronautics and Space Administration, an independent agency of the executive branch of the United States federal government responsible for the civilian space programme, as well as aeronautics and aerospace research.

2.6.1 Calibrating *Chandra* Data

The *Chandra* data we used in this work was obtained using the AXAF CCD Imaging Spectrometer (ACIS) instrument (Garmire et al., 1986; Bautz et al., 1996; Bautz et al., 1998). The Standard Data Processing (SDP) of this data follows several levels, the first of which are automatically performed by the *Chandra* X-ray Centre (Plummer and Subramanian, 2001). Level 0 converts the raw telemetry into FITS files and at level 1, an instrument correction is applied to produce the events files. Level 2 filters the events file to good time intervals (GTIs) and produces a candidate list. The data analysis software we used is `CIAO version 4.10` (Fruscione et al., 2006). Using the events file produced at level 1, we cleaned the data of spurious events (e.g., cosmic rays). Using the tool `acis_run_hotpix`, we identify and store the information about the hot pixels, afterglow events[6], and pixels with bright bias in a file that is applied to the events file using the `acis_process_events` tool. The final step in this basic pipeline is to flag and remove streaks where a significant amount of charge is randomly deposited along pixel rows as they are read out. These data is automatically flagged for ACIS observations at level 1 and can then be removed at level 2. We finally obtain a FITS file which we use for the analyses.

2.6.2 Calibrating *XMM-Newton* Data

XMM-Newton data on the other hand consists of three events files, one for the PN camera and one for each of the MOS cameras. The *XMM-Newton* data reduction in this work was done using `SAS version 16.1.0` (Gabriel et al., 2006; Gabriel, 2017). A standard pipeline is developed to perform an initial data reduction on the *raw* data files. The pipeline calibrates, removes hot pixels and excludes out-of-field events from the events list. To make an image of the data, the datasets were energy-filtered to include energies between 0.3 and 5.0 keV, unless stated otherwise, before using `evselect` to generate images. We then combined the exposure maps for each camera and divided the combined image by the total livetime. The combined scaled image was then divided by the combined scaled exposure map thus removing the chip gaps from the final image. The FITS image obtained was then used in the analyses.

---

[6] These are events where a cosmic ray has interacted with the CCD leaving a residual charge.

Chapter 3

The Complex Radio Relic in Abell 115

In this chapter, we study the merging galaxy cluster Abell 115 since there was tentative evidence that it hosts a large scale diffuse synchrotron source that could be a radio relic (Govoni et al., 2001). In our study, we analysed archival data from the VLA and new data from the GMRT and LOFAR. In addition, new data from the upgraded VLA, with a wide band L-band receiver was used. A wide band spectral index and polarisation analysis were made, and the merger scenario investigated. From the analyses, we could claim that: (1) The extended diffuse radio emission in A115 is indeed a radio relic and show that the morphology remains the same even when observed at lower frequencies. (2) Merging galaxy clusters generate large scale shock waves that permeate the ICM; the leading edges of the shock waves provide a conducive environment for electron acceleration, giving rise to extended diffuse radio sources called radio relics. (3) The cluster Abell 115 is a prime cosmic laboratory for studying magnetic fields in low density cluster environments since part of the relic lies in a region with less dense ICM. (4) Observations of galaxy clusters with LOFAR improve our understanding of the electron acceleration processes in galaxy clusters since the low frequencies probe less massive systems whose radio synchrotron power is below the detectability threshold at higher frequencies. (5) A high dynamic range is necessary in order to calibrate properly the regions that host low surface brightness sources like radio relics. A very bright source close to a low surface brightness source will otherwise prevent a deeper “cleaning”.

We therefore present, pedagogically, the details of our study in the sections that follow.

3.1 Introduction

Abell 115, hereafter A115, was first observed in the X-ray with the *Einstein* Observatory, finding that it has a bimodal distribution of the X-ray surface brightness (Beers et al., 1983). Figure 3.1 shows the bimodal X-ray surface brightness distribution of A115 (Hallman et al., 2018). The X-ray luminosities measured for the two A115 sub-cluster components were $32 \pm 3 \,\&\, 19 \pm 2 \times 10^{43} \mathrm{ergs\,s^{-1}}$(Forman et al., 1981). An optical follow up was made by Geller and Beers (1983), who found three clumps of galaxies; of which two were associated with the two extended X-ray surface brightness clumps. The association of the galaxy number density[1] clumps with the X-ray surface brightness clumps shows that A115 can be a multi-component system. Beers et al. (1983) studied the velocity dispersion of galaxies in A115, concluding that this is a disturbed system. This shows that galaxy clusters with multiple components are prime targets for the study of the dynamics in galaxy clusters.

The advancement of CCD detectors in the late 1980's made it possible to carry out an optical follow up using deep CCD observations. The photometry of all field objects was examined in order to study the morphology of all galaxies in the field. The dominant morphological galaxy type in a galaxy cluster can be used to trace the activity in the cluster. A115 is composed of a similar number of early type (elliptical galaxies & barred spiral galaxies) and late-type galaxies (spirals galaxies), which also suggests that it is a dynamically active system (Gregorini and Bondi, 1989). Relaxed systems have a larger fraction of early-type to late-type galaxies.

Another indication of a dynamic system is the electron temperature variation ($\Delta \mathrm{T_e}$) of the ICM. An X-ray study of $\Delta \mathrm{T_e}$ with the Advanced Satellite for Cosmology and Astrophysics (ASCA) showed a significant variation, confirmed by the hardness ratio analysis and spectral fits. Moreover, a linking region between the main cluster and sub-cluster showed a higher temperature compared to other regions (Shibata et al., 1999). Two possibilities were examined as the cause of the temperature variation: (1) Cooling flows in the main cluster and (2) Shock heating due to the collision of the sub-cluster into the main system. The high temperature in the linking region implies that Abell 115 is undergoing a merger, with a possible contribution from cooling flows on the temperature structure (Shibata et al., 1999).

---

[1] The galaxy surface number density is a probe used to trace the dark matter halos.

Since A115 is a peculiar system and hosts a very bright radio galaxy (3C28), deeper X-ray observations and analyses are still ongoing to examine the details of the merger, including the velocities of the sub-clusters through the analysis of the cold front and a weak shock (Forman, 2017), how the energy of the merger is dissipated into thermal and non-thermal forms (Burns et al., 2017), and to constrain the merging scenario of this complex system by mapping the dark matter (Kim et al., 2018).

A merging system will have an imprint on the star formation history of the various galaxy types it hosts. The fraction of blue galaxies in A115 is found to be $f_B = 0.13$ and their radial distribution supports the prediction of galaxy harassment mechanisms for tidally induced star formation operating on an infalling set of gas-rich galaxies (Rakos et al., 2000).

We therefore study the merging galaxy cluster, the extended diffuse radio source in it plus other diffuse sources that could have arisen from the merger activity. Table 3.1 shows the properties of the cluster. The large scale extended radio relic was discovered using VLA observations of the galaxy cluster by Govoni et al. (2001). Relics are suggested to trace large scale merger shocks, where electrons are re-accelerated due to the multiple crossings they make along the shock surface (see e.g., Blandford and Eichler, 1987; Jones and Ellison, 1991). Shocks can also adiabatically compress and trigger the acceleration of electrons in relic plasma left behind by previously active galaxies (Enßlin and Gopal-Krishna, 2001; Enßlin and Brüggen, 2002). It should be noted that the relic lies in the a region where there are two bright radio galaxies. The radio galaxies could be sources of the high-energy electrons.

The merger in A115 is suggested to be off-axis. This is based on new spectroscopic and photometric analyses by Barrena et al. (2007), where the northern sub-component (A115N) and the southern sub-component (A115S) are colliding with a line-of-sight (LOS) impact velocity $\Delta v_{\rm rf} \sim 1600\,{\rm km\,s^{-1}}$. This means that the radio relic with its largest dimension perpendicular to the merging axis is likely connected to this merger. When A115 was later re-observed with *XMM-Newton*, the temperature maps obtained showed evidence of pre-merger activity (Beygu et al., 2009).

Mergers generate shocks that should be seen as sudden jumps in X-ray surface brightness and temperature profiles. Indeed, an X-ray shock is found for part of the relic emission (Botteon et al., 2016). Hallman et al. (2018) too suggest a dynamical scenario that is consistent with the structure of the X-ray gas, the hot region between the sub-cluster components, and the radio relic feature.

Merger shocks can also be studied using radio spectral studies, where the Mach number of the shock is related to the spectral index of the injected relativistic electrons. This is possible when the radio emission is studied at different frequencies in order to obtain a reliable spectral index of the relativistic plasma. We report additional radio observations from the WRST and GMRT; we show in section 3.3 that the large scale emission is indeed a relic, by constraining the spectral index further (Dumba et al., 2015).

We present here the first radio observation at low frequencies with the LOFAR-HBA centred at 143 MHz. The results are complemented with both GMRT observations at 610 MHz and archival VLA 1.4 GHz C & D configuration data. Results from a wide-band VLA B-configuration L-band observation are also shown.

Property	Quantity	Reference
Coordinates (J2000)	RA $00^{\mathrm{h}}55^{\mathrm{m}}59.0^{\mathrm{s}}$ DEC $26^{\circ}22'41''$	(Piffaretti et al., 2011)
z (redshift)	0.197	(Struble and Rood, 1999)
Physical scale	3.29 kpc/$''$	(Wright, 2006)
Abell Richness Class	3	(Abell, 1958)
Bautz-Morgan type	III	(Bautz and Morgan, 1970)
Virial Mass ($h_{70}^{-1}\mathrm{M}_{\odot}$)	$(2.2 - 3.5) \times 10^{15}$	(Barrena et al., 2007)
$L_{\mathrm{X}}(0.1 - 2.4$ keV)	1.57×10^{45} ergs s^{-1}	(Govoni et al., 2001)

TABLE 3.1: Basic properties of the galaxy cluster Abell 115.

3.2 Radio Observations & Data reduction

All radio observations were performed using arrays due to the moderate resolution required in order to identify discrete sources in the field. The A115 field is host to two bright radio galaxies that require a moderately high resolution to be studied. We present results from the analysis of data from previous observations performed by Govoni et al. (2001) and from observations that we performed in order to follow up on their study.

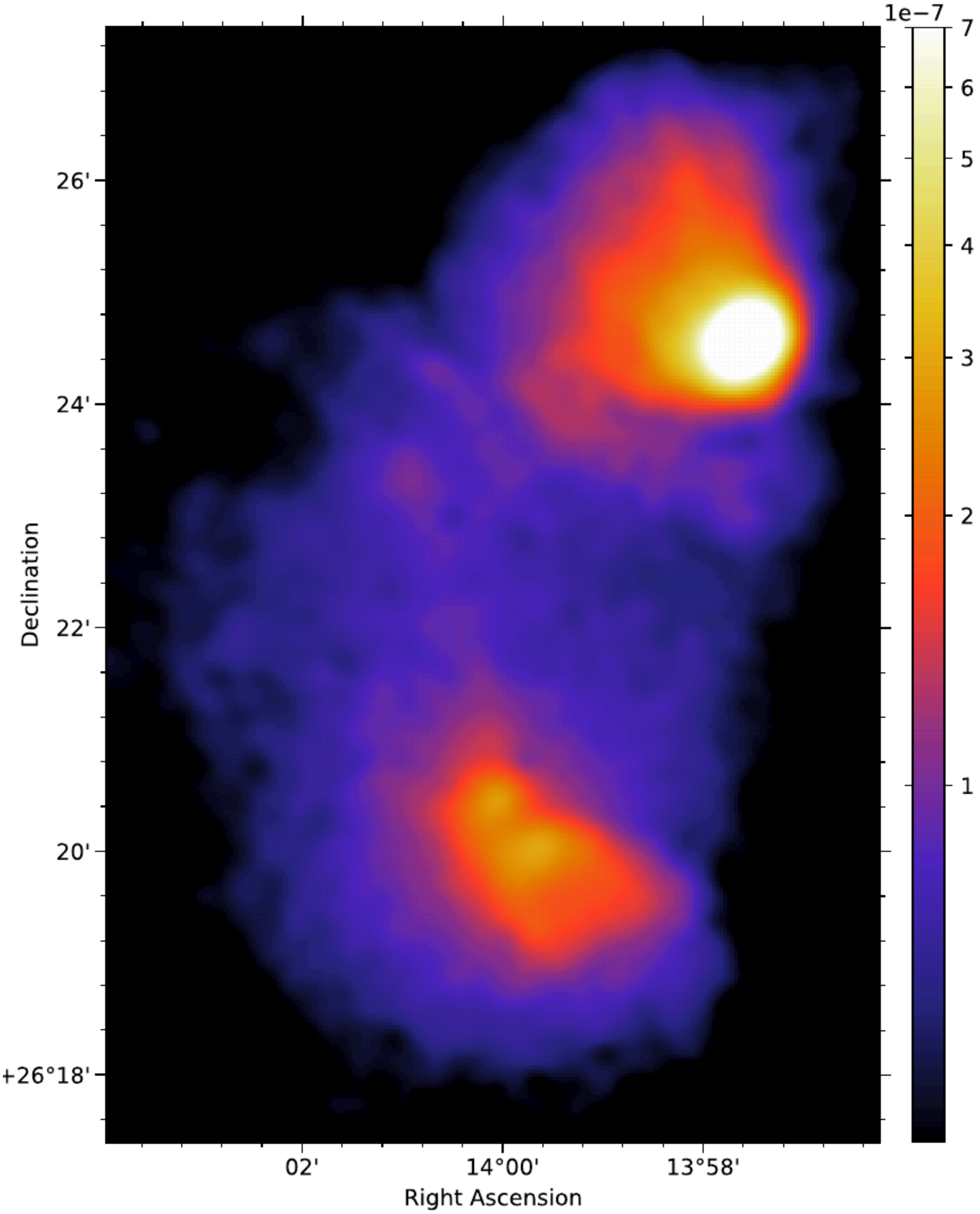

FIGURE 3.1: X-ray Bimodal distribution of Abell 115. The color scale shows the electron temperature in the range 0.5 – 8.0 keV. (Hallman et al., 2018)

	LOFAR	GMRT	VLA		
Frequency	143 MHz	610 MHz	1.5 GHz	1.4,1.4 GHz	1.4,1.7 GHz
Obs. date	Sept. 2016	Jul. 2011	Nov. 2017	Dec. 1998	Mar. 1999
Setup/mode	Interleaved	Dual	B-config.	C-config.	D-config.
Flux Cal.	3C295	3C48	3C286	3C48	3C48
Phase Cal.	3C196	3C468.1	J1219+4829	J0119+321	J0119+321
Bandwidth	44 MHz	32 MHz	800 MHz	50 MHz	50 MHz
Chan. width	200 kHz	125 kHz	1000 kHz		
Int. time	2 s	16.9 s	3 s	5 s	5 s
Obs. time	6 hrs	4 hrs	3 hrs	3 hrs	3 hrs
Max. Res.	3″.6	5″.5	3″.3	12″.5	25″.7
σ_{rms}	200 µJy	600 µJy	30 µJy	65 µJy	74 µJy
polarisation	XX,YY	RR	RR,LL	RR,LL	RR,LL

TABLE 3.2: Observations of the galaxy cluster A115 field using three different arrays.

3.2.1 Previous Observations

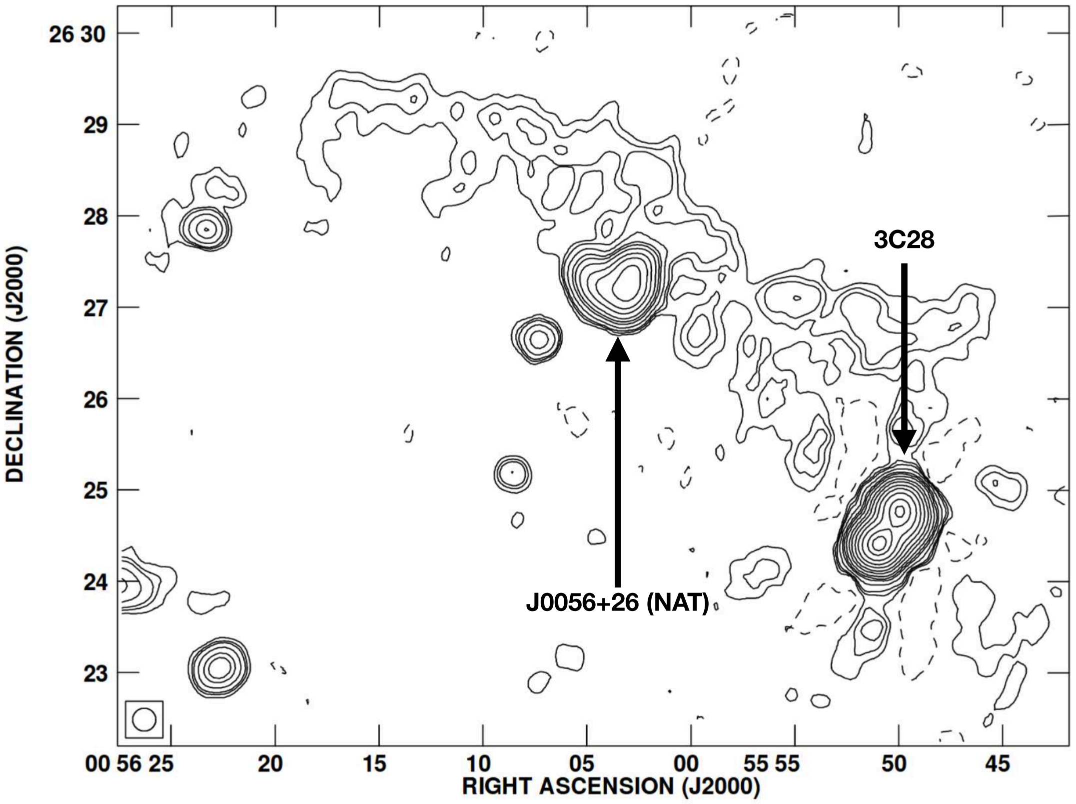

FIGURE 3.2: Abell 115 radio relic as shown in Govoni et al. (2001). Resolution is 15″ × 15″; the noise level is 0.1 mJy/beam. First 5 contour levels are: -0.4, 0.4, 0.7, 1, 2, 4 mJy/beam. The extended diffuse synchrotron source is clearly visible; the two radio galaxies that lie close to the radio relic are labelled.

A115 was observed in 1998/1999 with the VLA at 1.4 GHz in the C and D configurations for a total observing time of 2 hours for each configuration. The observing frequency and configurations were chosen in order to have a good sampling of short spacings with the hope that a halo-like source could be easily detected. However, no radio halo was found for A115. The details of these observations are given in table 3.2. The different frequencies were chosen in order to obtain an estimate of the spectral index of the diffuse source. The results from this observation are presented in Govoni et al. (2001). The radio relic was clearly visible (see fig. 3.2), elongated in the SW-NE direction, with a projected maximum extension of about $10'$, which is about 2 Mpc in size. The spectral index obtained was $\alpha \sim 1.1$. We obtain additional observations at other frequencies in order to confirm the nature of this diffuse source and constrain the spectral index. Observations at other frequencies enabled the study of other diffuse sources in the field.

3.2.2 New VLA Observations & Data Reduction

We observed A115 with the VLA in November 2017 while the telescope was in the B configuration. The wide band ($1-2\,$GHz) L-band receiver was used with the frequency range allocated to 16 spectral windows of 64 channels each. The details of the observation are recorded in table 3.2. The data analysis and imaging were done using the `CASA`[2] radio analysis package, version 5.0. An initial RFI inspection of the data showed that only 70% of the data was usable. We therefore "hanning smoothed" the data and RFI was excised automatically using the `flagdata` and `flagcmd` `CASA` tasks. The standard procedure of bandpass and gain calibration was then done. Flux levels were set using the Perley and Butler (2013) scale. We used 3C48 and J0122+2502 as the flux and phase calibrators, respectively. After applying the gain solutions to the target, and splitting out the target data, imaging was performed using the `CLEAN` task in `CASA`. We then checked our flux calibration by measuring the fluxes of all the known bright compact sources in the field. Our fluxes were in agreement within the flux calibration uncertainty, usually about 5%. Several iterations of self calibration (phase only) were run in multi-scale mode with wide-field imaging enabled. When the image quality could not be improved any further, two rounds of phase-amp self-calibration were then performed. The details of the image obtained are recorded in table 3.3.

---

[2] `CASA` is developed by an international consortium of scientists based at the National Radio Astronomical Observatory (NRAO), the European Southern Observatory (ESO), the National Astronomical Observatory of Japan (NAOJ), the Academia Sinica Institute of Astronomy and Astrophysics (ASIAA), the CSIRO division for Astronomy and Space Science (CASS), and the Netherlands Institute for Radio Astronomy (ASTRON) under the guidance of NRAO.

3.2.3 New GMRT Observations & Data Reduction

GMRT Observations were carried out in July 2011 (PI: Dr. Bonafede Annalisa) using the GMRT software back-end (GCB; Roy et al., 2010). A dual frequency setup was used, recording RR polarisation at 610 MHz and LL polarisation at 241 MHz. However, the data at 241 MHz was unusable and is therefore not included in our analysis. Column 3 in table 3.2 shows the details. Data reduction was done using the `CASA` package, version 4.2.1. An initial inspection of the data was done to exclude antennae that were severely affected by RFI. The `AOFlagger` (Offringa, 2010) software package was then run on the data to remove data that is affected by RFI. The standard procedure of bandpass and gain calibration was then done, followed by a few rounds of phase self-calibration. When the resultant solutions obtained could not be improved any further, two rounds of phase-amp self-calibration were done. Fluxes were set using the Perley and Butler (2013) scale. The final images were made using the "briggs" weighting system (Briggs, 1995). The details of the image obtained are shown in table 3.3.

3.2.4 New LOFAR Observations & Data Reduction

The observation was carried out from 19-Sep-2016 to 20-Sep-2016 for a total time of 8 hours in interleaved mode, i.e. the calibrator being observed for two minutes followed by a scan on the target for about 11 minutes separated by a 1 minute gap. This allows time for beam forming and target re-acquisition (Mol and Romein, 2011; Sclocco et al., 2012). A total of 242 sub-bands were recorded over a bandwidth of 50 MHz. However, the last 15 sub-bands were unusable due to RFI contamination. Each sub-band is composed of 64 channels over a bandwidth of 195 kHz. The integration time for the observation was set to 2 seconds for both the calibrator and target. All the four polarisations were recorded. The field of view for the HBA station field is around 5 degrees FWHM. For the case of our study, we used only the Dutch stations, a total of 62 stations.

After obtaining the data from the observatory, the `pre-FACTOR` pipeline was used for a direction independent calibration. The data calibration performed by the `pre-FACTOR` pipeline is described in van Weeren et al. (2016) and Williams et al. (2016). The basic steps are as follows: Each sub-band is flagged of RFI using `AOFlagger` (Offringa, 2010), and averaged in time to 10 seconds per sample and in frequency by a factor of 16, resulting in 4 channels per sub-band in the output data. The calibrator data are used to derive amplitude solutions for each station using the `DPPP` (van Diepen and Dijkema, 2018). `DPPP` takes into account the time and frequency varying LOFAR station beams. For this calibration run, we set the flux density scale using Scaife and Heald (2012). All solutions obtained were then kept for use during the next calibration run on the target. The solutions obtained from the calibrator calibration are then applied to the target to fix the target amplitude scale. A direction independent imaging is then performed using `WSClean` (Offringa et al., 2014; Offringa and Smirnov, 2017) in order to obtain an initial model for direction dependent imaging.

The newly developed `FACTOR` pipeline was then used to perform a direction dependent self-calibration and imaging. The details of how the pipeline works are discussed in van Weeren et al. (2016). The `FACTOR` pipeline uses a set of scripts that perform the self-calibration pedagogically. Here, we present an overview which goes as follows: (1) The target data is copied and redistributed into frequency bands that are both uniformly spaced and similar in bandwidth. The number of bands is dictated upon by how many sub-bands one wants to concatenate, usually between 10 to 12 sub-bands. For each band, any frequency gaps that may arise, due to the process of making the bands uniformly spaced, are filled up with dummy data. (2) We then use `FACTOR` to divide the sky into facets making sure that each facet hosts a source that is bright enough to act as a calibrator for that field. The procedure of dividing the pointing on the sky into facets follows the Voronoi tesselation scheme (e.g., Senechal, 1993; Okabe, 2000). The threshold of how bright a source should be, in order to be chosen as a calibrator, is chosen by the user. We set this threshold to 0.3 Jy. This resulted into 60 facets for our field. (3) Using `FACTOR`, we then perform the rest of the self-calibration and imaging for each of these facets, starting from the facet with the brightest calibrator. We performed self-calibration for all the facets surrounding the target field facet before imaging the target facet. We checked our source positions and fluxes with the TGSS catalogue. Our positions and the fluxes were in agreement within 5% error. (4) We then made our final images using `WSClean` (Offringa and Smirnov, 2017). The details of a medium resolution image obtained are shown in table 3.3.

	Max. Res.	Briggs robust	Beam size	$\sigma_{\rm rms}$[mJy/beam]	Starting contour
LOFAR	$3''6$	−0.5	$18''$	0.72	$4\sigma_{\rm rms}$
WSRT	$40''5$	1.0	$98'' \times 40''$	0.83	$3\sigma_{\rm rms}$
GMRT	$5''5$	0.0	$18''$	0.64	$3\sigma_{\rm rms}$
VLA	$3''9$	0.5	$18''$	0.03	$3\sigma_{\rm rms}$

TABLE 3.3: Image parameters for all the images in fig. 3.3

3.3 The Giant Radio Relic in A115

Figure 3.3 shows radio maps from 4 observations. The image parameters of all 4 images are written in table 3.3. They all reveal the large radio relic structure that starts from the Northern cluster component A115N and extends towards the north east, a region with low ICM density. The morphology is maintained from 1.5 GHz down to 143 MHz. The structure is classified as a radio relic partly because of its location and longitudinal alignment with respect to the cluster centre. The tentative spectral index obtained by Govoni et al. (2001) is another factor that led to the tentative classification as a radio relic.

Based on additional observations at 350 MHz with the WSRT, Drabent (2017) confirms the classification. Since the resolution achievable with the WSRT data was not sufficient to discretise the two galaxies close to the relic, additional observations were required in order to study the relic better. Using the GMRT at 610 MHz, we obtained radio maps that could be used for spectral index analyses as discussed in section 3.3.2. The results at 610 MHz confirmed the nature of the source and the relic spectral index between 610 MHz and 1.4 GHz (Dumba et al., 2015).

We argue that such an extended diffuse radio source cannot be remnant emission from a radio galaxy. For a wider spectral study, we finally use data from the LOFAR telescope at 143 MHz. The radio map is in agreement with all previous studies as shown in fig. 3.3.

With the 3C28 radio source becoming increasingly brighter (25 Jy) at 143 MHz, a high dynamic range (DR)[3] is required in order to obtain a low noise image. The highest DR ever achieved while imaging at 143 MHz is 10 000, yet we need 125 000. With a careful analysis, we mitigate the artefacts created due to insufficient deconvolution (`CLEANing`) by employing calibration techniques which involve flagging poor solutions after each round of self-calibration. The

---

[3] Dynamic range (DR) = $\frac{\text{Peak flux}}{\sigma_{\rm rms}}$.

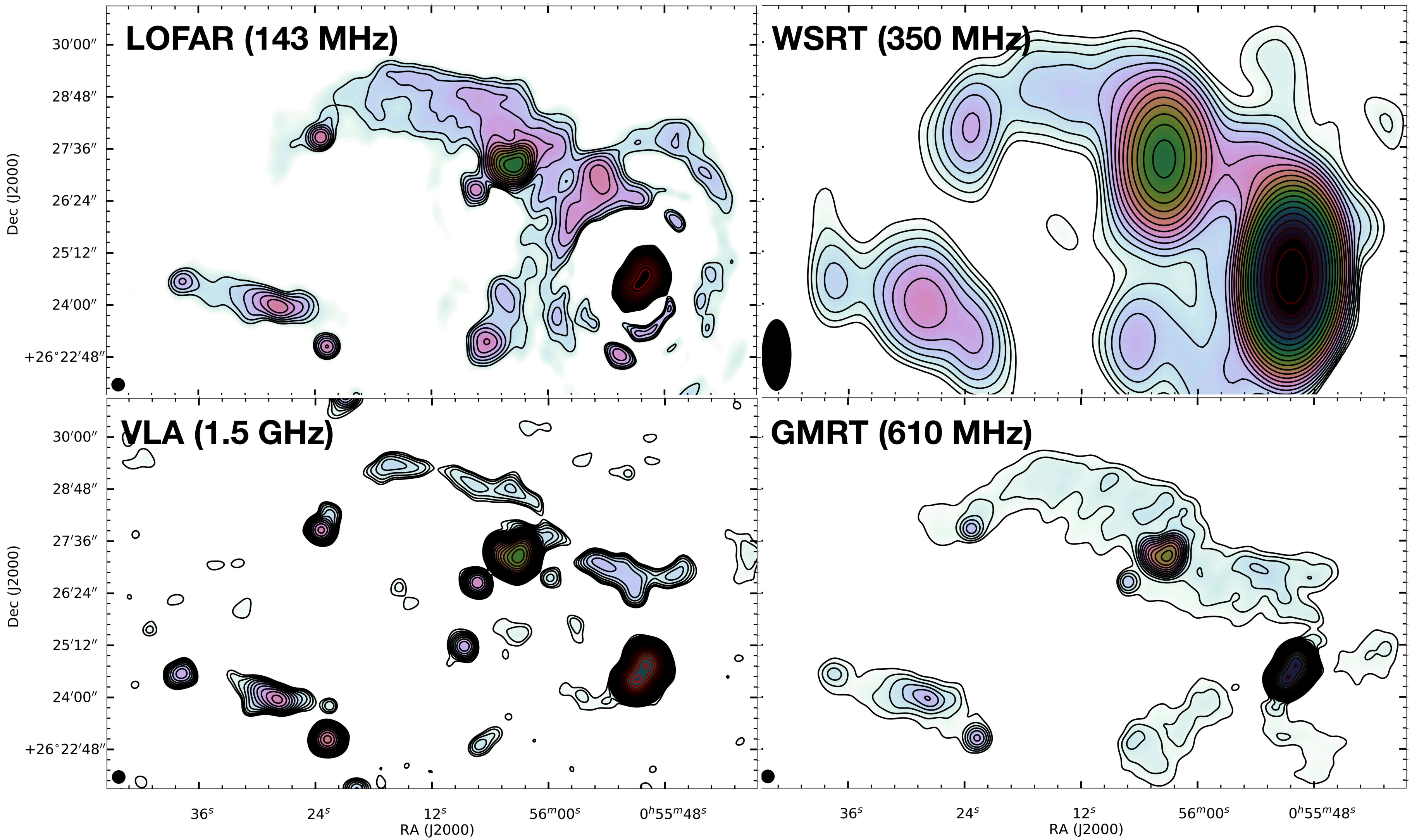

FIGURE 3.3: A115 radio relic view from 4 different arrays : Top left, LOFAR (143 MHz); Top right, WSRT (350 MHz); Bottom right, GMRT (610 MHz); Bottom left, LOFAR (143 MHz). The WSRT image is obtained from Drabent (2017). Contours in all images start at $3\sigma_{\rm rms}$ and increase in steps of $sqrt2$. The radio relic morphology is maintained even at the lowest frequency. The LOFAR image shows how challenging it can be to image a field with a very bright (3C28: 25 Jy) radio source.

top left panel of fig. 3.3 shows the final image obtained. A few artefacts are still visible in the region surrounding the bright 3C28 source. However, the left part of the relic is recovered properly; in agreement with the structure obtained at other frequencies.

3.3.1 Relic Structure & Merger Scenario

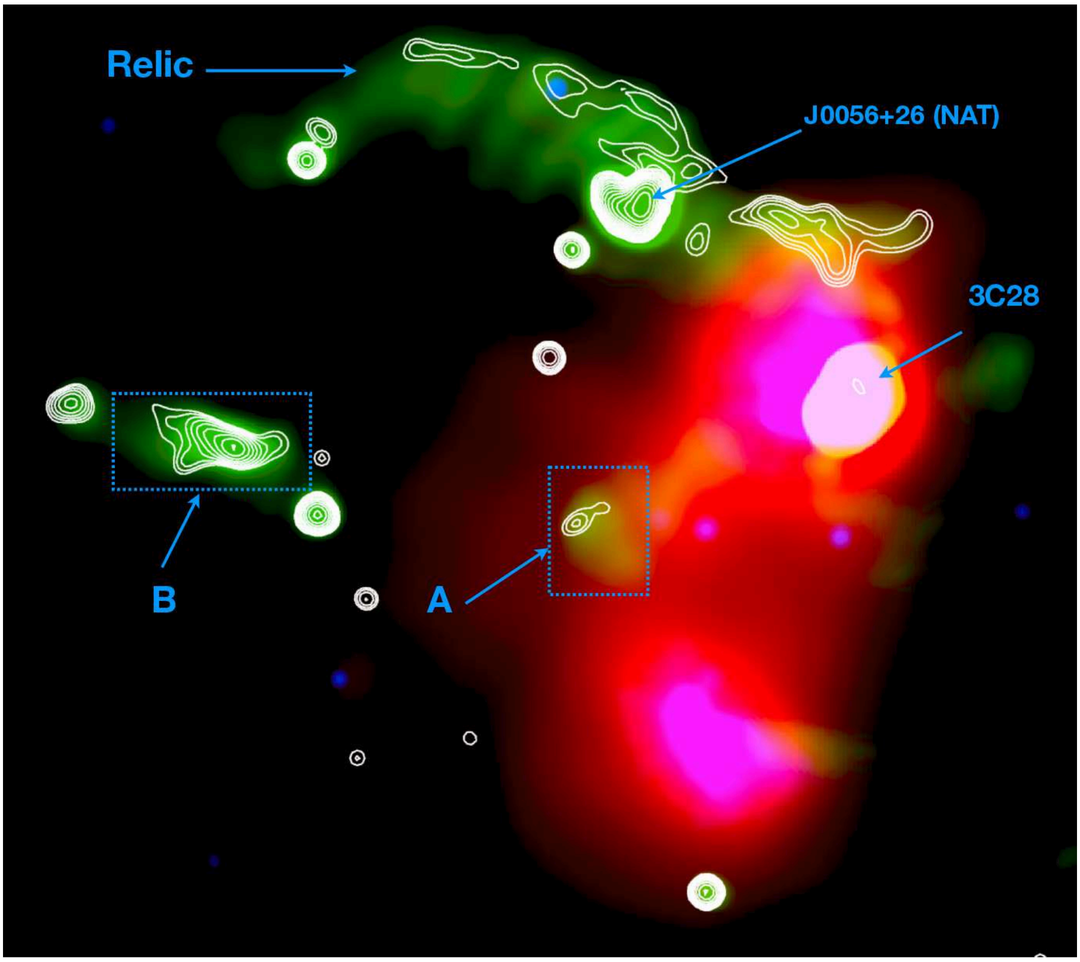

FIGURE 3.4: Abell 115 radio relic as seen with the GMRT and VLA. The VLA image contours (white) are overlaid onto the GMRT radio relic emission (green) and XMM Xray (magenta-red). The resolutions are $18'' \times 18''$ and $5'' \times 5''$ for the GMRT and VLA, respectively; the noise level for the GMRT image is 700 μJy/beam. VLA contour levels start at $3\sigma_{\rm rms}$ where $\sigma_{\rm rms}$=30 μJy/beam.

The VLA ($1 - 2$ GHz) image contours (white) are shown in fig. 3.4 overlaid onto the GMRT image (green) and the *XMM-Newton* X-ray surface brightness (red-magenta). The contours show the extent of the radio relic at 1.5 GHz (VLA B-configuration only). The relic emission is elongated in such a way that part of it lies deep in the ICM while the rest extends outward to a region with very low ICM density. We label the relic region that lies deep in the ICM as relic E and that that lies in the low-density environment relic W. The total extent of the relic is about 2.1 Mpc. The shape and extension are similar to that previously shown by Govoni et al. (2001). The majority of radio relics in literature lie in the outskirts of the galaxy clusters. However, the relic placement in A115 lies obliquely to the X-ray morphology centroid, just like the radio relic in the *toothbrush* cluster (Rajpurohit et al., 2018). This, together with other considerations, suggests that the merger in A115 is off-axis, with more than the two sub-components involved (Hallman et al., 2018). Figure 3.5 shows a pictorial representation of the most likely scenario that describes how the two main sub-cluster components are merging. The direction of travel for A115N is partially supported by the shape of the lobes of the NAT galaxy. NATs are subjected to the pressure induced by the ICM as they travel through the ICM. This confines the jets to a narrow cocoon leaving behind tails of radio emission (see section 1.3).

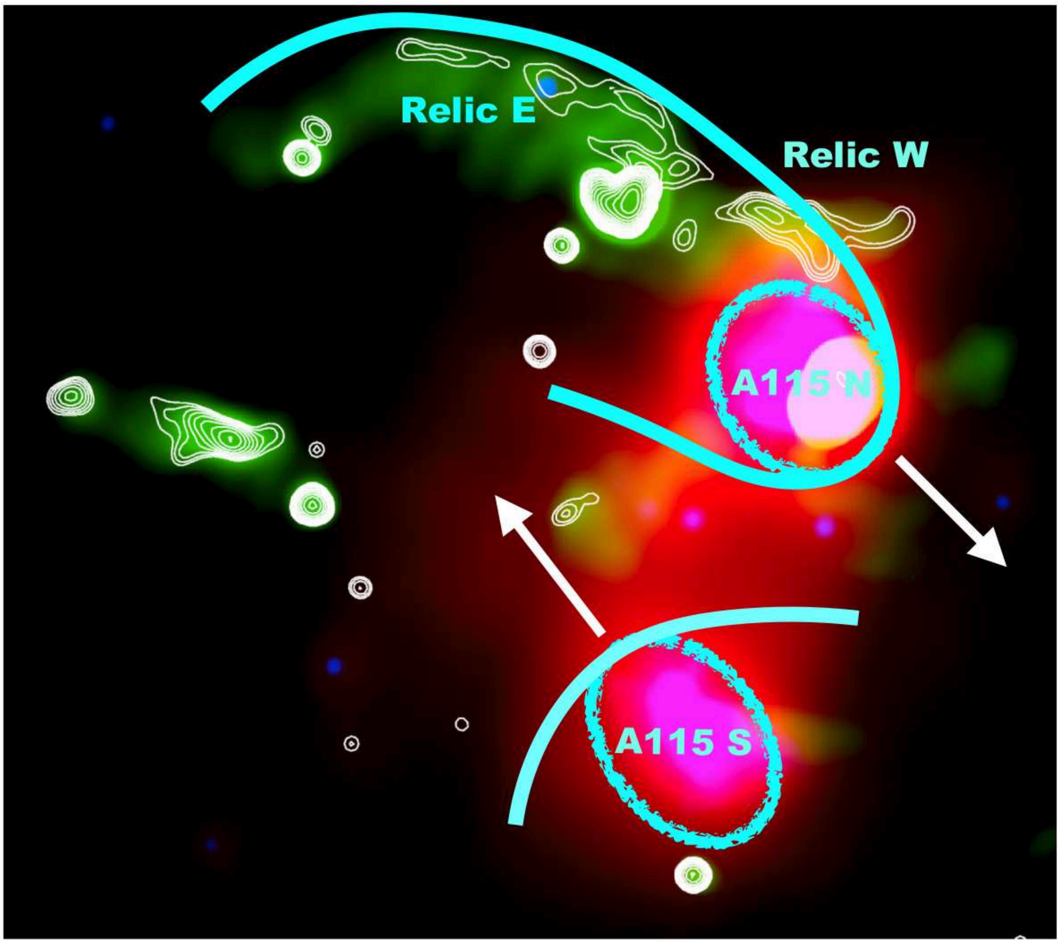

FIGURE 3.5: Pictorial illustration of the merger in A115 showing the two sections of the radio relic, relic E and relic W.

3.3.2 Spectral Analysis

A spectral index map was computed using the LOFAR and VLA images. It was created by fitting a single power-law for the flux density measurements at the two frequencies. The procedure suppress errors due to RFI, calibration, deconvolution, and different UV coverages as long as they do not correlate at the same location and spatial frequencies on the sky. For regions where the noise level falls below $3\sigma_{\rm rms}$, the pixels were blanked. For the remaining pixels, a spectral index value and the corresponding error for each pixel were estimated using:

$$\alpha = -\frac{\ln \frac{\mathcal{S}_1}{\mathcal{S}_2}}{\ln \frac{\nu_1}{\nu 2}}, \tag{3.1}$$

and

$$\Delta\alpha = -\frac{1}{\ln \frac{\nu_1}{\nu 2}} \sqrt{\left[\frac{\Delta\mathcal{S}_1}{\mathcal{S}_1}\right]^2 + \left[\frac{\Delta\mathcal{S}_2}{\mathcal{S}_2}\right]^2}, \tag{3.2}$$

where the total error within each flux density measurement, $\mathcal{S}_{\rm i}$, is $\Delta\mathcal{S}_{\rm i} = \sqrt{(\sigma^i_{\rm rms})^2 + (f_{\rm err}\mathcal{S}_{\rm i})^2}$; the subscripts $i = [1, 2]$ representing $[144, 1512]$ MHz. The total error is due to the flux scale uncertainty, $f_{\rm err}$[4] and the image noise level, $\sigma_{\rm rms}$. The result is shown in fig. 3.6 (bottom panel).

A down stream spectral index steepening is clearly visible for the eastern section of the relic, from 0.9 to 1.4. This is similar to what is observed in a number of radio relics and is as a result of energy losses through synchrotron and IC processes (see e.g., Stroe et al., 2016; Rajpurohit et al., 2018, for the *sausage* and *toothbrush* relics, respectively). There is also a tight correlation between the brightest parts of the relic and flat spectra. The western part of the relic is uncertain due to severe artefacts associated with the bright 3C28 source. The direction of the steepening rules out the possibility that the extended diffuse emission is part of the NAT galaxy. We attribute the diffuse radio emission to (re)acceleration of electrons via a shock front.

Radio relics are argued to be tracers of regions where shocks have (re)accelerated particles via the DSA mechanism.

Assuming that the shock properties remain the same and that the age of the shock is much larger than the electron cooling time, the integrated spectrum will be described by a power law whose spectral index is an additional 0.5 units

---

[4] $f_{\rm err} = 15\%, 10\%,$ and 5% for LOFAR, GMRT, and VLA observations respectively.

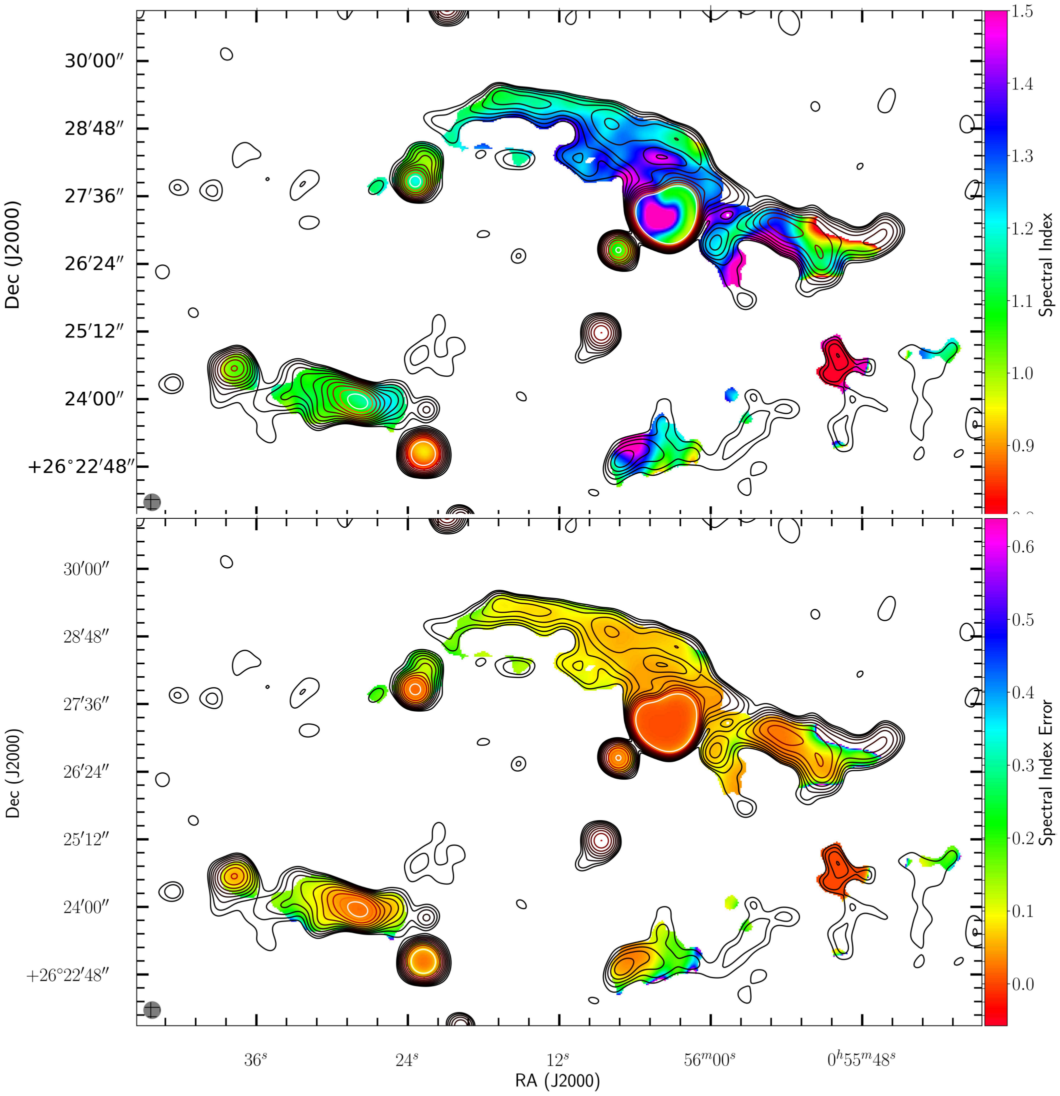

FIGURE 3.6: Abell 115 radio relic spectral index map between 143 MHz & 1512 MHz

steeper than α_{inj} (see e.g., Blandford and Eichler, 1987; Sarazin, 1999; Miniati, 2002; Sarazin, 2002, or as described in section 1.4.2).

To estimate the integrated spectral index across the shock region, we trace the shock region spectral index using boxy pandas (not shown) whose size is equal to that of the beam. We obtain an average integrated spectral index between 143 MHz & 1,420 MHz of 1.17 ± 0.10. The spectral index obtained is in agreement with that previously obtained by Dumba et al. (2015) and Govoni et al. (2001). This would imply that $\alpha_{\text{inj}} = 0.67 \pm 0.10$ for a simple shock model. This is close to the flattest possible spectral index expected from DSA of about 1.0, only possible if the relic has just been brightened. We argue that this is possibly the case as the dynamic state of the galaxy cluster suggests a pre-merger. The close proximity of the presumed shock to the cluster centre

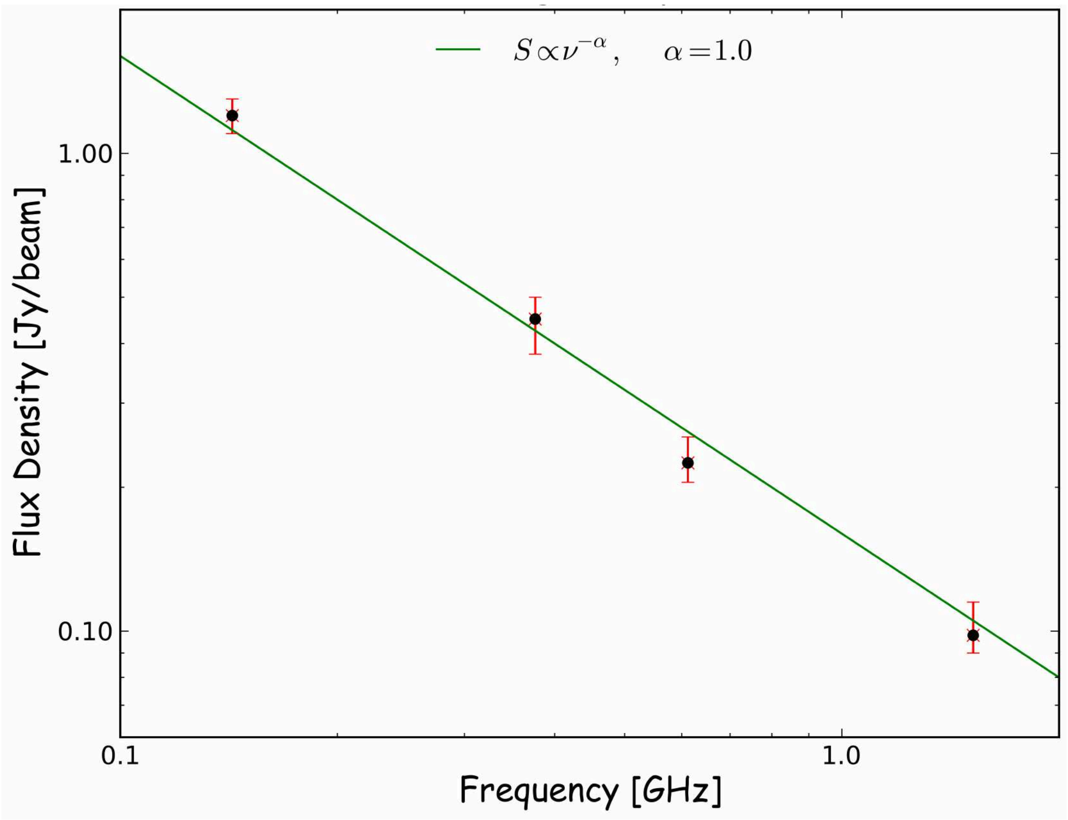

FIGURE 3.7: Abell 115 radio relic integrated spectrum between 143 MHz & 1,420 MHz

also suggests that the shock has not yet had enough time to travel outwards, an indication of an early ongoing merger.

The injection spectral index, $\alpha_{\rm inj}$, is linked to the Mach number, $\mathcal{M}$, of the shock wave by eq. (1.13).

This results in a Mach number $\mathcal{M} = 3.6^{+2.0}_{-0.9}$. The uncertainty in the Mach number is due to the variation in spectral index across the shock region of about 0.1. The Mach number obtained is in agreement with those found in other similarly massive merging clusters (see e.g., Kierdorf et al., 2017, and in section 1.4.2).

3.3.3 Polarisation

Shocks are known to compress the magnetic field at the shock front and therefore increase the magnetic field strength in that region. The increased magnetic flux results in the presence of ordered magnetic field lines which are observable in polarisation maps. We obtain polarisation intensity and polarisation fraction maps using archival VLA data as shown in fig. 3.8. The lower left panel shows

B-vectors overlaid onto the polarised intensity image, showing that the magnetic field vectors are aligned along the relic extent. The map also reveals that the western part is depolarised whereas eastern part is polarised. This is consistent with the idea that the western part lies within or behind the dense ICM of A115N. The ICM acts as a depolariser as shown for the *toothbrush* relic (Kierdorf et al., 2017; Rajpurohit, 2018). The alignment of the relic in A115 is similar to that of the *toothbrush* relic. We plan to obtain further information on the relations between the polarised emission and the shock front using future wide band VLA observations.

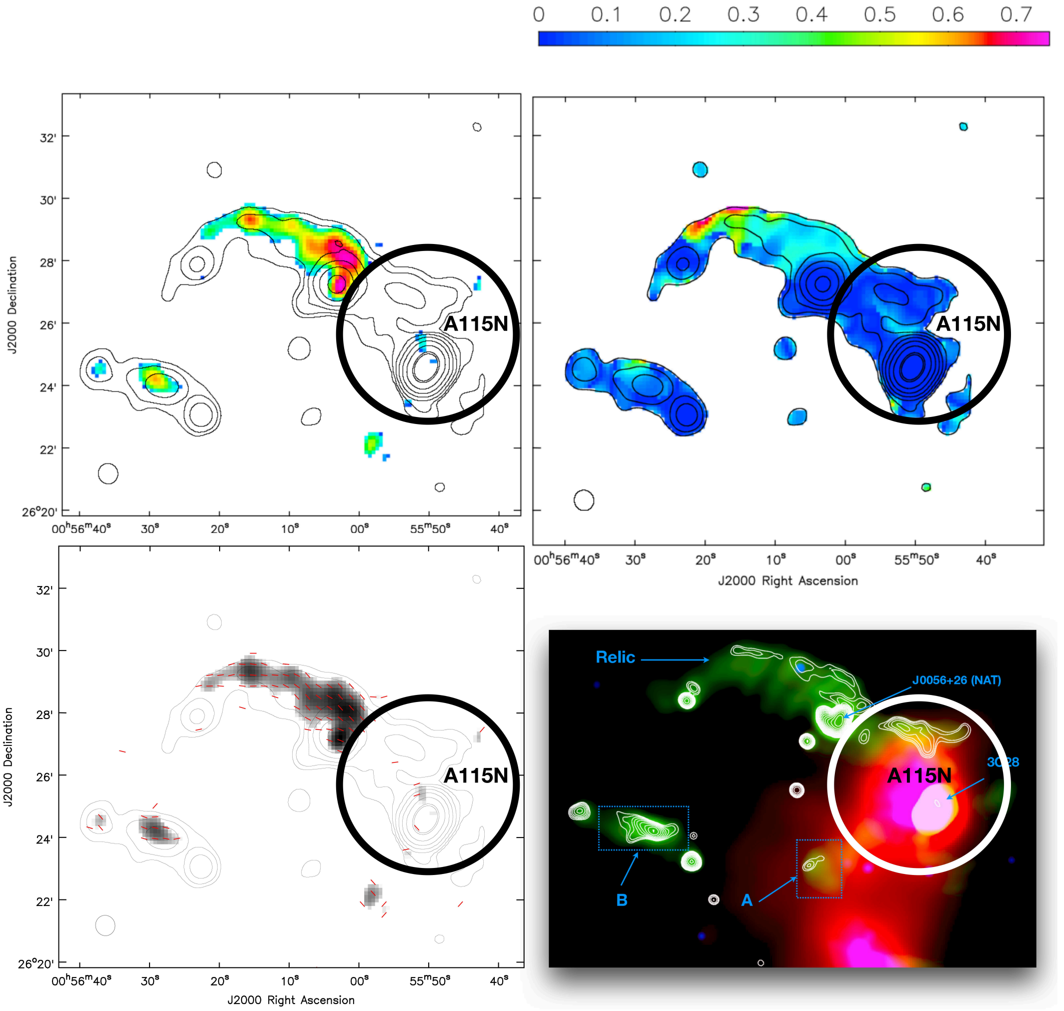

FIGURE 3.8: Polarised intensity map (top left) & polarisation fraction map (top right) of the radio relic in A115. The B-vectors (red) over plotted onto the polarised intensity are shown in the lower left panel. The region of the relic that coincides with the northern sub cluster component is depolarised.

3.3.4 Equipartition Magnetic Field

If a synchrotron source containing any arbitrary distribution of electron energies is optically thin ($\tau \ll 1$), then the low-frequency spectrum will be the superposition of the spectra from the individual electrons. This spectrum never rises more rapidly than the $\frac{1}{3}$ power of the frequency, i.e.

$$\alpha \equiv \frac{-\mathrm{dlog}\,\mathrm{S}_\nu}{\mathrm{dlog}\,\nu} > \frac{-1}{3}. \tag{3.3}$$

Indeed, many astrophysical radio synchrotron sources have spectral indices $\alpha > 0.7$. For the radio halo in A1430, we obtained a spectral index of about 1.2. This overall spectral index reflects the electron energy distribution. We can write this electron energy distribution as

$$N(\varepsilon)\mathrm{d}\varepsilon \approx N_0\varepsilon^{-\delta}\mathrm{d}\varepsilon, \tag{3.4}$$

where $N(\varepsilon)\mathrm{d}\varepsilon$ is the number of electrons per unit volume with energies $\varepsilon\, to\, \varepsilon{+}d\varepsilon$. The relativistic particle energy density can then be given by

$$\varepsilon_{\mathrm{CRe}} = \int \varepsilon N(\varepsilon)\,\mathrm{d}\varepsilon. \tag{3.5}$$

To derive a zero-order estimate of the magnetic field strength averaged over the entire source volume, we assume that the extended diffuse radio source in the cluster is in a minimum energy condition. Under this condition, the magnetic field energy, $\varepsilon_B = B^2/(8\pi)$ is comparable to the relativistic particle energy and so are their energy distributions. From the derivation of the energy budget of a synchrotron source using eq. (3.4) and eliminating ε in favour of ν/ν_{G}, where $\nu_{\mathrm{G}} \propto B$, we can compare the slopes of the distribution to get

$$\alpha = \frac{\delta - 1}{2}. \tag{3.6}$$

For a spectral index $\alpha = 1.17 \pm 0.10$, we obtain $\delta = 3.34 \pm 0.10$.

The total minimum energy density $u_{\mathrm{min}} = U_{\mathrm{min}}/V\Phi$. Equation (1.18) shows how this is expressed in observable parameters after assuming $\Phi = 1$, i.e. the same volume of particles and the magnetic field, and applying the $k-correction$. The factor $f(\alpha, \nu_1, \nu_2) = 3.8^{+1.0}_{-0.5} \times 10^{-13}$, when computed for $\alpha = 1.17 \pm 0.10, \nu_1 = 10\,\mathrm{MHz}$, and $\nu_2 = 100\,\mathrm{GHz}$.

The size of the relic along the line of sight, d, is estimated from the intrinsic width of the relic, $w_{\rm int}$. The intrinsic width of the relic is in turn estimated from the downstream plasma velocity with respect to the shock. The downstream specific energy density determines the downstream plasma velocity (Hoeft and Brüggen, 2007). For typical clusters, with a temperature of 6.5 keV, the velocity is about 1300 km/s. Using the geometry of a cross-section of a sphere to represent a relic, the size of the relic along the line of sight, d, can be written in terms of the intrinsic width, $w_{\rm int}$, and the distance from the cluster centre $R_{\rm cc}$ as

$$d \sim 2\sqrt{w_{\rm int} R_{\rm cc}}\,. \tag{3.7}$$

A 50 kpc intrinsic width of a relic that is 1.3-1.6 Mpc from the cluster centre results in an average length along the line of sight, d, of about 540 kpc. For the selected cross-section of the relic in A115, we therefore use $\alpha = 1.17 \pm 0.10$, $d \sim 540\,\mathrm{kpc}$, and $I_0 \sim 2.1 \times 10^{-1}\mathrm{mJy\,arcsec^{-2}}$ at 1.5 GHz to estimate the magnetic field strength at which the total energy content is minimum.

The magnetic field strength at which this minimum value of the total energy content is obtained is then derived from eq. (1.20). We obtain $B_{\rm eq} = 3.82^{+0.23}_{-0.55}\,\mu G$. However, a more precise way of estimating the energy budget in the relativistic particles is to use the Lorentz factors, γ_1 and γ_2, instead of the frequency cut-offs, ν_1 and ν_2. Assuming that $\gamma_1 \ll \gamma_2$, Brunetti et al. (1997) and Beck and Krause (2005) derive the equipartition magnetic field strength as

$$B'_{\rm eq} \approx 1.1\gamma_{min}^{\frac{1-2\alpha}{3+\alpha}}\, B_{\rm eq}^{\frac{7}{2(3+\alpha)}}\left[\mathrm{erg}^{\frac{1}{2}}\ \mathrm{cm}^{-\frac{3}{2}}\right]. \tag{3.8}$$

We estimate an equipartition magnetic field, $B'_{\rm eq} = 7.10^{+0.85}_{-1.29}\,\mu G$.

3.4 The diffuse radio sources A & B

The A115 cluster field is host to other sources of uncertain origin. We label the sources A and B as shown in fig. 3.4. The emission is diffuse in nature and slightly extended. Figure 3.9 and fig. 3.10 show an overlay of the radio emission contours on to a DSS Optical R-band image. In each of the images, the sources A and B are further discretised into smaller components as shown.

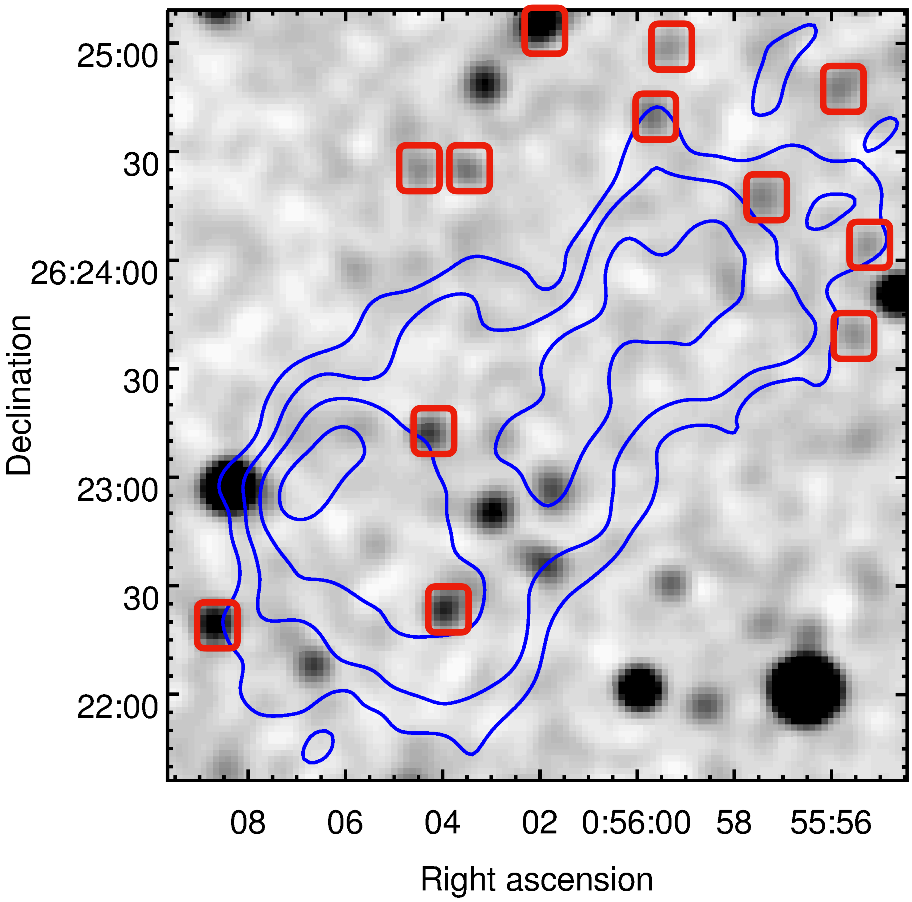

FIGURE 3.9: The overlay of the GMRT 610 MHz radio emission contours onto the optical image reveal many galaxies lie in the region. Red boxes show the location of all galaxies in the region. The peak emission is however free of any optical counterpart.

Source A is discretised into A1 and A2; Source B is discretised into B1, B2, and B3. We therefore study the morphology and where possible, the spectral index of all these sources in order to ascertain their nature.

3.4.1 Radio morphology

Source A

Source A lies close to the cluster centre in a region close to the main cluster component, A115N. This cluster field region hosts many galaxies that could have been responsible for the radio emission. We however find this possibility implausible because none of the galaxies is coincident with any peak in the radio surface brightness. Figure 3.11 shows all galaxy positions placed in the field with the GMRT low resolution radio emission in the background. The only source coincident with a radio galaxy and a peak in the radio surface brightness

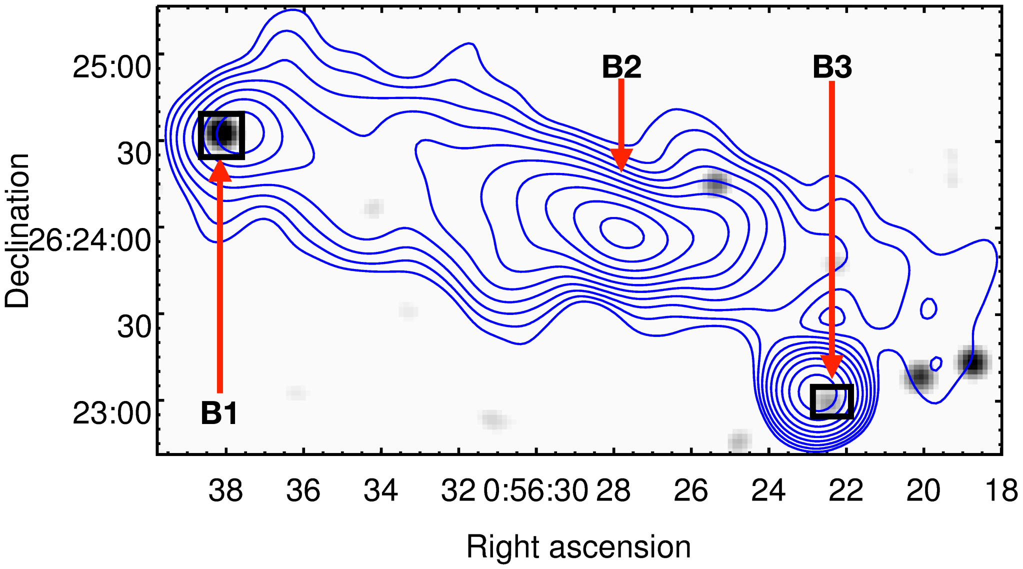

FIGURE 3.10: The overlay of the LOFAR 150 MHz radio emission contours onto the optical image reveal that B2 has no optical counterpart. Sources B1 and B3 are coincident with galaxies in the field.

being source A2. We argue that while source A2 could be emission from the radio galaxy, the main diffuse radio source A1 is not associated with any galaxy. We therefore suggest that source A1 is possibly a radio relic that could have originated from an oblique shock in the region that cannot be traced anymore. We also obtain images at high resolution (8 arcsec) and show that the source A1 does not change in nature over the frequency range from 150 MHz to 1.5 GHz (see 3.12).

Source B

The diffuse source B is composed of three sources of which the source B2 does not coincide with any radio galaxy in the field. Sources B1 and B3 are clearly radio galaxies in the field whose emission blends into that from source B2. We show in fig. 3.13 that the morphology of source B2 remains the same albeit a general increase in extension as one moves to lower frequencies. This is observed in other diffuse radio sources as well. We argue that source B2 is also a radio relic whose origin is not easy to explain. Deeper observations of the field are needed in order to perform a detailed study of the source.

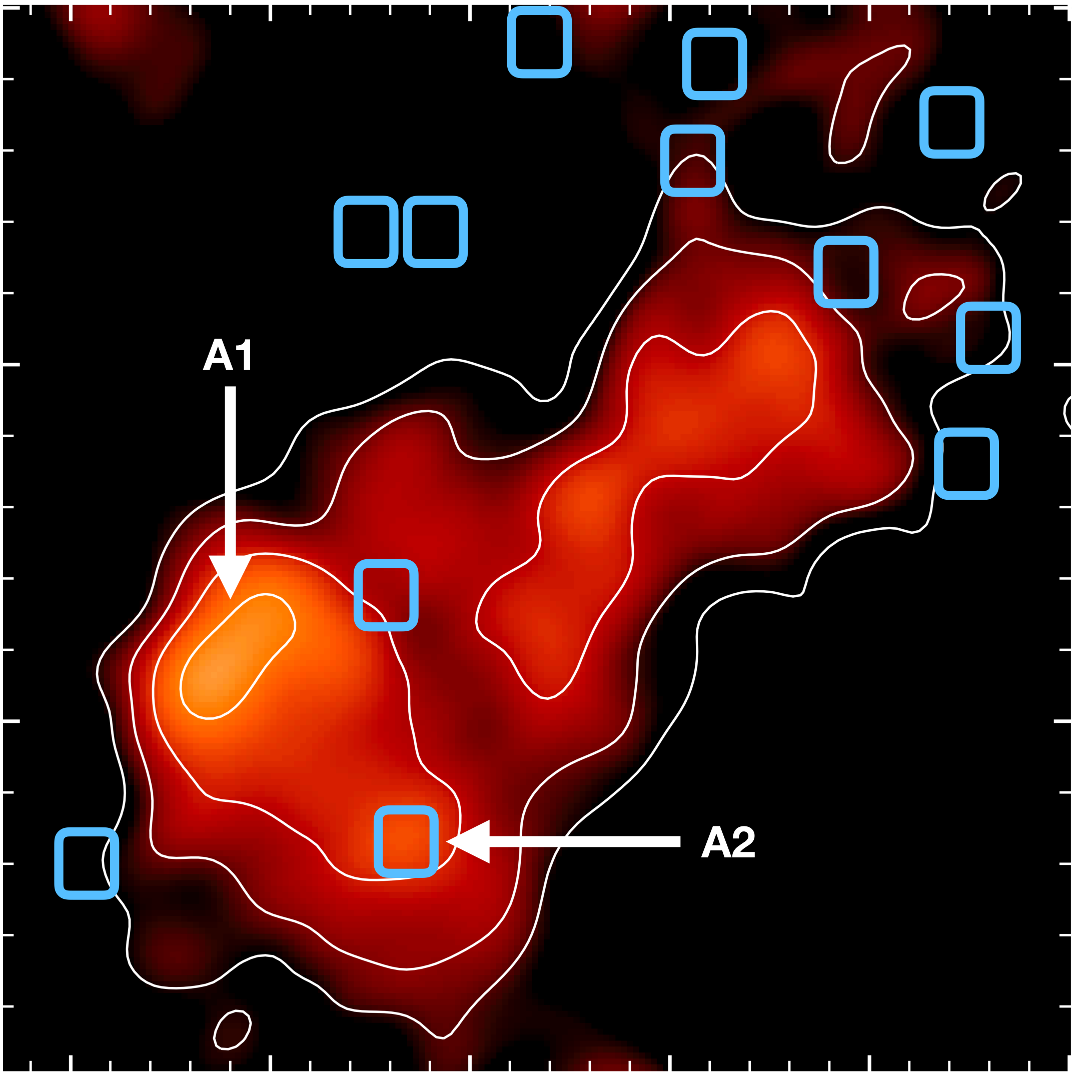

Figure 3.11: The positions of galaxies in the field marked onto the GMRT 610 MHz radio emission. Blue boxes show the positions of all galaxies in the field. Region A2 is coincident with a field galaxy whereas the region A1 does not contain any field galaxy.

3.4.2 Spectral analysis

A spectral index map source B was computed using the LOFAR and VLA images. We fitted a single power-law for the flux measurements of the two frequencies. For regions where the noise level falls below $3\sigma_{\rm rms}$, the pixels were blanked. For the remaining pixels, a spectral index and the corresponding error for each pixel were estimated using eqs. (3.1) and (3.2), respectively, where the total error with each flux density measurement, $\mathcal{S}_{\rm i}$, is $\Delta\mathcal{S}_{\rm i} = \sqrt{(\sigma^{i}_{\rm rms})^2 + (f_{\rm err}\mathcal{S}_{\rm i})^2}$; the subscripts $i = [1, 2]$ representing $[144, 1512]$ MHz. The total error is due to the flux scale uncertainty, $f_{\rm err}$[5] and the image noise level, $\sigma_{\rm rms}$. The maps are

---

[5] $f_{\rm err} = 15\%, 10\%,$ and 5% for LOFAR, GMRT, and VLA observations respectively.

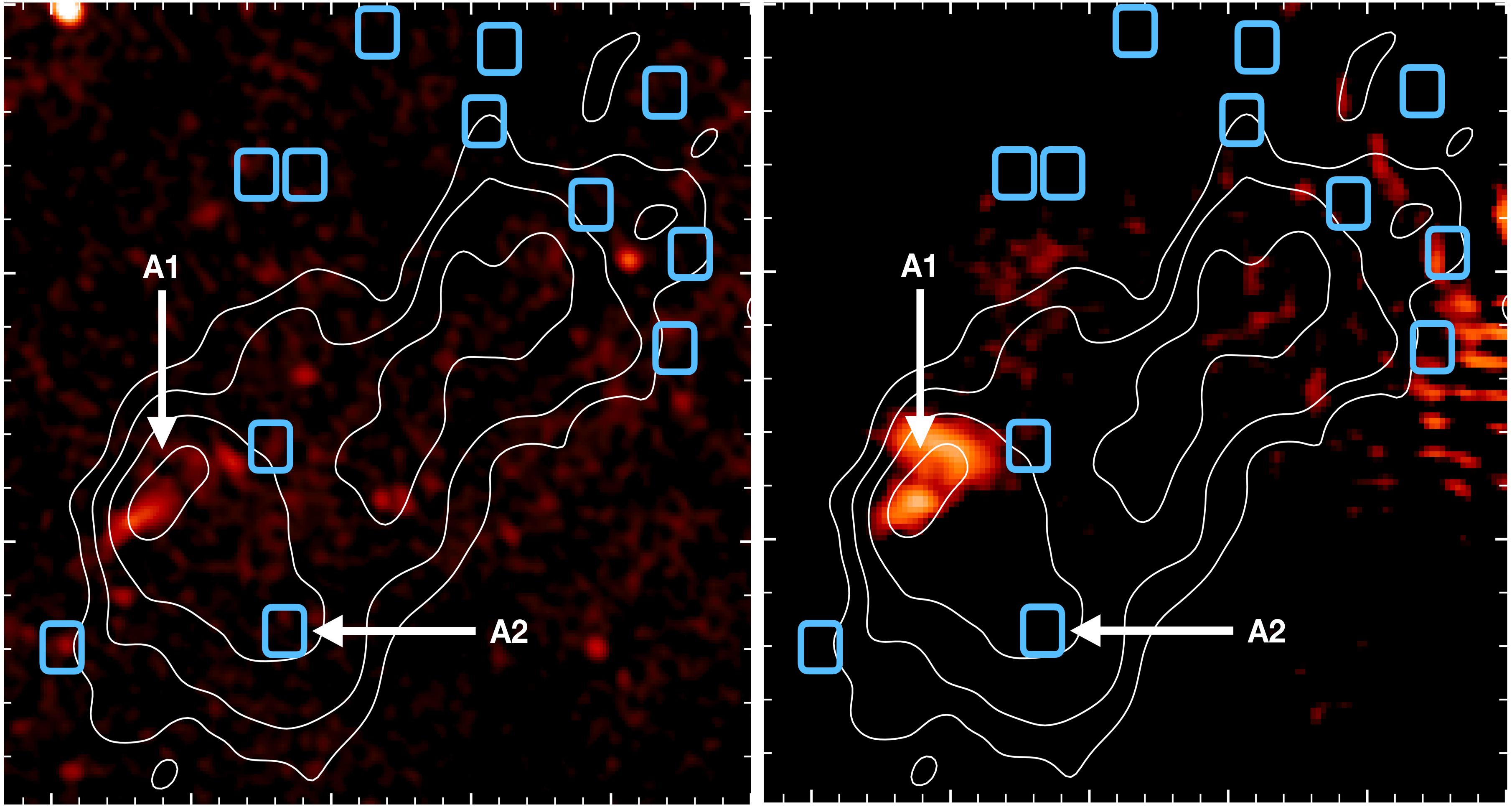

FIGURE 3.12: Region A1 as seen with LOFAR and the VLA telescopes. Blue boxes indicate the positions where galaxies are located. The A1 region does not contain any field galaxies.

shown in fig. 3.14.

The spectral index map shows a variation from an index value of 1.0 to 1.3, which is typical of radio relics. We therefore conclude that the source B2 is most likely a radio relic.

3.5 Summary

We study the merging galaxy cluster A115 using data from optical, X-ray, and radio telescopes. Merging galaxy clusters generate cluster-wide shocks which are sites of electron acceleration processes. Govoni et al. (2001) discovered a large scale synchrotron source in A115 and suggested it could be a radio relic. The spectral index obtained ($\alpha = 1.0$) was in agreement with their suggestion. The radio spectra of radio relics are steep (α of about 1). The relic position is however oblique−a part lieing in a region of low-icm-density. This is partly explained by some studies in the optical and numerical simulations which show that A115 is undergoing an off-axis merger. Off-axis mergers are known for generating peculiar shock morphologies of such a nature. The morphology and spectral index were confirmed by Dumba et al. (2015) at even lower frequencies (610 MHz). We observe the relic with LOFAR for the first time, confirming the relic structure, spectral index, and oblique alignment. Radio relics are said to trace cluster-wide merger shocks. This is confirmed for the A115 relic by Botteon et al. (2016), who find an X-ray shock the lies coincident with the western part of the relic. The eastern part of the relic lies in a low-icm-density environment making X-ray analyses in this region challenging. We perform full-stokes radio continuum observations of the cluster using the new VLA wide-band L-band receiver ($1 - 2$ GHz). We show that the relic is polarised and the integrated radio spectrum is consistent with particle acceleration in the shock region by DSA. An inference to the Mach number suggests a value of $\mathcal{M} = 3.6^{+2.0}_{-0.9}$ for the shock, in agreement with that previously estimated in the X-ray by Botteon et al. (2016). Tentative polarisation analyses indicate that the ICM depolarises part of the relic. We suggest that the depolarised part of the relic lies either deep within or behind the dense ICM.

Future deep VLA observations will shed more light on the polarised structure of the relic, and therefore the detailed magnetic field properties of the ICM.

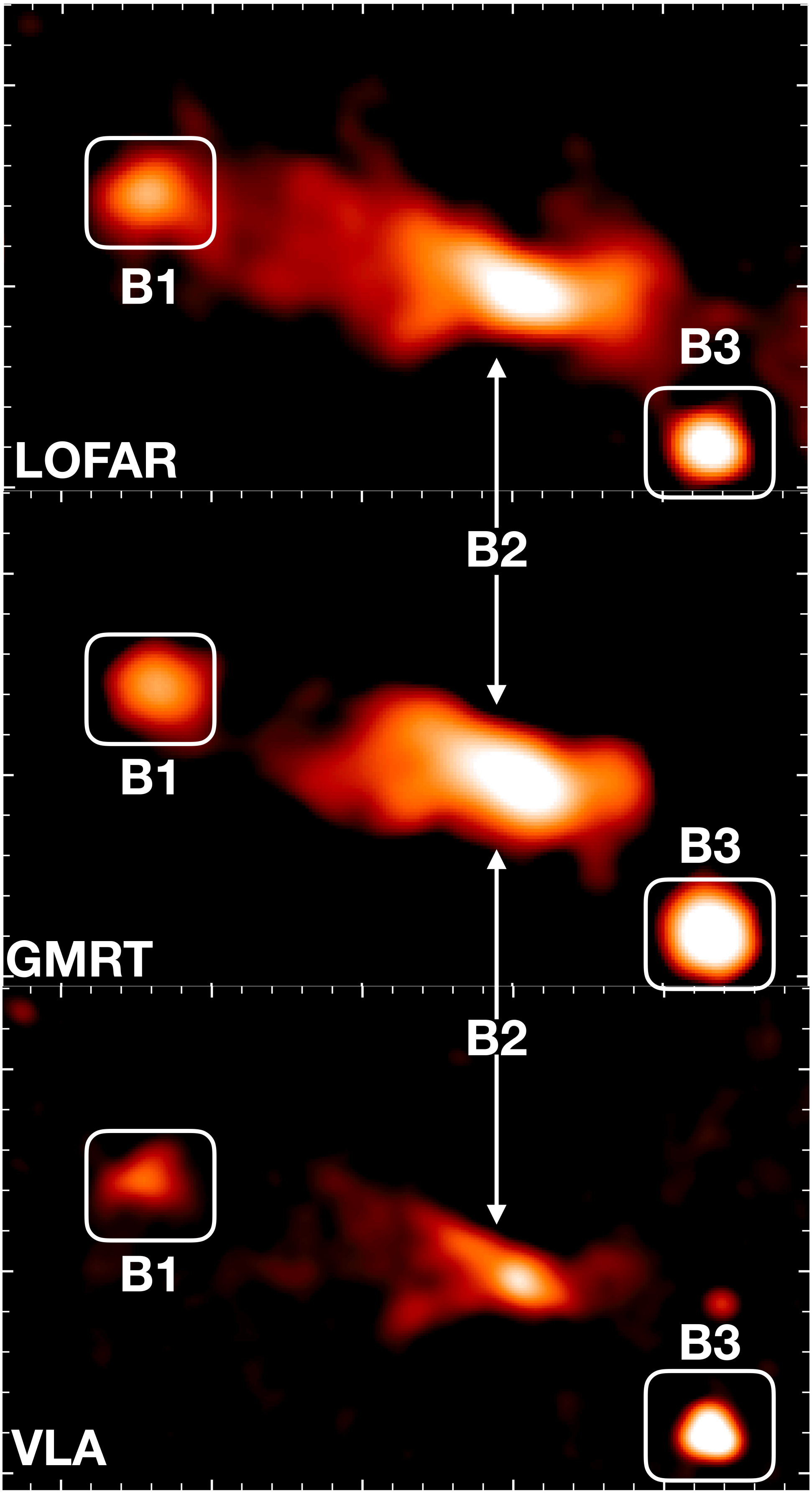

FIGURE 3.13: 18″ resolution images of the diffuse radio source B2 at three different frequencies. The source becomes more extended at lower (LOFAR) frequencies.

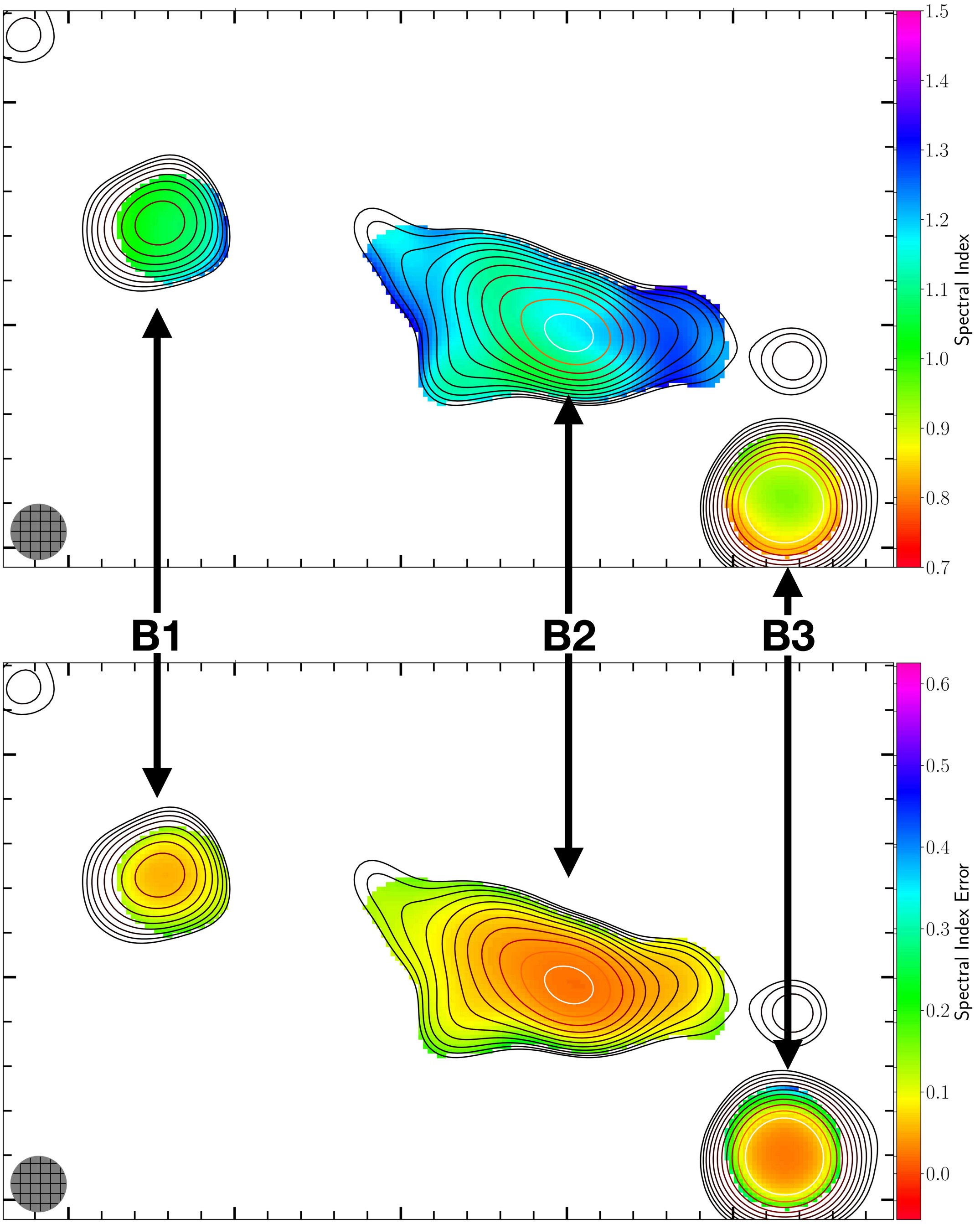

Figure 3.14: Spectral Index map generated for source B. The B2 source shows a spectral index whose value varies from 1.0 to 1.3. The source B3 has a flat spectral index of less that 0.8 while B1 displays a signature spectral index gradient typical for tailed galaxies, i.e., flat at the head and steep along the tail.

Chapter 4

A Radio Halo in Abell 1430

This chapter details the observation, analysis, and interpretation of results for the merging galaxy cluster Abell 1430. The cluster is located in an area of the sky that is covered by LoTTS, a low frequency sky survey of the northern hemisphere. Sky images showed that the cluster could be hosting a large radio halo, and therefore worthwhile to study the field in detail. We re-analysed the data from the pointing, performing a careful direction dependent calibration and imaging with the `FACTOR` pipeline. Images at both high and low resolution were made and the discrete sources were subtracted in order to measure not only the total extent of the radio halo, but also its flux density, reliably. We were fortunate enough to obtain data of the same field from the VLA data archive. With this, a tentative spectral index analysis was performed. The radio surface brightness was also compared with the X-ray surface brightness in order to understand the extent to which the thermal plasma correlates with the radio synchrotron plasma. From our study, we argue that: (1) The extended diffuse radio emission in A1430 is a two-component radio halo. (2) The properties of the radio halo synchrotron emission are related to those of the X-ray emission in the same volume. (3) The radio power of the radio halo in A1430 and the X-ray luminosity of A1430 are consistent with the correlation between radio power and cluster X-ray luminosity of the previously found radio halos[1]. (4) Observations of galaxy clusters with LOFAR improve our understanding of the electron acceleration processes in galaxy clusters since LOFAR is more sensitive to fainter sources than other arrays. (5) Less powerful radio radio halos can be studied at lower frequencies where their flux density is higher.

---

[1] The mass of a cluster correlates with the cluster's X-ray luminosity.

4.1 Introduction

Abell 1430 ($z = 0.35$), hereafter A1430, was first listed as a cluster in a catalogue of 2712 rich clusters of galaxies found in the National Geographic Society Palomar Observatory Sky Survey (Abell, 1958). The catalogue lists 31 cluster members, making A1430 have a richness class of 0. It was also listed in the Northern ROSAT All-Sky (NORAS) Galaxy Cluster Survey as one of the extended X-ray sources, namely RXC J1159.2+494 (Böhringer et al., 2000).

Recent studies have provided further details about A1430: the $Y_{\mathrm{SZ},500}$[2] and its associated M_{500}[3][4] (Planck Collaboration et al., 2014a).

Most recently, under the Legacy Programme for Massive Clusters of Galaxies [5], A1430 was observed by the *Chandra* X-ray telescope (Andrade-Santos et al., 2017). The X-ray images analysed in section 4.2.3 of this thesis were obtained using *Chandra* observations from this programme.

The X-ray observations reveal that the cluster is composed of at least two sub-components; these sub-components are seen as peaks in the X-ray surface brightness, having a separation of about 300 kpc. There are a few discrete radio sources that are close to the X-ray surface brightness peaks. The radio sources are cluster radio galaxies. We compute the X-ray luminosity (0.1−2.4 keV) of A1430 within R_{500} to be $L_{\mathrm{X},500} = 6.60 \pm 0.14 \times 10^{44}\,\mathrm{erg\,s^{-1}}$. A global electron temperature of 6.74 ± 0.73 keV is reported for this cluster by Morandi et al. (2015). Table 4.1 lists all the available properties of A1430.

4.2 Observations & Data Reduction

A study of A1430 in the radio has not been performed before. The LOFAR Two Meter Sky Survey (LoTSS)[6], has made it possible to study A1430 using data from a pointing in which it lies. The data was obtained using the LOFAR High Band Antennas (LOFAR-HBA). The description of the LOFAR-HBA is

---

[2] The Sunyaev Zel'dovich (SZ) signal for a mass enclosed by R_{500}.

[3] The mass enclosed by R_{500}.

[4] R_{500} is the radius within which the average matter density is 500 times the critical density of the universe.

[5] http://hea-www.cfa.harvard.edu/CHANDRA_PLANCK_CLUSTERS/

[6] The LoTSS will cover the entire northern hemisphere providing properties of radio sources that lie in the northern hemisphere at 143 MHz in great detail.

TABLE 4.1: A1430 properties

Property	Value	Reference
Position	$11^{\rm h}59^{\rm m}17.4^{\rm s}$ $49^\circ47'37''$	1
z	0.35	2
Physical scale [kpc/″]	5.00	this work
M_{500} [$\mathrm{M}_\odot$]	$7.35^{+0.57}_{-0.61} \times 10^{14}$	5
Y_{500} [Mpc^2]	12.02 ± 1.72	5
$L_{\rm x}$ (0.1-2.4 keV) [$\mathrm{erg\,s^{-1}}$]	$6.60^{+0.14}_{-0.14} \times 10^{44}$	this work
$T_{\rm x}$: electron energy [keV]	$10.98^{+1.58}_{-0.68}$	this work
w: Centroid Shift	$2.06 \pm 0.75 \times 10^{-2}$	this work
$C_{\rm SB}$: Concentration (0.15-1.0 r_{500})	$2.00 \pm 0.07 \times 10^{-1}$	this work
$C_{\rm SB4}$: Concentration (40-400 kpc)	$2.79 \pm 0.30 \times 10^{-2}$	this work
δ: Cuspiness	$2.76 \pm 0.85 \times 10^{-1}$	this work
$n_{\rm core}$: Central Density [cm^{-3}]	$7.07 \pm 2.61 \times 10^{-3}$	this work
R_{500} [Mpc]	1.36	this work

Notes:(1) Abell (1958), (2) Rozo et al. (2015), (3) Planck Collaboration et al. (2014a)

TABLE 4.2: Galaxies in a 1 Mpc radius of the A1430 field obtained from SDSS. RA and DEC are listed in columns (1) & (2), type of source in (3) with its corresponding redshift in (4). The type of redshift measurement is listed in (5)

RA(deg) (1)	DEC(deg) (2)	Type (3)	Redshift (4)	Flag (5)
$11^{\rm h}59^{\rm m}14.86^{\rm s}$	$49^\circ47'48.12''$	BCG	0.35	Spec
$11^{\rm h}59^{\rm m}30.36^{\rm s}$	$49^\circ47'47.04''$	BCG	0.34	Spec
$11^{\rm h}59^{\rm m}24.96^{\rm s}$	$49^\circ49'28.20''$	G	0.36	Spec
$11^{\rm h}59^{\rm m}31.82^{\rm s}$	$49^\circ48'05.76''$	G	0.36	Spec
$11^{\rm h}59^{\rm m}33.07^{\rm s}$	$49^\circ47'28.68''$	G	0.34	Spec
$11^{\rm h}59^{\rm m}14.76^{\rm s}$	$49^\circ48'33.12''$	G	0.35	Spec
$11^{\rm h}59^{\rm m}18.46^{\rm s}$	$49^\circ50'26.16''$	G	0.33	Spec
$11^{\rm h}59^{\rm m}21.84^{\rm s}$	$49^\circ47'34.80''$	G	0.35	Phot
$11^{\rm h}59^{\rm m}13.92^{\rm s}$	$49^\circ47'41.28''$	G	0.35	Spec
$11^{\rm h}59^{\rm m}32.16^{\rm s}$	$49^\circ47'34.80''$	G	0.34	Phot
$11^{\rm h}59^{\rm m}32.09^{\rm s}$	$49^\circ46'45.12''$	G	0.34	Spec
$11^{\rm h}59^{\rm m}11.71^{\rm s}$	$49^\circ46'53.04''$	G	0.35	Spec
$11^{\rm h}59^{\rm m}14.42^{\rm s}$	$49^\circ47'16.44''$	G	0.34	Phot
$11^{\rm h}59^{\rm m}10.66^{\rm s}$	$49^\circ48'24.12''$	G	0.35	Phot
$11^{\rm h}59^{\rm m}37.06^{\rm s}$	$49^\circ49'58.44''$	G	0.34	Spec

found in section 2.1.3. For our study purpose, we use 62 stations composed of (2 × 24) core stations and 14 remote stations. With the excision of unusable channels due to radio interference (RFI), the remaining data set had a central

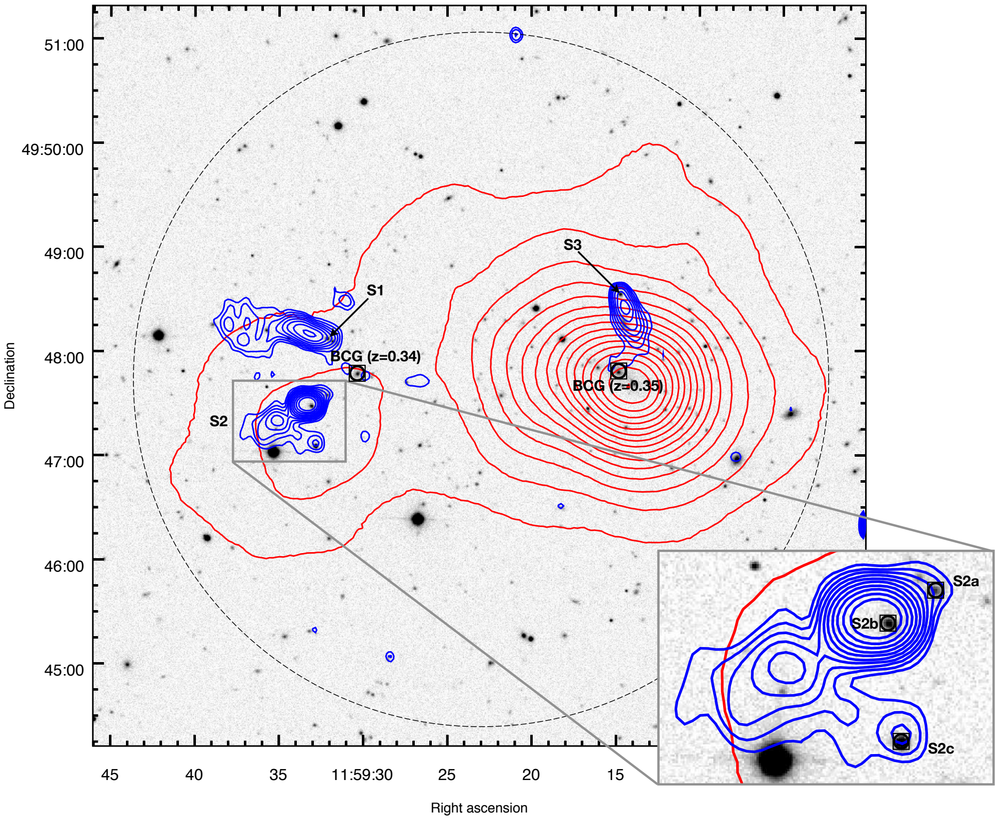

FIGURE 4.1: Brightest Cluster Galaxies in the A1430 field with their associated redshift. The black dotted circle indicates a 1.0 Mpc radius centred at the *Chandra* X-ray pointing centre. Red contours show the *Chandra* X-ray surface brightness morphology. Blue contours show the LOFAR full resolution image contours highlighting the position of the radio galaxies, S1, S2, and S3 with respect to the X-ray emission peaks. S2 is zoomed in to show that its composed of three discrete sources.

frequency of 143 MHz.

In addition, archival data from an earlier observation with the VLA L-band (1−2 GHz) was obtained (PI: A. Babul). The VLA data consists of two snapshot observations for each of the configurations B, C & D. The combination of all configurations provides a sufficient *uv* coverage. These two independent radio interferometric data sets allowed a deeper study of A1430.

The X-ray data used in this study is obtained from the data archive of the Chandra−Planck Legacy Program for Massive Clusters of Galaxies. The *Chandra* X-ray Observatory is a telescope operated by NASA to detect X-ray emission from astronomical sources. The final fits images, obtained after a careful data calibration and analysis, are used in this work.

4.2.1 LOFAR-HBA

We utilise data obtained from a LOFAR Surveys pointing. Details of the observation for the pointing are shown in the right panel of table 4.3. A total of 62 core plus remote stations were used for the observation. The maximum baseline length was 120 km. For the LOFAR-HBA, this provides a full resolution of $\sim 5''$.

The data was direction-independent calibrated using a procedure that is described in detail by van Weeren et al. (2016), Williams et al. (2016), and de Gasperin et al. (2018). In order to perform imaging on a smaller field of view that contains the cluster of interest, a direction dependent calibration is required.

We perform a direction dependent calibration and imaging using the `FACTOR` pipeline. All procedures in the `FACTOR` pipeline are also described in detail by van Weeren et al. (2016) and Williams et al. (2016, or briefly in section 2.3.2). The overall idea is to divide the pointing on the sky into facets using the Voronoi tesselation scheme (e.g., Senechal, 1993; Okabe, 2000), where each facet contains a compact radio source that is bright enough to act as a calibrator for that region. A total of 52 facets were generated for which a careful calibration was performed before the facet containing A1430 was imaged. For all facets, the level of the noise was close to 200 μJy beam^{-1}.

For the facet that includes A1430, a full resolution image was made. with a resolution of $8'' \times 5''.5$. The full resolution model was subtracted so that a point-source-subtracted low resolution image is made. The low resolution image has a resolution of $45'' \times 45''$. The rms noise level reached for the high and low resolution images was 230 μJy beam^{-1} and 450 μJy beam^{-1}, respectively. Flux measurements for all discrete sources in the field are recorded in table 4.5.

4.2.2 VLA

High frequency data was obtained from the VLA data archive. Data from two 30 minute observations performed in each of the B-,C- & D-configurations was used. Although these were snapshots, a combination of all configurations provided a sufficient *uv* coverage for the detection of extended diffuse emission at this frequency. Each of the six 30 minute observations contains four 7 minute scans of the target field, two scans for the flux calibrator[7], and four scans for the phase calibrator. The phase calibrators were observed during the intervals between the target field scans in order to track the phases reliably.

Data reduction and calibration for all the data sets from the VLA archive were carried out using the *Common Astronomy Software Applications* package (`CASA`) (McMullin et al., 2007). The flux densities were set using the Perley-Butler-2013 flux density scale (Perley and Butler, 2013).

The initial calibration process was followed by imaging in order to obtain initial model images for the self calibration process. The self-calibration included two rounds of phase only selfcalibration and one round of amplitude and phase calibration. The final imaging was performed using `WSClean`; utilising the recently included automatic masking algorithm (Offringa et al., 2014; Offringa and Smirnov, 2017).

A high resolution image was made using the B- and C-configuration data in order to obtain a model of the discrete sources. Using the C- and D-configuration data, a lower resolution image was made after subtracting the discrete sources' model. The extent covered by the diffuse emission was noted, and an estimate of the flux density measured.

TABLE 4.3: LOFAR (left) & *Chandra* X-ray (right) Observation specifications

Field Name	P18Hetdex03
Pointing centre	$11^{\mathrm{h}}\,58^{\mathrm{m}}\,49.05$
	$49^\circ\,58'\,30''.67$
Target Obs.ID	229587
Calibrator Obs.ID	229585
Cluster centre	$11^{\mathrm{h}}\,59^{\mathrm{m}}\,23^{\mathrm{s}}$
	$49^\circ\,47'\,39''$
Available stations	62
Integration time	8 h
Sampling time	2 s
Frequency range	[110-180] MHz
Usable Bandwidth	[120-166] MHz

Observation date	2014-01-04
Observation ID	15119
Sequence Number	801248
PI Name	C. Jones
RA	$11^{\mathrm{h}}\,59^{\mathrm{m}}\,23.00^{\mathrm{s}}$
DEC	$49^\circ\,47'\,39''$
Exposure time	22 ks
Band used	0.5-2.0 keV

---

[7] For each configuration, 3C147 was used for the first observation and 3C286 for the second observation.

TABLE 4.4: Details of all the available A1430 data

Telescope	ν (MHz)	TOS* (hrs)	θ_{HPBW}	θ_{LAS}
LOFAR-HBA	143	8.0	$5''$	$2500''$
VLA L-band (D)	1500	1.0	$46''$	$970''$
VLA L-band (C)	1500	1.0	$14''$	$970''$
VLA L-band (B)	1500	1.0	$4.3''$	$120''$

*Time On Source

4.2.3 *Chandra* X-ray

A1430 was observed on January 4, 2014 with the *Chandra* Observatory. The details are provided in the right panel of table 4.3. The *Chandra* data reduction followed the process described in Vikhlinin et al. (2005). We applied the calibration files `CALDB 4.7.2`. The data reduction included corrections for the time dependence of the charge transfer inefficiency and gain, and also a check for periods of high background, which were then removed (only 45 s were discarded). Standard blank sky background files and readout artifacts were subtracted.

We also detected compact X-ray sources in the 0.7–2.0 keV and 2.0–7.0 keV bands using `CIAO wavdetect` and then masked these sources before performing the spectral and spatial analyses of the cluster emission.

TABLE 4.5: Properties of the 5 discrete sources S1, S2a, S2b, S2c and S3. The source S2 could not be resolved into its discrete components at 1.5 GHz. The spectral indices of all sources are in agreement with what is expected from radio radio galaxies, a value of $\alpha \sim 0.7$.

Source	$\mathrm{RA}_{\mathrm{J2000}}$	$\mathrm{DEC}_{\mathrm{J2000}}$	$\mathcal{S}_{143\,\mathrm{MHz}}$ [mJy]	$\mathcal{S}_{1.5\,\mathrm{GHz}}$ [mJy]	$\alpha^{1.5\,\mathrm{GHz}}_{143\,\mathrm{MHz}}$
S1 [RG]	$11^{\mathrm{h}}59^{\mathrm{m}}45.9^{\mathrm{s}}$	$49^\circ48'08''$	74.7 ± 0.7	9.9 ± 0.1	0.86 ± 0.09
S2 [BS]	-	-	90.1 ± 0.9	17.5 ± 0.2	0.70 ± 0.05
S2a [RG]	$11^{\mathrm{h}}59^{\mathrm{m}}32.4^{\mathrm{s}}$	$49^\circ47'46''$	66.4 ± 0.7	-	
S2b [RG]	$11^{\mathrm{h}}59^{\mathrm{m}}34.5^{\mathrm{s}}$	$49^\circ47'23''$	19.6 ± 0.2	-	
S2c [CRS]	$11^{\mathrm{h}}59^{\mathrm{m}}32.8^{\mathrm{s}}$	$49^\circ47'06''$	3.30 ± 0.03	-	
S3 [RG]	$11^{\mathrm{h}}59^{\mathrm{m}}14.9^{\mathrm{s}}$	$49^\circ48'37''$	39.4 ± 0.4	10.8 ± 0.1	0.55 ± 0.06

Notes:- BS: Blended Sources, CRS: Compact Radio Source, RG: Radio Galaxy

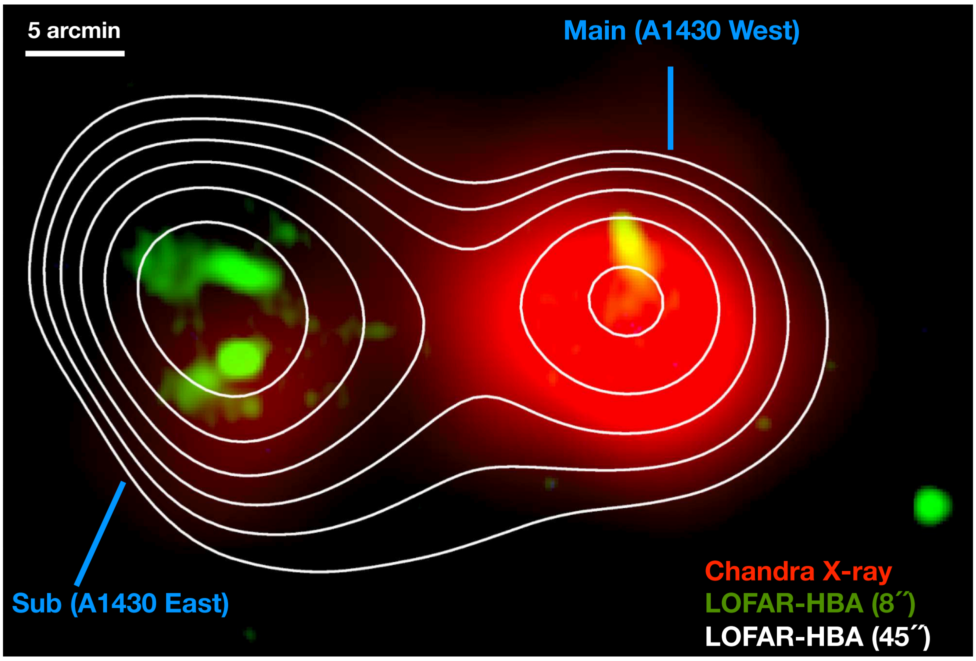

FIGURE 4.2: Abell 1430 two-component radio halo as seen with the *Chandra* X-ray telescope (red). The LOFAR-HBA radio halo contours (white) are overlaid onto the *Chandra* X-ray (red). The high resolution LOFAR-HBA image shown in green. The resolutions are $45'' \times 45''$ and $8'' \times 8''$ for the diffuse halo emission and discrete sources emission, respectively; the noise levels are 500 microJy/beam and 250 microJy/beam, respectively. Contour levels start at $2\sigma_{\rm rms}$.

4.3 Results

4.3.1 Total Intensity Maps

Total Intensity maps for both the LOFAR and VLA data are provided in fig. 4.3. The lower resolution traced with blue contours while the emission extent from the discrete sources is traced with black contours. The low resolution maps were obtained after subtracting the high resolution model from the visibilities. The maximum resolutions attainable for the LOFAR & VLA maps were $8'' \times 5''$ and $19'' \times 18''$, respectively.

The rms noise levels attained for the LOFAR and VLA low resolution maps were $450\,\mu\mathrm{Jy\,beam^{-1}}$ and $35\,\mu\mathrm{Jy\,beam^{-1}}$, respectively while the high resolution maps had rms noise levels of $230\,\mu\mathrm{Jy\,beam^{-1}}$ and $30\,\mu\mathrm{Jy\,beam^{-1}}$, respectively.

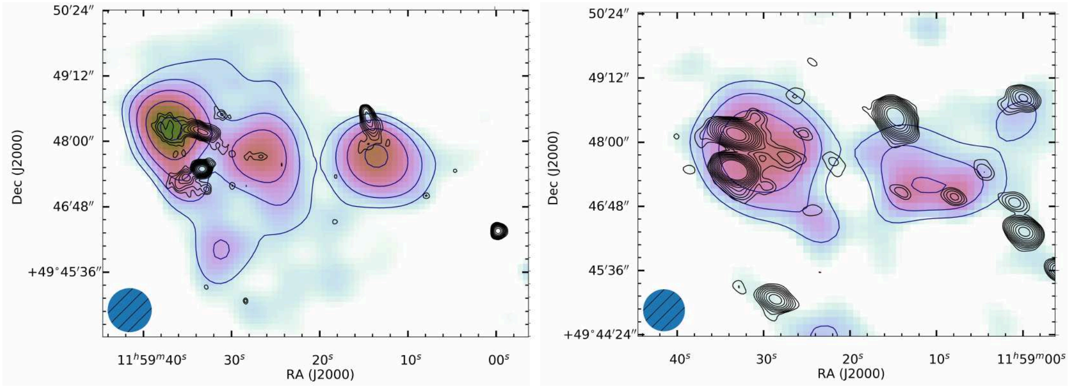

FIGURE 4.3: LOFAR (143 MHz) total intensity image (left) and VLA (1.5 GHz) total intensity image (right) at $45'' \times 45''$ traced with blue contours. Black contours trace the emission from the discrete sources at $8'' \times 8''$ (LOFAR) and $19'' \times 18''$ (VLA). Blue contours start at $4 \times \sigma_{\rm rms}$ with increaments of $\sqrt{2}$ where the rms is 450 µJy beam^{-1} (LOFAR) and 35 µJy beam^{-1} (VLA). Black contours start at $3 \times \sigma_{\rm rms}$ with increaments of $\sqrt{2}$ where the rms is 230 µJy beam^{-1} (LOFAR) and 35 µJy beam^{-1} (VLA).

4.3.2 Discrete Sources in the Field

The LOFAR high resolution images show that there exists at least 5 discrete sources in the cluster region. These sources are labelled as S1, S2a, S2b, S2c, and S3 in fig. 4.1. A search for all sources with redshift information confirms all but source S2c to be cluster members. Sources S2a, S2b, and S2c are blended into a single source S2 when the resolution gets larger than around 10 arc seconds. The properties of the discrete sources are recorded in table 4.5. We find that at 1.5 GHz, sources S2a, S2b, and S2c can not be resolved into discrete sources (see fig. 4.3 left) with the current data. The contribution of the total flux density by the compact emission in the field amounts to 204.2 ± 2.0 mJy and 38.2 ± 0.4 mJy at 143 MHz and 1.5 GHz, respectively. The integrated spectral indices between 143 MHz and 1.5 GHz of the sources were also computed (see column 6 of table 4.5). The values are in agreement with the average spectral index of radio galaxies, i.e α of about 0.7.

The measurement of the flux density of the halo emission at 1.5 GHz in the low resolution VLA image results in 5.2 ± 0.2 mJy. We acknowledge that it is challenging to subtract the emission from the lobes of the radio radio galaxies in the halo region. However, due to a value of 18 arc seconds achievable for the high resolution images, we argue that all the emission from the lobes of the radio galaxies is modelled, and therefore subtracted properly. To check this value, we also perform a subtraction in the image plane. This is done by summing up the contribution of the total flux density of all discrete sources in the halo region,

Table 4.6: Properties of the radio halo in A1430

Property	Value
$\mathcal{S}_{143\,\mathrm{MHz}}$ [mJy]	78.5 ± 3.4
$\mathcal{S}_{1.5\,\mathrm{GHz}}$ [mJy]	5.1 ± 0.2
$P_{1.4\,\mathrm{GHz}}$ [WHz^{-1}]	$1.92 \pm 0.45 \times 10^{24}$
$\alpha_{143\,\mathrm{MHz}}^{1.5\,\mathrm{GHz}}$	1.16 ± 0.11
Linear size [Mpc]	2.1 ± 0.1

and subtracting this sum from the total flux density where no source subtraction has been done. At 1.5 GHz, this gave a value of 5.1 ± 0.2 mJy as the remainder, in agreement with the initial value. The values are recorded in table 4.6 together with the linear size of the radio halo. When discrete sources reside in a region with diffuse extended emission, a proper subtraction of these discrete sources is required in order to obtain reliable flux density estimates for the extended diffuse emission. For the LOFAR imaging, we performed a careful subtraction of the discrete sources which involved imaging at varying resolutions in order to recover the faint lobes of the radio galaxies. We did this by: (1) Imaging at 10 arc seconds, and subtracting the model obtained. (2) Imaging at 18 arc seconds to recover the emission residing in the lobes that could not be recovered properly at 10 arc seconds, and adding the model obtained to the initial model obtained at 10 arc seconds. (3) Re-imaging at 18 arc seconds the *uv* subtracted data in order to check that all the emission from the radio galaxies has been subtracted. A *uv* cut of 1000λ was applied in all imaging steps in order to preserve the halo emission that could have been subtracted. With this procedure, it is only the faintest parts of the lobes of S1 that we could not model and subtract (see the eastern-most part of A1430E in the LOFAR image). The data quality at hand could not allow for a better imaging procedure. With the careful discrete source subtraction, we argue that the emission that is left in the image belongs to the radio halo. A deeper study of all discrete sources in the field is planned when deeper observations of the field at higher frequencies are performed.

4.3.3 The Two-Component Giant Radio Halo

Figure 4.5 shows blue contours that trace the extent of the radio halo at 143 MHz with the contribution from the discrete sources subtracted carefully. The total extent of the extended emission is about 2 Mpc in size. The western part of the extended emission traces the major component of the X-ray emission, and is

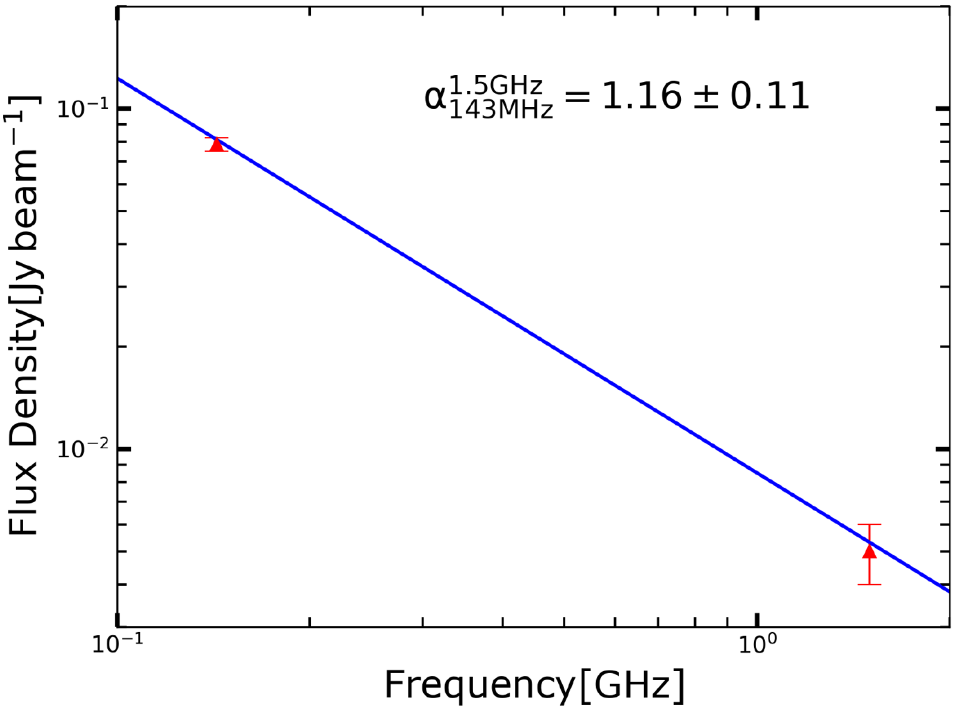

Figure 4.4: Integrated spectrum of the radio halo between 143 MHz and 1.5 GHz. The fitted line depicts a spectral index α of 1.16 for $\mathcal{S} \propto \nu^{-\alpha}$.

about 1 Mpc in size. The eastern part of the extended emission includes an area that could be due to insufficient subtraction of the lobes of the radio galaxy S1. Nevertheless, the western part of A1430E is reliable. This part lies in a region where the ICM is less dense, a region where one can see a bridge connecting the two X-ray components . We therefore consider this to be a two-component radio halo system, A1430E and A1430W. The total flux density obtained at 143 MHz is 78.5 ± 3.4 mJy. A sanity check was performed in order to examine how well discrete sources were subtracted. The peaks of the compact source emission are not coincident with any peak in the extended emission surface brightness. This suggests that the derived extended emission is not contaminated by the residual emission.

Using the flux density of 5.1 ± 0.2 mJy, obtained at 1.5 GHz for the extended emission, we compute a spectral index of 1.16 ± 0.11 for the radio halo. The properties of the radio halo are recorded in table 4.6.

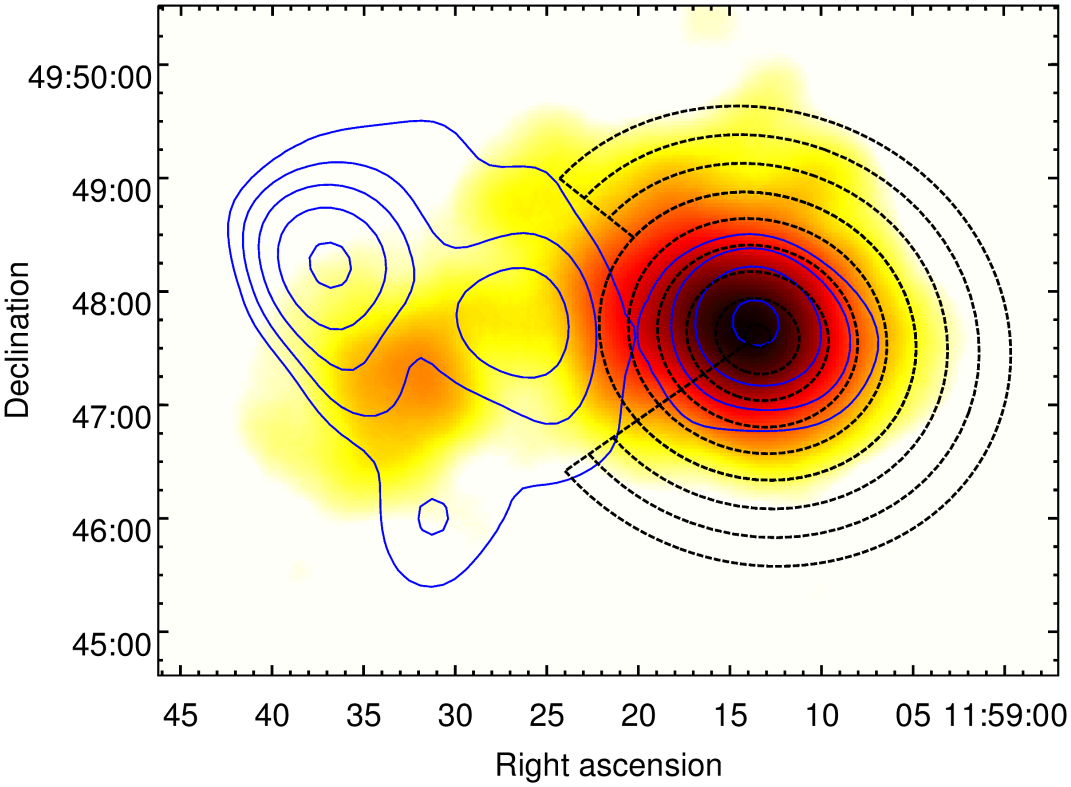

FIGURE 4.5: LOFAR HBA low resolution image ($45'' \times 41''$) contours overlaid onto the Chandra Xray image (colour). The r.m.s noise level reached for the LOFAR HBA image is 450 µJybeam^{-1}. The minimum contour level is $4.0 \times \sigma_{\rm rms}$ followed my multiples of $\sqrt{2}$. The discrete sources shown in the left panel of fig. 4.3 were subtracted.

4.3.4 Integrated Radio Spectrum between 143 MHz and 1.5 GHz

The average spectral index for radio halos is assumed to be 1.3 when a complimentary flux density measurement is not available (Feretti et al., 2012; Brunetti and Jones, 2014). For Abell 1430, we obtained complimentary data from the VLA data archive. The VLA L-band data enabled us to estimate the flux density at 1.5 GHz. With two measurements at different frequencies, a spectral index of 1.16 ± 0.11 was obtained. Figure 4.4 shows the two measured points used in obtaining the integrated spectral index. The spectral index is close to the average spectral index of radio halos. For this spectral index, considering a redshift of 0.35, the radio halo power at 1.4 GHz is $1.92 \pm 0.21 \times 10^{24}$W Hz^{-1}. The flux density is close to the detection limit of NVSS, explaining the non detection in the survey. We argue that radio halos whose power at 1.4 GHz is close to the NVSS detection limit could have been missed and can only be discovered in low frequency surveys, e.g LoTTS.

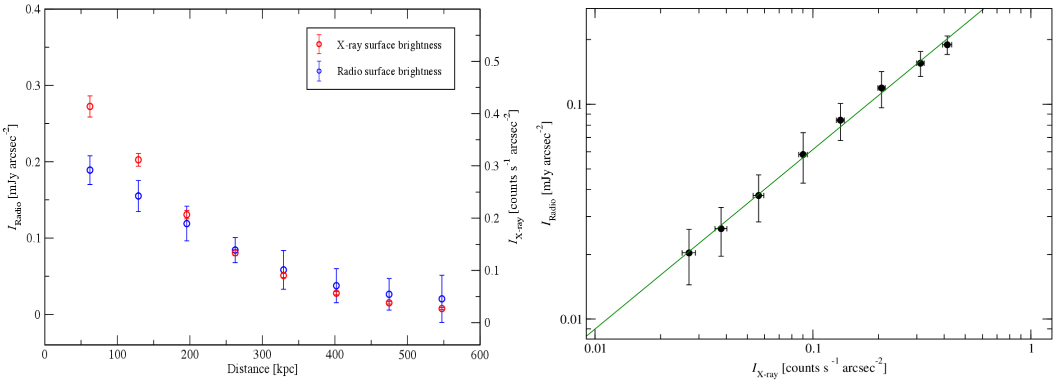

FIGURE 4.6: Comparison between radio and X-ray normalised surface brightness profiles in A1430W. X-ray surface brightness vs Radio surface brightness in concentric annuli centered at the subcluster center. The slope = 0.84 ± 0.03.

4.3.5 X-ray vs Radio

To compare the surface brightnesses of both the X-ray and radio emission, we separate the radio halo into A1430E, and A1430W. We then analyse the western component since its radio emission traces the X-ray morphology of the main cluster component. The total extent over which the two overlap each other is about $3.3'$, corresponding to a physical extent of about 1 Mpc. The X-ray emission in A1430W is seen to be elongated in the NE-SW direction (see fig. 4.5). The similarity between the radio halo and X-ray morphology has been reported for several galaxy clusters, indicating a connection between thermal gas and relativistic plasma.

We create elliptical annuli that mimic the elongation, see fig. 4.5, excluding the region where A1430E lies. The average surface brightnesses in each annulus in both the radio and X-ray images were measured. The resultant plots are shown in fig. 4.6. The comparison between the radio and X-ray morphologies for A1430W indicates that the radio emission has a connection with the thermal plasma, as found for several other radio halos (see Feretti et al., 2012). The brightness profiles for both are also strikingly similar. The extracted points were then fitted to a power law relation of the type

$$I_{\rm radio} \propto I_{\rm X-ray}^{b}, \tag{4.1}$$

where the radio surface brightness $I_{\rm radio}$ is expressed in mJy arcsec^{-2} and X-ray surface brightness $I_{\rm X-ray}$ in milli counts s^{-1} arcsec^{-2}. The fitted power relation results in a slope of 0.84 ± 0.03. The value of the slope is of special significance for hadronic models, where the radio surface brightness scales with the square of the cluster density, i.e the X-ray surface brightness. A slope close to 1 could suggest that the radio halo is of hadronic origin. We therefore argue that the radio halo is unlikely of hadronic origin.

4.3.6 Origin of the Two-Component Radio Halo

We propose that the peculiar extended diffuse radio emission in A1430 is bicomponental, i.e A1430E and A1430W. A1430W is tracing the main X-ray cluster component, and A1430E is residing in a bridge region that connects the two X-ray cluster components, a region of low ICM density. A1430W shows characteristics of a merger in its late stages where the BCGs are usually deep in the potential well of the cluster. The elongation of the X-ray surface brightness is also indicative of a major merger. The merger in this component of the cluster could have triggered enough turbulence for the thermal electrons to be accelerated to relativistic energies.

While the halo emission in A1430W traces the ICM extension, that in A1430E is quite peculiar in nature since the halo emission resides in a region with less dense ICM. It is challenging to explain the origin of diffuse extended radio emission in such low density environments. The bridge visible in X-ray could indicate an ongoing merger between the two sub cluster components. Using galaxy information to trace the dark matter, it is noted that the dark matter component precedes the hot gas. This could indicate a rapid infall of A1430E into the main A1430W component. At high velocities, the dark matter component compresses the ICM plasma. In a region where seed electrons from radio galaxies could exist, such compression triggers the acceleration of mildly relativistic electrons to relativistic energies. We argue that A1430E could be a result of adiabatic compression of the thermal plasma.

4.3.7 Scaling Relations

Correlations between the thermal and non-thermal components of galaxy clusters have been used to study cluster properties. These scaling relations have shown that the extended non-thermal emission in galaxy clusters is tightly correlated with the X-ray emission.

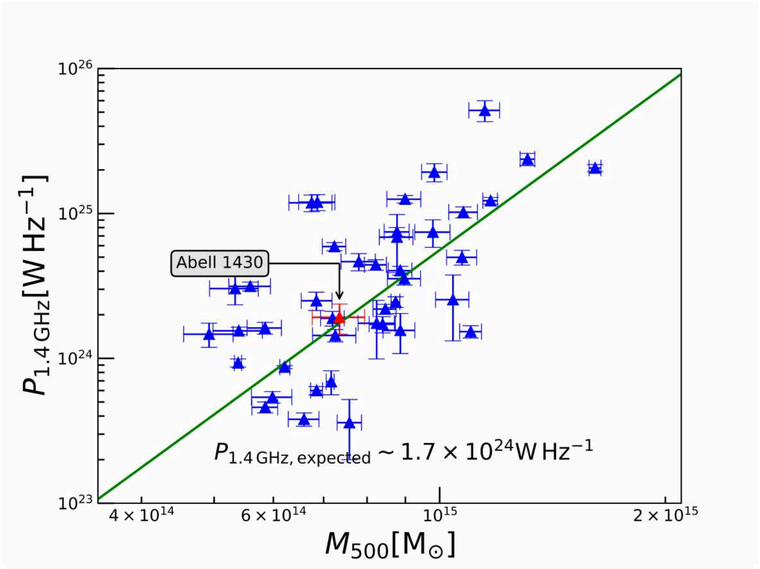

FIGURE 4.7: Radio power at 1.4 GHz vs M_{500}

We calcule the radio power at 1.4 GHz assuming a redshift and spectral index of 0.35 and 1.16, respectively. This results in $P_{1.4\,\mathrm{GHz}} = 1.92 \pm 0.21 \times 10^{24}\mathrm{W\,Hz^{-1}}$. Using results obtained from all radio halos by Cassano et al. (2013), we overplotted values obtained for A1430.

Figure 4.7 shows the $P_{1.4\,\mathrm{GHz}} - M_{500}$ correlation. The radio halo in A1430 is indicated by the red point. Using Cassano et al. (2013) values of the BCES bisector for radio halos only, we overplot the correlation obtained. This correlation estimated a value of $P_{1.4\,\mathrm{GHz}} = 1.70 \pm 0.13 \times 10^{24}\mathrm{W\,Hz^{-1}}$ for A1430. This is in agreement with the value we provide.

In fig. 4.8, we overplot values of A1430 for the $P_{1.4\,\mathrm{GHz}} - L_{\mathrm{X},500}$ onto those obtained for radio halos in Cassano et al. (2013) in which the correlation would yield a value of $P_{1.4\,\mathrm{GHz}} = 2.20 \pm 0.15 \times 10^{24}\mathrm{W\,Hz^{-1}}$. The value we obtain is in agreement with their correlation.

We overplotted values of A1430 for the $P_{1.4\,\mathrm{GHz}} - Y_{500}$ onto those obtained for radio halos in Cassano et al. (2013) in which the correlation would yield a value of $P_{1.4\,\mathrm{GHz}} = 4.10 \pm 0.61 \times 10^{24}\mathrm{W\,Hz^{-1}}$. This is shown in the right panel of fig. 4.8. The value we obtain is below this correlation but fits in the overall scatter for the other sources.

Our measurements are in good agreement with the scaling relations; suggesting that the extended emission is indeed a radio halo.

4.4 Discussion

Radio surveys at low frequencies like the LOFAR Two-meter Sky Survey (LoTSS) in this case, have the potential to discover several previously undetected diffuse radio emission sources in galaxy clusters (Shimwell et al., 2017). This could be attributed to the rising discovery of steep spectrum sources that are easily detectable at low frequencies. With quicker calibration strategies under development, and the release of sky images at low frequencies, the number of known diffuse radio sources is expected to increase. This will enrich our statistical studies and improve our understanding of the nature of such sources.

Here, we report the discovery of one of such new discoveries that are under way using first insights from a LoTSS survey pointing in the Hobby-Eberly Telescope Dark Energy Experiment (HETDEX) Spring Field (Hill et al., 2008). Archival VLA wideband L-band data was used to study the emission at higher frequencies. This made it possible to study the spectral nature of the source. We classify it as a two-component radio halo.

The radio halo is $\sim$ 2.1 Mpc in size. The western $\sim$ 1.0 Mpc sized part of the halo traces the X-ray emission while the eastern part extends beyond the X-ray emission margins. This suggests that A1430E could be a result of plasma compression. The spectral index of the radio halo between 143 MHz and 1.5 GHz is $\alpha = 1.16 \pm 0.11$, which is close to the average spectral index of all known radio halos, namely $\alpha \sim 1.3$. Due to the insufficient sensitivity of the observations at 1.5 GHz, the obtained flux density is a lower limit. This is because their observations were snapshots. The low limit of the flux density means that the spectral index could be slightly lower, possibly closer to $\alpha \sim 1.0$. It is therefore essential that deeper observations with the VLA L-band are carried out in order to perform more accurate flux density measurements.

The galaxy cluster A1430 has been reported earlier to be at a redshift of 0.21. This redshift was obtained by averaging the photometric redshift of only two galaxies in the field. The SDSS survey has provided more redshift information on the galaxies in the cluster field. We find that all but the previous two galaxies are located at a redshift of 0.35, suggesting that A1430 is located at this redshift.

Properties of A1430 were obtained from both Popesso et al. (2004) and Planck Collaboration et al. (2014a) and are recorded in table 4.1. Using a redshift of 0.35 and the recovered flux density at 1.5 GHz of $\sim$ 5 mJy, we computed a power of $P_{1.4\,\mathrm{GHz}} = 1.92 \pm 0.21 \times 10^{24}\mathrm{W\,Hz^{-1}}$. This value is in agreement with the $P_{1.4\,\mathrm{GHz}}$–M_{500}, $P_{1.4\,\mathrm{GHz}}$–$L_{\mathrm{X},500}$, and $P_{1.4\,\mathrm{GHz}}$–Y_{500} correlations for cluster radio halos. This suggests that the emission is attributed to the large scale disturbances in the ICM. With this addition to the statistics, we show that low frequency surveys will play an important role in enriching the sample of radio halos in literature.

4.5 Summary

We present a study on the merging galaxy cluster A1430 using LOFAR HBA data and archival VLA L-band data. The two data sets were used to study the morphology and spectral energy distribution of the extended radio emission. We analyse CHANDRA X-ray data to study the relationship between the radio emission and the X-ray emission. We conclude that: (1) A1430 hosts an extended (2.1 Mpc in size) radio halo that has not been detected in previous radio sky surveys (e.g., Condon et al., 1998). The morphology is described with two components, A1430E and A1430W. (2) The radio emission in A1430W traces the X-ray surface brightness morphology while that in A1430E extends beyond the X-ray morphology into a region of lower density. We measure an integrated flux of 78.5 ± 3.4 mJy and 5.1 ± 0.2 mJy at 143 MHz and 1.5 GHz, respectively. (3) From our analysis of the spectral energy distribution, the radio halo spectral index is uniform across the cluster, with an average value of $\alpha \sim 1.2$. This is in agreement with the average spectral index of radio halos. (4) A reliable redshift is needed when estimating the global cluster temperature and the X-ray luminosity. We study the redshifts of the galaxies in the cluster using the SDSS Data Release 14 in order to obtain a reliable redshift. We use the X-ray luminosity to compute the radio power at 1.4 GHz for a comparison with the radio halo power of other clusters. (5) The extended emission is attributed to the large scale disturbances in the ICM. We computed a radio power of $P_{1.4\,\mathrm{GHz}} = 1.92 \pm 0.21 \times 10^{24}\,\mathrm{W\,Hz^{-1}}$. This value is in agreement with the $P_{1.4\,\mathrm{GHz}}$–M_{500}, $P_{1.4\,\mathrm{GHz}}$–$L_{\mathrm{X},500}$, and $P_{1.4\,\mathrm{GHz}}$–Y_{500} correlations for cluster radio halos.

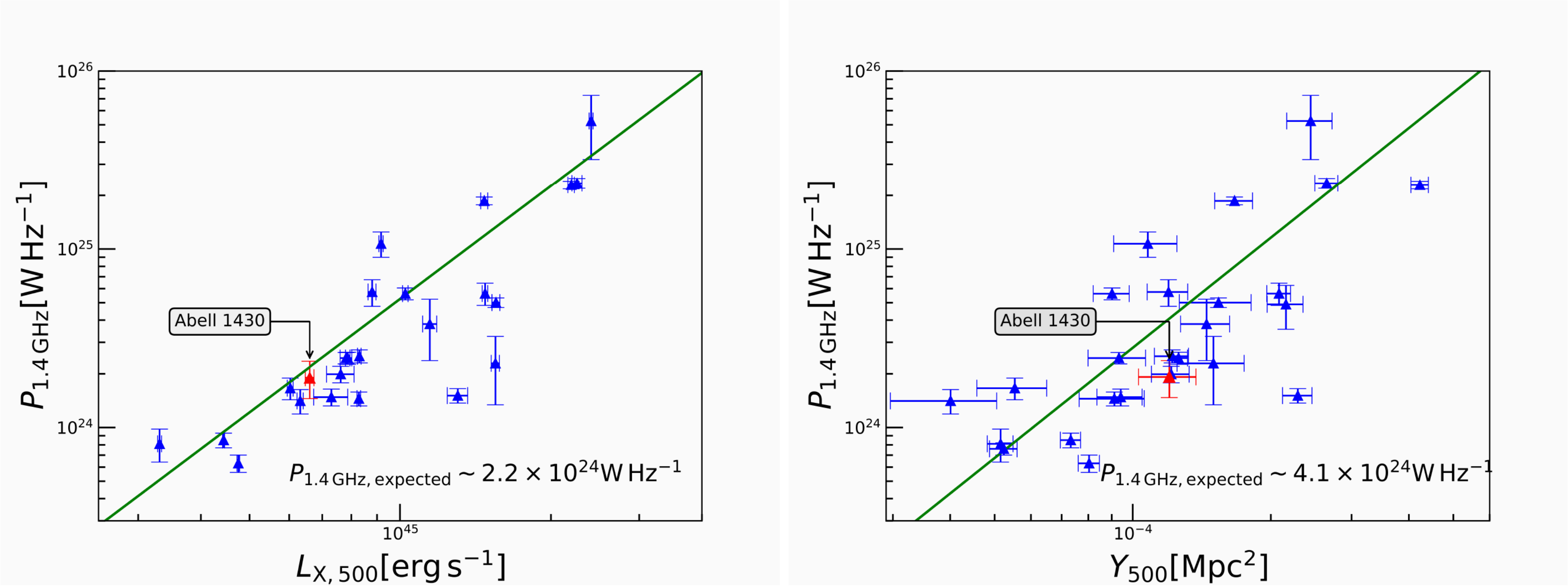

FIGURE 4.8: Radio power at 1.4 GHz vs $L_{X,500}$(right) and Radio power at 1.4 GHz vs Y_{500}(left) for all the known radio halos. Radio halos are known to follow the correlations described by the green line (Cassano et al., 2013). The quantities for A1430 are in agreement with those of the known radio halos.

Chapter 5

Observations of Cluster Radio Relics at Higher Frequencies

Detailed studies of radio relics in galaxy clusters have suggested that the relics could be a consequence of cluster wide shocks. Cluster shocks are generated during cluster mergers (see e.g., Feretti et al., 2012; Brunetti and Jones, 2014, for a review). This is emphasised by many discoveries of systems with double radio relics. When the merger is between cluster components of uneven mass, the radio relics morphologies can be complex. Careful and deeper radio studies are therefore required to understand the nature of the relics, and a possible interpretation of their formation. To do this, polarisation studies are useful since the polarised structure, when detectable, can be studied in detail. The internal structure of either the radio emitting region and/or the foreground cluster medium can also be investigated through Faraday RM studies. Previous studies have however been carried out at lower frequencies where polarisation studies are still challenging. Polarisation & Faraday RM studies are vital for a careful dissection of all the components along the line of sight. It is expected that shocks will compress the plasma and thus align the previously misaligned magnetic field in the region. Wide band spectral index studies are also vital for Mach number estimates. We therefore study 4 galaxy clusters, previously studies at low frequencies only. We observe these clusters with the 100-m *Effelsberg* single dish radio telescope at 4.85 GHz and 8.3 GHz. The relics in these galaxy clusters are either already confirmed to be polarised or have shown some hints of being polarised sources. The degree of polarisation we obtain provides an estimate of the both the Mach number, $\mathcal{M}$, of the shock that generated the relic and the magnetic field strength, B, in the

TABLE 5.1: Properties of the 4 galaxy clusters in the sample

Property	PSZ1-G108	A746	0809+39	A1367
RA	$23^{\mathrm{h}}22^{\mathrm{m}}50.0^{\mathrm{s}}$	$09^{\mathrm{h}}09^{\mathrm{m}}37.3^{\mathrm{s}}$	$08^{\mathrm{h}}08^{\mathrm{m}}45.0^{\mathrm{s}}$	$11^{\mathrm{h}}44^{\mathrm{m}}44.6^{\mathrm{s}}$
DEC	$48°48'00''$	$51°32'48''$	$39°00'00''$	$19°41'59''$
z	0.34	0.23	0.20	0.03
$L_{\mathrm{X},0.1-2.4\,\mathrm{keV}}$ [ergs^{-1}]	7.5×10^{44}	3.7×10^{44}	$\leq 1.0 \times 10^{43}$	1.5×10^{44}
M_{500} [$\times 10^{14}\mathrm{M}_{\odot}$]	$7.70^{+0.73}_{-0.88}$	$5.34^{+0.39}_{-0.40}$	-	-

cluster medium. The sources in our study and their properties are listed in table 5.1.

5.1 Previous Studies

The galaxy cluster PSZ1 G108.18-11.53 hereafter PSZ1-G108-11 is listed in the Planck catalogue of galaxy clusters. The cluster lies at a redshift of about 0.34 as measured spectroscopically by Planck Planck Collaboration et al. (2014b). The Planck satellite identifies galaxy clusters by measuring the effect of the clusters Sunyaev Ze'ldovich (SZ) signal on the cosmic microwave background radiation. By integrating the SZ signal over the clusters angular extent, the total thermal energy is obtained. Using the relationship of total thermal energy with cluster mass, a value of $7.7^{+0.7}_{-0.9} \times 10^{14}\mathrm{M}_{\odot}$ for the mass enclosed within R_{500} (Planck Collaboration et al., 2015). Using *ROSAT* observations, the ICM is estimated to have a total luminosity of 7.5×10^{44}ergs^{-1} and a cluster electron energy of about 6.5keV (de Gasperin et al., 2015).

Abell 746, hereafter A 746 is a Bautz-Morgan (BM) III type merging galaxy cluster located at a redshift of 0.23 (Koester et al., 2007). It is also identified as ZwCl 0905.9+5143 in the Zwicky catalogue of galaxy clusters and as MaxBCG J137.41809 + 51.54460 in the MaxBCG sample of galaxy clusters in which its redshift was calculated. van Weeren et al., 2011 discovered a faint radio halo and radio relic using the VLA and WSRT radio telescopes. The radio relic in this cluster has a largest angular extent of 5′ which corresponds to a physical size of 1.1 Mpc at the measured redshift. The hot intra-cluster gas (ICM) was detected using *ROSAT* and estimated to have a total luminosity of 3.68×10^{44}ergs^{-1}. A point source is attached to the southernmost part of the relic. This could have been thought to be the origin of the elongated relic but thanks to deep polarisation studies, the relic is highly polarised and is not associated to the source. We study this source using the *Effelsberg* radio telescope at 4.85 & 8.3 GHz to obtain a wide frequency estimate of the spectral index and polarisation degree.

The extended diffuse radio emission in 0809+39 was discovered through a blind search for diffuse radio emission in the WENSS survey (Rudnick et al., 2006). It is quite peculiar because it lies in a low density environment (poor cluster) (Delain and Rudnick, 2006). In such a low density environment, the radio luminosity far exceeds that expected for on a standard radio/X-ray correlation for extended diffuse synchrotron sources (see e.g., Cassano et al., 2010). The source was followed up by Brown and Rudnick (2009) where they studied its spectral, polarisation, and environmental properties using the WSRT and VLA for radio wavelengths. Two distinct sources lie in the field, with a polarized one to the north and an unpolarised one to the south. A study on the environment in which the two sources lie suggests that the one to the south is perfectly aligned with a filament of galaxies at a redshift of ~ 0.04. The northern polarized source, tentatively classified as a relic, is associated with a poor galaxy cluster at $z \sim 0.2$. We observe this the field in order to confirm the nature of the sources.

Abell 1367 ($z = 0.022$), hereafter A 1367, is part of a filamentary supercluster structure in the Coma galaxy cluster. It is a merging galaxy cluster that hosts a radio relic that lies in the northwest (Cortese et al., 2004). Indeed, Ghizzardi et al. (2010) detected an X-ray brightness discontinuity—which they label a "merging" cold front—about $350''$ south of the X-ray center (about $70''$ from the peak) using *XMM-Newton*. The diffuse radio emission in the cluster has been observed before, but first labelled a radio halo (see e.g., Gavazzi and Trinchieri, 1983; Gavazzi and Jaffe, 1987), and later as a radio relic; with the detection of polarised emission (Ensslin and Biermann, 1998; Farnsworth et al., 2013). We observe the field at 4.85 GHz in order to study the relic properties such as the Mach number.

The properties of all 4 fields are summarised in table 5.1. We performed the data reduction and imaging on all 4 fields as described in Müller et al. (2017) or as in section 2.4.2. Detailed analyses are still ongoing for the observations that were carried out at 8.3 GHz. We present here our current findings for the observations carried out at 4.85 GHz.

Table 5.2: Available radio relic properties

Relic	S_ν (mJy)						$\alpha^{1380\,\text{MHz}}_{147/351\,\text{MHz}}$	$\alpha^{4850\,\text{MHz}}_{1380\,\text{MHz}}$
	4850 MHz	1380 MHz	607 MHz	351 MHz	323 MHz	147 MHz		
PSZ1 N	12.1 ± 0.2	67.7 ± 0.3	177 ± 2	–	422 ± 2	1032 ± 14	1.25 ±0.02	1.37 ±0.05
PSZ1 S	8.9 ± 0.2	45.4 ± 0.3	128 ± 2	–	323 ± 3	753 ± 15	1.28 ±0.02	1.30 ±0.05
A746	–	24.5 ± 2.0	–	–	–	–	–	–
0809 N	9.1 ± 0.2	37.8 ± 0.7	–	178 ± 0.7	–	–	~1.12	–
0809 S	5.0 ± 0.2	24.8 ± 1.0	–	136 ± 1.1	–	–	~1.23	–
A1367	–	~ 232	–	–	–	–	–	–

Please note: S_ν values for PSZ1 except those at 4.85 GHz are quoted from de Gasperin et al. (2015); those of 0809, except at 4.85 GHz, are quoted from Brown and Rudnick (2009).

5.2 Results and Discussion

PLANCK PSZ1-G108-11

The total intensity & polarisation maps at 4.85 GHz are shown in the left panel of fig. 5.1, with the B-vectors overlaid to show the magnetic field alignment. The emission from both relics is clearly visible. Due to the large beam of the *Effelsberg* single dish telescope, it is not possible to resolve the discrete sources close to the Northern and Southern radio relics. Flux densities of 12.1 ± 0.2 and 8.9 ± 0.2 for the Northern and Southern relics, respectively were measured carefully. Further details can be found in table 5.1. These values yielded respective spectral indices of 1.37 ± 0.05 and 1.30 ± 0.05. The emission in the cluster is connected by a *bridge* that could be indicative of the central halo emission previously discovered by de Gasperin et al. (2015). The two large scale diffuse sources are clear radio relics. Mach number estimates will be computed after the inclusion of observations performed at 8.3 GHz.

Abell 746

A746 is a clear relic at 1.4 GHz. At this frequency, the degree of polarization is high, up to 50%. We show in the right panel of fig. 5.1 that the diffuse emission can be detected at 4.85 GHz, and that polarised emission exists. However, more maps are needed in order to measure the flux density in total power and the polarised flux density reliably. We nevertheless argue that the emission should be associated with a shock due to the detected polarised emission. Further details are shown in table 5.2.

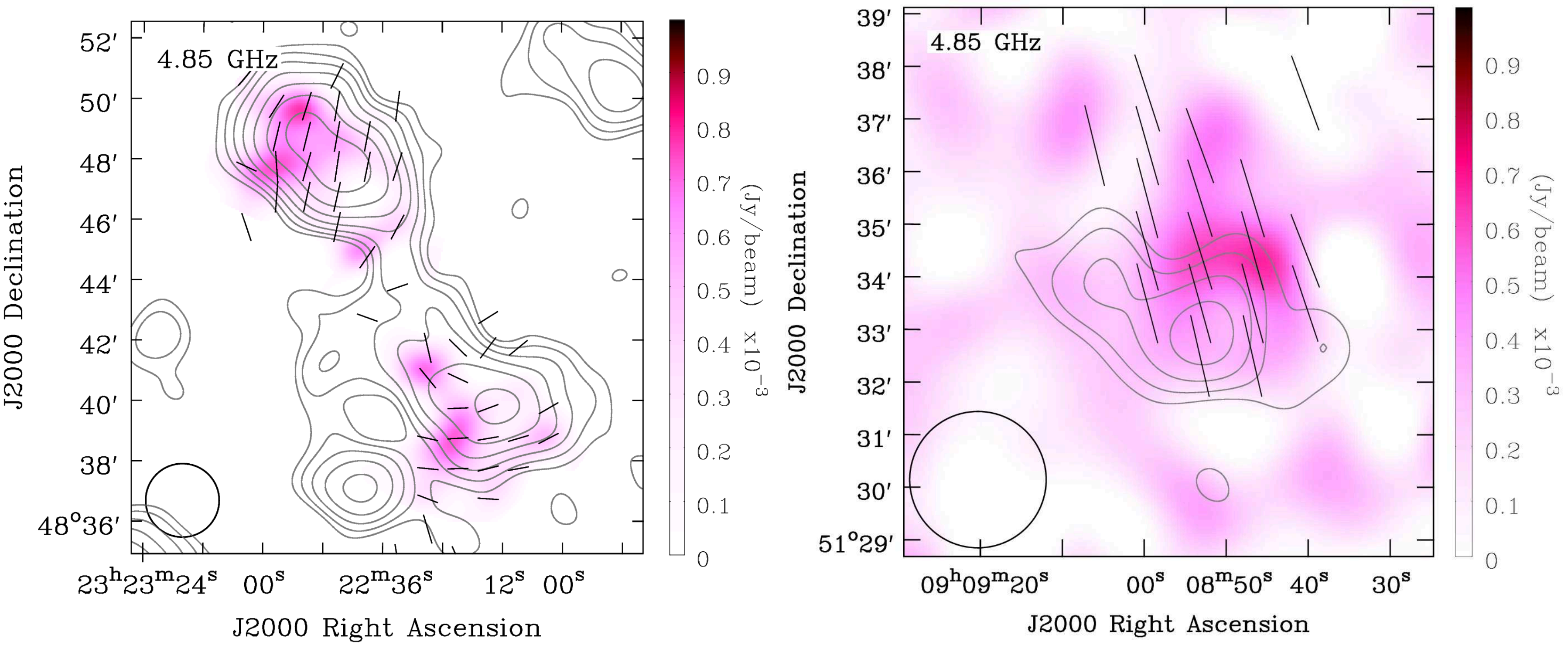

FIGURE 5.1: *Left:*PSZ1-G108 *Effelsberg* (4.85 GHz) Polarised intensity image at $152'' \times 150''$ resolution in color. Total Intensity contours overlaid; start at $5\sigma_{\mathrm{rms}}$ with increments of $\sqrt{2}$ where the rms is $2\,\mathrm{mJy\,beam^{-1}}$. *Right:*A746 *Effelsberg* (4.85 GHz) Polarised intensity image at $150'' \times 150''$ resolution in color. Total Intensity contours overlaid; start at $1\sigma_{\mathrm{rms}}$ with increments of $\sqrt{2}$ where the rms is $0.7\,\mathrm{mJy\,beam^{-1}}$. For both images, $B-$field vectors are overlaid to show the alignment of the magnetic field. The $B-$field vectors are not corrected for Faraday rotation.

0809+39

The two diffuse sources are shown in the left panel of fig. 5.2, with the polarised emission in colour, and total power contours over-plotted. The B-vectors clearly show that its only the northern source that is polarised. Although a polarised point source lies in the same region, we are able to distinguish the polarised emission of the point source from that of the relic. We obtain flux density values of 9.1 ± 0.2 and 5.0 ± 0.2 mJy for the northern and southern sources, respectively. The spectral indices that result from our measurements are about 1.1 and 1.2 for the northern and southern sources, respectively. We argue that the emission is associated with a shock. Further polarisation studies will shed more light on the strength of the shock.

Abell 1367

The right panel of fig. 5.2 shows the total power contours overlaid on the polarised emission on the field. B-vectors show the alignment of the magnetic field structure. The existence of a compact source close to the diffuse emission made the analysis difficult. We however performed a careful RFI excision procedure that enabled us obtain a reliable map. The diffuse structure can be seen to the east of the compact source. More maps are needed in order to perform a reliable polarisation analysis.

5.3 Summary & Conclusions

Radio continuum observations with single-dish telescopes like the *Effelsberg* 100-m telescope are ideal for confirming radio relics. This is done by detecting the polarised emission from which the polarisation degree can be calculated. The detection of the polarised emission is possible because galaxy cluster radio relics are among the sources on the sky that are highly polarised. We detected the polarised flux in all four sources observed and argue that these sources are cluster radio relics. Further analyses on the sources are still ongoing in order to estimate the polarisation degree, and calculate the Mach number for each relic. The radio spectra below 4.85 GHz can be well fitted by a single power law for all relics whose flux density was measured. The study, when complete, including the observations at 8.3 GHz, will allow us to analyse the radio spectra beyond

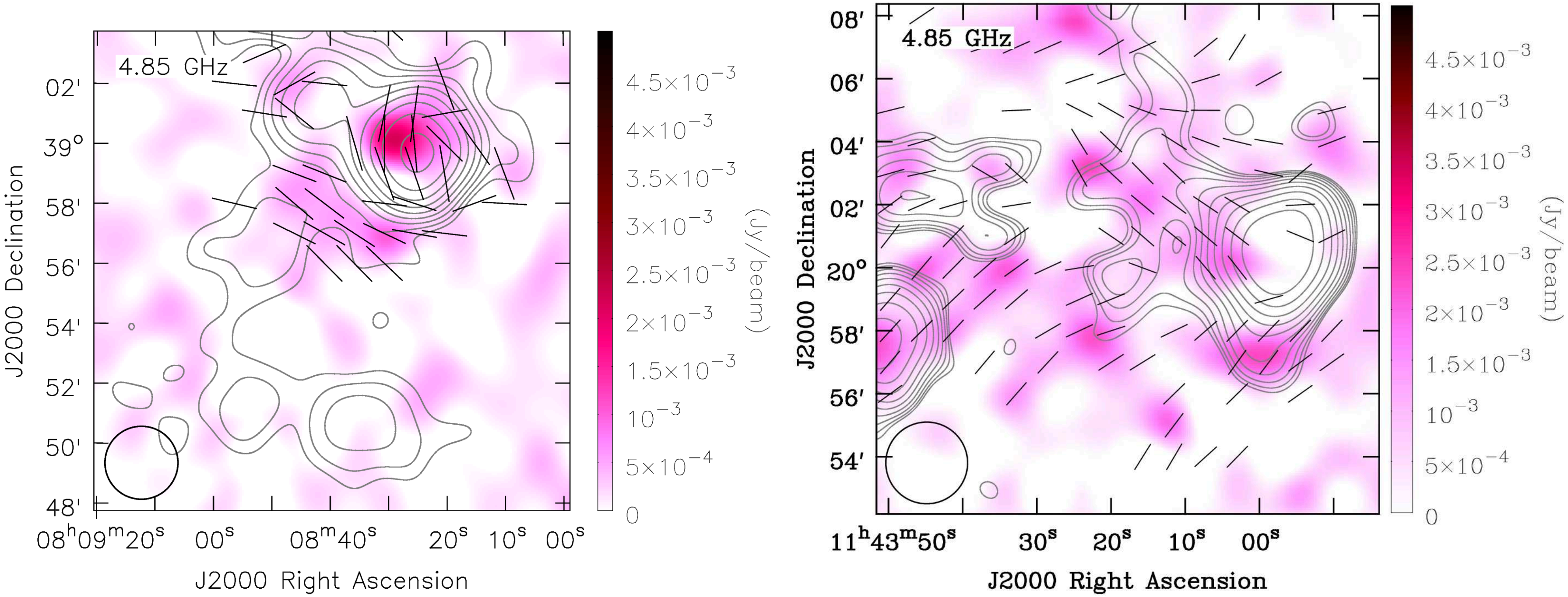

FIGURE 5.2: *Left:Effelsberg* (4.85 GHz) Polarised intensity image at $146'' \times 146''$ resolution in color. Total Intensity contours overlaid; start at $5\sigma_{\rm rms}$ with increments of $\sqrt{2}$ where the rms is 5 mJy beam^{-1}. *Right:*A1367 *Effelsberg* (4.85 GHz) Polarized intensity image at $153'' \times 153''$ resolution in color. Total Intensity contours overlaid; start at $1\sigma_{\rm rms}$ with increments of $\sqrt{2}$ where the rms is 1.0 mJy beam^{-1}. For both images, $B-$field vectors are overlaid to show the alignment of the magnetic field. The $B-$field vectors are not corrected for Faraday rotation.

4.85 GHz. Spectral breaks at higher frequencies are found in some relics (Stroe et al., 2016); this needs to be confirmed for the radio relics in our study.

Combining all earlier polarization observations with the current observations, and performing an RM Synthesis (Brentjens and de Bruyn, 2005) will allow us to measure the Faraday spectrum. A Faraday spectrum provides information about the internal structure of either the radio emitting region and/or the foreground cluster medium.

Chapter 6

Conclusions & Outlook

Merging galaxy clusters are a cosmic laboratory in which we study the physics of the most energetic events in the universe. The ICM being magneto-ionic in nature is useful in understanding particle acceleration mechanisms and in turn the strength of the magnetic field in galaxy clusters. An understanding of these properties is vital in order to discover many large scale synchrotron sources in galaxy clusters.

To date, about 30% of merging galaxy clusters have been found to host extended synchrotron sources known as *radio relics* and *radio halos*. The discovery of such sources was made possible by radio sky surveys like the NVSS and TGSS. However, past surveys were carried out at higher frequencies, where, due to the steep spectrum of such sources, only a few are detectable. Current on-going surveys like the LoTSS are expected to increase the number of known extended synchrotron sources since they are carried out at low frequencies. The discovery of the radio halo in A1430, which was not visible in NVSS, shows how vital such low frequency surveys are.

We confirm the nature and morphology of the radio relic in A115 using four different frequency observations. For the spectral index, we measure a value of $\alpha = 1.1 \pm 0.1$, which suggests that the relic has just been brightened within the last about 500 Myrs. This also is in agreement with a pre-merger scenario suggested by Barrena et al. (2007), Dumba et al. (2015) and Hallman et al. (2018).

The alignment of the radio relic makes it possible to investigate how such a relic can form in a low density environment. Polarisation studies show that part of the relic lies deep in the ICM, thus being depolarised by the ICM. The other part of the relic, one that lies in a low density environment shows a uniform alignment of the magnet field across the whole relic region. This suggests that the relic is caused by a large scale shock during an off-axis merger.

We plan to study the properties of the radio relic with deep VLA L-band observations. This will help us perform precise polarisation studies on all the regions of the relic. These observations are already planned for November 2018. Calibration techniques that maximise the achievable dynamic range have been tested, with the purpose of reanalysing the LOFAR-HBA observations. A combination of both results will provide an unprecedented view of the radio relic in A115.

We have presented LOFAR HBA observations of the galaxy cluster A1430, showing for the first time a radio halo that resides in this galaxy cluster. The radio halo morphology suggests a two component system in which one system, A1430W, is due to a previous merger of the main sub-cluster component, and A1430E could be due to the merger between both subcluster components. We argue that in A1430, we are witnessing a rare event where two independent processes are accelerating particles to relativistic energies. We also show, for the first time, the X-ray surface brightness distribution of the galaxy cluster A1430.

The integrated spectral index for the radio halo is consistent with the average spectral index found for radio halos, i.e., $\alpha \sim 1.3$ (see e.g., Cassano et al., 2011; Feretti et al., 2012; Cassano et al., 2013). The spectral index map shows indications of a moderately uniform spectral index across the entire halo region. Deep observations at 1.5 GHz are needed to determine the variation in a better way.

Single dish observations with the *Effelsberg* radio telescope are vital for studying the properties of radio relics at higher frequencies. Spectral breaks at higher frequencies are found in some relics (Stroe et al., 2016); this should be checked for more relics. With a spectral analysis over a wider frequency band, RM Synthesis can be performed in order to measure the Faraday spectrum. A Faraday spectrum provides information about the internal structure of either the radio emitting region and/or the foreground cluster medium. The complete study of the galaxy clusters PSZ1-G108, A746, 0809+39, and A1367 at higher frequencies will shed more light on the properties of the radio relics and the environment in which they are.

Appendix A

X-ray Morphological Parameters

(i) Centroid Shift, w

For galaxy clusters with significantly bright X-ray clumps, the centroid of the X-ray surface brightness will shift as the aperture is varied. This shift is calculated using:

$$w = \frac{1}{R_{\text{max}}} \times \sqrt{\frac{\sum_i (x_i - < x >)^2}{N-1}}, \tag{A.1}$$

where N is the total number of apertures considered and x_i is the position of the centroid of the i^{th} aperture calculated within R_{max} and x the position of the X-ray SB peak. The boundary between relaxed and unrelaxed galaxy clusters is taken to be around $w = 0.01$. For different radii chosen, and/or for different samples, the boundary value can change (O'Hara et al., 2006; Cassano et al., 2010; Weißmann et al., 2013).

(ii) Light Concentration, c

This estimator is used to describe systems that have most of their light concentrated either in the core or outside the core. When applied on X-ray images of galaxy clusters, it will distinguish galaxy clusters with cool cores from those without cool cores. A useful definition is found in Cassano et al. (2010) in which the cluster core radius is estimated to be around 100 kpc. This is written as:

$$c_{[\text{kpc}]} = \frac{S(r < 100\,\text{kpc})}{S(r < 500\,\text{kpc})}, \tag{A.2}$$

where S is the X-ray flux density. To select clusters that have cooling cores, a core region of around 40 kpc is normally chosen (e.g., Santos et al., 2008; Semler et al., 2012). The dividing line between relaxed and non-relaxed galaxy clusters is taken to be around $c_{[\mathrm{kpc}]} = 0.2$.

(iii) Power Ratios, P_i/P_0

The power ratio estimator was introduced by Schade et al. (1995) in order to parametarise the amount of substructure in the ICM relating it to the dynamical state of the galaxy cluster. Power ratios are based on a 2D multipole expansion of the cluster's gravitational potential using the surface mass density distribution. The higher the moments, the finer the structure being described. This means that power ratios have to be calculated within a certain aperture radius (e.g. r_{500}).

The 2D multipole expansion of the 2D gravitational potential $\psi(R, \phi)$ can be written as

$$\psi(R,\phi) = -2G[a_0 \ln \frac{1}{R} + \sum_{m=1}^{\infty} \frac{1}{mR^m}(a_m \cos(m\phi) + b_m \sin(m\phi))], \tag{A.3}$$

where a_m and b_m are:

$$a_m(R) = \int_{R' \leq R} \Sigma(\mathbf{x}')(R')^m \cos(m\phi')d^2x', \tag{A.4}$$

and

$$b_m(R) = \int_{R' \leq R} \Sigma(\mathbf{x}')(R')^m \sin(m\phi')d^2x', \tag{A.5}$$

where $\mathbf{x}' = (R', \phi')$ are the coordinates, G the gravitational constant and Σ represents the surface mass density as described in Schade et al. (1995).

The powers are defined by the integral of the magnitude of ψ_m, the m^{th} term in the multipole expansion evaluated in a circular aperture of radius R. Thus,

$$P_m(R) = \frac{1}{2\pi}\int_0^{2\pi} \psi_m(R,\phi)\psi_m(R,\phi)d\phi. \tag{A.6}$$

The powers are then given by

$$P_0 = [a_0 \ln(R)]^2, \tag{A.7}$$

and

$$P_m = \frac{1}{2m^2 R^{2m}} (a_m^2 + b_m^2). \tag{A.8}$$

The projected mass density is estimated using the X-ray surface brightness assuming that the X-ray surface brightness distribution traces the gravitational potential (Schade et al., 1995). To compare a cluster's estimate with other clusters, the moments are normalised by the zeroth-order moment, obtaining a power ratio. Even power ratios, P_2/P_0 and P_4/P_0 are strongly correlated, with the higher power ratio being more sensitive to smaller scales. Thus merging systems will show higher values of P_2/P_0 than relaxed systems. Odd moments trace asymmetries in the distribution and vanish for relaxed systems. This makes P_3/P_0 the smallest moment which can be used to measure the dynamical state of a cluster unambiguously (see e.g., Schade et al., 1995; Jeltema et al., 2005; Weißmann et al., 2013; Kale et al., 2015; Chon et al., 2016).

Asymmetry Parameter, A

The asymmetry observed in the concentration of light gives an imprint of the morphology of spherical object. This was used to study the morphology of galaxies by Schade et al. (1995). They defined the Asymmetry parameter as:

$$A = \frac{\sum(|I - R|)}{\sum(I)} \tag{A.9}$$

where the difference in flux between an image (I) and its rotated counterpart (R), normalized by the original, gave a value of asymmetry. This procedure became so powerful in detecting disturbed systems that it was also employed by X-ray data analysts to categorize galaxy clusters (Okabe et al., 2010). Different asymmetry parameters are defined depending on how the image is rotated. Images are usually rotated by 180 deg, flipped along the $x - axis$ or $y - axis$, with both axes passing through the X-ray mass centroid. Considering different parameters and selecting the one with the highest value reduces underestimations that may arise due to preferences.

Fluctuation Parameter, F

This parameter is used to discover peaks (valleys) of high (low) X-ray flux over the entire image. It is defined by Rasia et al. (2013) as:

$$F = \frac{\sum(|I - B|)}{\sum(I)} \tag{A.10}$$

where a smoothed image, B, is subtracted from the unsmoothed original one, I, and normalizing with the original. For the smoothed image, various Gaussian kernels can be used depending on the size of peaks (valleys) of substructure under investigation. In such a case the fluctuation parameters can be labelled accordingly. A relaxed cluster will posses lower values in F, while a disturbed cluster would have high values.

Hardness Ratio Indicators, H

This is a technique which is used to identify structures that have been recently accreted into the system. Cooler structures have more power in the soft X-ray band while hotter structures have more power in the hard X-ray band. A ratio between images obtained from these two bands will identify systems with the most recent accretion of cooler structures from those that have relaxed already. This was employed by Gitti et al. (2011) in order to identify cold filaments in Hydra A, a galaxy cluster. The hardness ratio can be defined as:

$$H = \frac{\sum(|H - S|)}{\sum(S)} \tag{A.11}$$

where H and S are images in the hard and soft X-ray energy bands, respectively. The soft X-ray band ranges from $[0.3-1.5]$ keV while the hard X-ray band ranges between $[1.5 - 7.5]$ keV.

Appendix B

The Generic Jones Terms & *Effelsberg* 100-m Radio Telescope

The generic Jones terms are:

$$\mathbf{J}_i = \mathsf{G}_i\mathbf{H}_i\mathbf{Y}_i\mathsf{B}_i\mathsf{K}_i\mathsf{T}_i\mathsf{F}_i, \tag{B.1}$$

where

$\mathsf{F}_i(\vec{\rho}, \vec{r_i})$	is the ionospheric Faraday rotation,
$\mathsf{T}_i(\vec{\rho}, \vec{r_i})$	the atmospheric complex gain,
$\mathsf{K}_i(\vec{\rho}, \vec{r_i})$	the factored Fourier Transform kernel,
$\mathsf{B}_i = \mathsf{D}_i\mathsf{E}_i\mathsf{P}_i$	is the Total Voltage Pattern, in which
P_i	is the parallactic angle term,
$\mathsf{E}_i(\vec{\rho})$	the voltage primary beam, and
D_i	the leakage term.
$\mathbf{Y}_i$	is the commutation of *IF-channels*,
$\mathbf{H}_i$	the hybrid term for hybrid arrays, and
G_i	the electronic complex gain for the feeds only.

$\vec{\rho}$ and $\vec{r_i}$ describe the source and antenna positions respectively. It is important to note here that the $\mathbf{H}_i$ & $\mathbf{Y}_i$ matrices are not used in all systems.

Figure B.1: Effelsberg 100-m radio telescope in Germany (Credit: MPIfR).

Bibliography

Abell, G. O. (1958). "The Distribution of Rich Clusters of Galaxies." In: *Astrophysical Journal, Supplement* 3, p. 211. DOI: `10.1086/190036`.

Abell, G. O., H. G. Corwin Jr., and R. P. Olowin (1989). "A catalog of rich clusters of galaxies". In: *Astrophysical Journal, Supplement* 70, pp. 1–138. DOI: `10.1086/191333`.

Ackermann, M. et al. (2010). "GeV Gamma-ray Flux Upper Limits from Clusters of Galaxies". In: *Astrophysical Journal, Letters* 717, pp. L71–L78. DOI: `10.1088/2041-8205/717/1/L71`. arXiv: `1006.0748 [astro-ph.HE]`.

Akamatsu, H. and H. Kawahara (2013). "Systematic X-Ray Analysis of Radio Relic Clusters with Suzaku". In: *Publications of the ASJ* 65, 16, p. 16. DOI: `10.1093/pasj/65.1.16`. arXiv: `1112.3030`.

Akamatsu, H. et al. (2011). "X-Ray Study of the Outer Region of Abell 2142 with Suzaku". In: *Publications of the ASJ* 63, S1019–S1033. DOI: `10.1093/pasj/63.sp3.S1019`. arXiv: `1106.5653`.

Andrade-Santos, F. et al. (2017). "The Fraction of Cool-core Clusters in X-Ray versus SZ Samples Using Chandra Observations". In: *Astrophysical Journal* 843, 76, p. 76. DOI: `10.3847/1538-4357/aa7461`. arXiv: `1703.08690`.

Bacchi, M. et al. (2003). "Deep images of cluster radio halos". In: *Astronomy and Astrophysics* 400, pp. 465–476. DOI: `10.1051/0004-6361:20030044`.

Baier, F. W. et al. (1996). "Optical and X-ray structures of galaxy clusters. I". In: *Astronomische Nachrichten* 317, p. 77. DOI: `10.1002/asna.2113170202`.

Barré, H., H. Nye, and G. Janin (1999). "An overview of the XMM observatory system." In: *ESA Bulletin* 100, pp. 15–20.

Barrena, R. et al. (2007). "The dynamical status of the galaxy cluster Abell 115". In: *Astronomy and Astrophysics* 469, pp. 861–872. DOI: `10.1051/0004-6361:20077407`. arXiv: `0705.1444`.

Baum, S. A. and C. P. O'Dea (1991). "Multifrequency VLA observations of PKS 0745 - 191 - The archetypal 'cooling flow' radio source?" In: *Monthly Notices of the RAS* 250, pp. 737–749. DOI: `10.1093/mnras/250.4.737`.

Bautz, L. P. and W. W. Morgan (1970). “On the Classification of the Forms of Clusters of Galaxies”. In: *Astrophysical Journal, Letters* 162, p. L149. DOI: `10.1086/180643`.

Bautz, M. W. et al. (1996). “X-ray CCD calibration for the AXAF CCD Imaging Spectrometer”. In: *EUV, X-Ray, and Gamma-Ray Instrumentation for Astronomy VII*. Ed. by O. H. Siegmund and M. A. Gummin. Vol. 2808. Proceedings of the SPIE, pp. 170–181. DOI: `10.1117/12.255992`.

Bautz, M. W. et al. (1998). “X-ray CCD calibration for the AXAF CCD Imaging Spectrometer”. In: *X-Ray Optics, Instruments, and Missions*. Ed. by R. B. Hoover and A. B. Walker. Vol. 3444. Proceedings of the SPIE, pp. 210–224. DOI: `10.1117/12.331238`.

Beck, R. and M. Krause (2005). “Revised equipartition and minimum energy formula for magnetic field strength estimates from radio synchrotron observations”. In: *Astronomische Nachrichten* 326, pp. 414–427. DOI: `10.1002/asna.200510366`. eprint: `astro-ph/0507367`.

Beck, R. et al. (2003). “Systematic bias in interstellar magnetic field estimates”. In: *Astronomy and Astrophysics* 411, pp. 99–107. DOI: `10.1051/0004-6361:20031101`.

Beers, T. C., J. P. Huchra, and M. J. Geller (1983). “Galaxy clusters with multiple components. II - Abell 115”. In: *Astrophysical Journal* 264, pp. 356–363. DOI: `10.1086/160603`.

Bell, J. et al. (2000). “Software Radio Telescope: Interference Atlas and Mitigation Strategies”. In: *Perspectives on Radio Astronomy: Technologies for Large Antenna Arrays*. Ed. by A. B. Smolders and M. P. van Haarlem, p. 257.

Beygu, B., M. Hudaverdi, and N. Ercan (2009). “Binary Clusters Observed with XMM-Newton X-Ray Observatory”. In: *Publications de l’Observatoire Astronomique de Beograd* 86, pp. 117–123.

Blandford, R. and D. Eichler (1987). “Particle acceleration at astrophysical shocks: A theory of cosmic ray origin”. In: *Physics Reports* 154, pp. 1–75. DOI: `10.1016/0370-1573(87)90134-7`.

Blasi, P. and S. Colafrancesco (1999). “Cosmic rays, radio halos and nonthermal X-ray emission in clusters of galaxies”. In: *Astroparticle Physics* 12, pp. 169–183. DOI: `10.1016/S0927-6505(99)00079-1`. eprint: `astro-ph/9905122`.

Böhringer, H. et al. (2000). “The Northern ROSAT All-Sky (NORAS) Galaxy Cluster Survey. I. X-Ray Properties of Clusters Detected as Extended X-Ray Sources”. In: *Astrophysical Journal, Supplement* 129, pp. 435–474. DOI: `10.1086/313427`. eprint: `astro-ph/0003219`.

Böhringer, H. et al. (2001). “Harvesting the results from the REFLEX cluster survey: following-up on an ESO Key programme”. In: *The Messenger* 106, pp. 24–31.

Böhringer, H., G. Chon, and P. P. Kronberg (2016). “The Cosmic Large-Scale Structure in X-rays (CLASSIX) Cluster Survey. I. Probing galaxy cluster magnetic fields with line of sight rotation measures”. In: *Astronomy and Astrophysics* 596, A22, A22. DOI: `10.1051/0004-6361/201628873`. arXiv: `1610.02887`.

Bonafede, A. et al. (2009). “Revealing the magnetic field in a distant galaxy cluster: discovery of the complex radio emission from MACS J0717.5 +3745”. In: *Astronomy and Astrophysics* 503, pp. 707–720. DOI: `10.1051/0004-6361/200912520`. arXiv: `0905.3552`.

Bonafede, A. et al. (2010). “The Coma cluster magnetic field from Faraday rotation measures”. In: *Astronomy and Astrophysics* 513, A30, A30. DOI: `10.1051/0004-6361/200913696`. arXiv: `1002.0594`.

Bonafede, A. et al. (2012). “Discovery of radio haloes and double relics in distant MACS galaxy clusters: clues to the efficiency of particle acceleration”. In: *Monthly Notices of the RAS* 426, pp. 40–56. DOI: `10.1111/j.1365-2966.2012.21570.x`. arXiv: `1206.6102`.

Bonafede, A. et al. (2017). “On the absence of radio haloes in clusters with double relics”. In: *Monthly Notices of the RAS* 470, pp. 3465–3475. DOI: `10.1093/mnras/stx1475`. arXiv: `1706.04203`.

Botteon, A. et al. (2016). “A shock at the radio relic position in Abell 115”. In: *Monthly Notices of the RAS* 460, pp. L84–L88. DOI: `10.1093/mnrasl/slw082`. arXiv: `1604.07823 [astro-ph.HE]`.

Brentjens, M. A. and A. G. de Bruyn (2005). “Faraday rotation measure synthesis”. In: *Astronomy and Astrophysics* 441, pp. 1217–1228. DOI: `10.1051/0004-6361:20052990`. eprint: `astro-ph/0507349`.

Briggs, D. S. (1995). “High Fidelity Interferometric Imaging: Robust Weighting and NNLS Deconvolution”. In: *American Astronomical Society Meeting Abstracts*. Vol. 27. Bulletin of the American Astronomical Society, p. 1444.

Brown, S. and L. Rudnick (2009). “Diffuse Cluster-Like Radio Emission in Poor Environments”. In: *Astronomical Journal* 137, pp. 3158–3171. DOI: 10.1088/0004-6256/137/2/3158. arXiv: 0811.0205.

Brown, S., J. Duesterhoeft, and L. Rudnick (2011). “Multiple Shock Structures in a Radio-selected Cluster of Galaxies”. In: *Astrophysical Journal, Letters* 727, L25, p. L25. DOI: 10.1088/2041-8205/727/1/L25. arXiv: 1011.4985.

Brown, Shea and Lawrence Rudnick (2009). “Diffuse Cluster-Like Radio Emission in Poor Environments”. In: *The Astronomical Journal* 137.2, p. 3158. URL: http://stacks.iop.org/1538-3881/137/i=2/a=3158.

Brüggen, M. et al. (2012). “Magnetic Fields, Relativistic Particles, and Shock Waves in Cluster Outskirts”. In: *Space Science Reviews* 166, pp. 187–213. DOI: 10.1007/s11214-011-9785-9. arXiv: 1107.5223 [astro-ph.HE].

Brunetti, G. (2006). “Particle acceleration in galaxy clusters via MHD turbulence”. In: *Astronomische Nachrichten* 327, pp. 615–618. DOI: 10.1002/asna.200610604.

Brunetti, G. and T. W. Jones (2014). “Cosmic Rays in Galaxy Clusters and Their Nonthermal Emission”. In: *International Journal of Modern Physics D* 23, 1430007-98, pp. 1430007–98. DOI: 10.1142/S0218271814300079. arXiv: 1401.7519.

Brunetti, G. and A. Lazarian (2007). “Stochastic re-acceleration in the ICM”. In: *Highlights of Astronomy* 14, pp. 97–97. DOI: 10.1017/S1743921307009982.

– (2011). “Acceleration of primary and secondary particles in galaxy clusters by compressible MHD turbulence: from radio haloes to gamma-rays”. In: *Monthly Notices of the RAS* 410, pp. 127–142. DOI: 10.1111/j.1365-2966.2010.17457.x. arXiv: 1008.0184.

Brunetti, G., G. Setti, and A. Comastri (1997). “Inverse Compton X-rays from strong FRII radio-galaxies.” In: *Astronomy and Astrophysics* 325, pp. 898–910. eprint: astro-ph/9704162.

Brunetti, G. et al. (2001). “Particle reacceleration in the Coma cluster: radio properties and hard X-ray emission”. In: *Monthly Notices of the RAS* 320, pp. 365–378. DOI: 10.1046/j.1365-8711.2001.03978.x. eprint: astro-ph/0008518.

Brunetti, G. et al. (2004). “Alfvénic reacceleration of relativistic particles in galaxy clusters: MHD waves, leptons and hadrons”. In: *Monthly Notices of the RAS* 350, pp. 1174–1194. DOI: 10.1111/j.1365-2966.2004.07727.x. eprint: astro-ph/0312482.

Brunetti, G. et al. (2009). “On the evolution of giant radio halos and their connection with cluster mergers”. In: *Astronomy and Astrophysics* 507, pp. 661–669. DOI: `10.1051/0004-6361/200912751`. arXiv: `0909.2343`.

Brunetti, G. et al. (2012). “Probing the origin of giant radio haloes through radio and γ-ray data: the case of the Coma cluster”. In: *Monthly Notices of the RAS* 426, pp. 956–968. DOI: `10.1111/j.1365-2966.2012.21785.x`.

Buote, D. A. (2001). “On the Origin of Radio Halos in Galaxy Clusters”. In: *Astrophysical Journal, Letters* 553, pp. L15–L18. DOI: `10.1086/320500`. eprint: `astro-ph/0104211`.

Burke, B. F. and F. Graham-Smith (1997). “Book Review: An introduction to radio astronomy / Cambridge U Press, 1996 & 1997”. In: *Journal of the British Astronomical Association* 107, p. 222.

Burns, J. O. et al. (2017). “Banging Galaxy Clusters: High Fidelity X-ray Temperature and Radio Maps to Probe the Physics of Merging Clusters”. In: *American Astronomical Society Meeting Abstracts No.230*. Vol. 230. American Astronomical Society Meeting Abstracts, p. 310.02.

Byram, E. T., T. A. Chubb, and H. Friedman (1966). “Cosmic X-Ray Sources-Galactic and Extragalactic.” In: *Astronomical Journal* 71, p. 379. DOI: `10.1086/109934`.

Carilli, C. L. and G. B. Taylor (2002). “Cluster Magnetic Fields”. In: *Annual Review of Astronomy and Astrophysics* 40, pp. 319–348. DOI: `10.1146/annurev.astro.40.060401.093852`.

Cassano, R., G. Brunetti, and G. Setti (2006). “Statistics of giant radio haloes from electron reacceleration models”. In: *Monthly Notices of the RAS* 369, pp. 1577–1595. DOI: `10.1111/j.1365-2966.2006.10423.x`.

Cassano, R., M. Gitti, and G. Brunetti (2008). “A morphological comparison between giant radio halos and radio mini-halos in galaxy clusters”. In: *Astronomy and Astrophysics* 486, pp. L31–L34. DOI: `10.1051/0004-6361:200810179`. arXiv: `0806.1817`.

Cassano, R. et al. (2010). “On the Connection Between Giant Radio Halos and Cluster Mergers”. In: *Astrophysical Journal, Letters* 721, pp. L82–L85. DOI: `10.1088/2041-8205/721/2/L82`. arXiv: `1008.3624 [astro-ph.CO]`.

Cassano, R., G. Brunetti, and T. Venturi (2011). “The Connection between Radio Halos and Cluster Mergers and the Statistical Properties of the Radio Halo Population”. In: *Journal of Astrophysics and Astronomy* 32, pp. 519–527. DOI: `10.1007/s12036-011-9117-1`. arXiv: `1108.0291`.

Cassano, R. et al. (2013). “Revisiting Scaling Relations for Giant Radio Halos in Galaxy Clusters”. In: *Astrophysical Journal* 777, 141, p. 141. DOI: `10.1088/0004-637X/777/2/141`. arXiv: `1306.4379`.

Cavaliere, A. and R. Fusco-Femiano (1976). “X-rays from hot plasma in clusters of galaxies”. In: *Astronomy and Astrophysics* 49, pp. 137–144.

Chen, Y. et al. (2007). “Statistics of X-ray observables for the cooling-core and non-cooling core galaxy clusters”. In: *Astronomy and Astrophysics* 466, pp. 805–812. DOI: `10.1051/0004-6361:20066471`. eprint: `astro-ph/0702482`.

Chon, G., E. Puchwein, and H. Böhringer (2016). “The effect of AGN feedback on the X-ray morphologies of clusters: Simulations vs. observations”. In: *Astronomy and Astrophysics* 592, A46, A46. DOI: `10.1051/0004-6361/201628532`. arXiv: `1605.06661`.

Clarke, T. E. and T. A. Ensslin (2006). “Deep 1.4 GHz Very Large Array Observations of the Radio Halo and Relic in Abell 2256”. In: *Astronomical Journal* 131, pp. 2900–2912. DOI: `10.1086/504076`.

Clarke, T. E., P. P. Kronberg, and H. Böhringer (2001). “A New Radio-X-Ray Probe of Galaxy Cluster Magnetic Fields”. In: *Astrophysical Journal, Letters* 547, pp. L111–L114. DOI: `10.1086/318896`.

Cohen, A. S. and T. E. Clarke (2011). “An Ultra-steep-spectrum Radio Relic in the Galaxy Cluster A2443”. In: *Astronomical Journal* 141, 149, p. 149. DOI: `10.1088/0004-6256/141/5/149`. arXiv: `1102.4606`.

Condon, J. J. et al. (1998). “The NRAO VLA Sky Survey”. In: *Astronomical Journal* 115, pp. 1693–1716. DOI: `10.1086/300337`.

Cortese, L. et al. (2004). “Multiple merging in the Abell cluster 1367”. In: *Astronomy and Astrophysics* 425, pp. 429–441. DOI: `10.1051/0004-6361:20040381`. eprint: `astro-ph/0406367`.

Dallacasa, D. et al. (2009). “Deep 1.4 GHz Follow-up of the Steep Spectrum Radio Halo in A521”. In: *Astrophysical Journal* 699, pp. 1288–1292. DOI: `10.1088/0004-637X/699/2/1288`. arXiv: `0905.0588`.

de Chambure, D. et al. (1999). “XMM’s X-ray telescopes.” In: *ESA Bulletin* 100, pp. 30–42.

de Gasperin, F. et al. (2015). “A powerful double radio relic system discovered in PSZ1 G108.18-11.53: evidence for a shock with non-uniform Mach number?” In: *Monthly Notices of the RAS* 453, pp. 3483–3498. DOI: `10.1093/mnras/stv1873`. arXiv: `1508.02901 [astro-ph.HE]`.

de Gasperin, F. et al. (2018). “Systematic effects in LOFAR data: a unified calibration strategy”. In: *Astronomy and Astrophysics*, pp. 0000–0000. DOI: `xxxxxxxx`. arXiv: `0000-0000 [astro-ph.HE]`.

Delain, K. M. and L. Rudnick (2006). “Diffuse radio sources in groups and poor clusters”. In: *Astronomische Nachrichten* 327, p. 561. DOI: `10.1002/asna.200610588`. eprint: `astro-ph/0511110`.

Dennison, B. (1980). “Formation of radio halos in clusters of galaxies from cosmic-ray protons”. In: *Astrophysical Journal, Letters* 239, pp. L93–L96. DOI: `10.1086/183300`.

Dermer, C. D. (1986). “Secondary production of neutral pi-mesons and the diffuse galactic gamma radiation”. In: *Astronomy and Astrophysics* 157, pp. 223–229.

Dolag, K. and T. A. Enßlin (2000). “Radio halos of galaxy clusters from hadronic secondary electron injection in realistic magnetic field configurations”. In: *Astronomy and Astrophysics* 362, pp. 151–157.

Dolag, K. et al. (2001). “Correlation of the magnetic field and the intra-cluster gas density in galaxy clusters”. In: *Astronomy and Astrophysics* 378, pp. 777–786. DOI: `10.1051/0004-6361:20011219`.

Dolag, K., M. Bartelmann, and H. Lesch (2002). “Evolution and structure of magnetic fields in simulated galaxy clusters”. In: *Astronomy and Astrophysics* 387, pp. 383–395. DOI: `10.1051/0004-6361:20020241`.

Donnert, J. et al. (2010). “Radio haloes from simulations and hadronic models - II. The scaling relations of radio haloes”. In: *Monthly Notices of the RAS* 407, pp. 1565–1580. DOI: `10.1111/j.1365-2966.2010.17065.x`. arXiv: `1003.0336`.

Drabent, Alexander (2017). “Diffuse radio emission at low frequencies in merging galaxy clusters”. Dissertation, Friedrich-Schiller-Universität Jena, 2017. PhD thesis. Jena: Friedrich-Schiller-Universität Jena. URL: `https://www.db-thueringen.de/receive/dbt_mods_00032593`.

Drury, L. O. (1983). “An introduction to the theory of diffusive shock acceleration of energetic particles in tenuous plasmas”. In: *Reports on Progress in Physics* 46, pp. 973–1027. DOI: `10.1088/0034-4885/46/8/002`.

Dumba, C. et al. (2015). “Extended Diffuse Radio Emission in Abell 115”. In: *The Many Facets of Extragalactic Radio Surveys: Towards New Scientific Challenges*, p. 48.

Ebeling, H. et al. (1996). “Properties of the X-ray-brightest Abell-type clusters of galaxies (XBACs) from ROSAT All-Sky Survey data - I. The sample”. In: *Monthly Notices of the RAS* 281, pp. 799–829. DOI: 10.1093/mnras/281.3.799.

Ebeling, H., A. C. Edge, and J. P. Henry (2001). “MACS: A Quest for the Most Massive Galaxy Clusters in the Universe”. In: *Astrophysical Journal* 553, pp. 668–676. DOI: 10.1086/320958.

Ensslin, T. A. and P. L. Biermann (1998). “Limits on magnetic fields and relativistic electrons in the Coma cluster from multifrequency observations”. In: *Astronomy and Astrophysics* 330, pp. 90–96. eprint: astro-ph/9709232.

Enßlin, T. A. and M. Brüggen (2002). “On the formation of cluster radio relics”. In: *Monthly Notices of the RAS* 331, pp. 1011–1019. DOI: 10.1046/j.1365-8711.2002.05261.x.

Enßlin, T. A. and Gopal-Krishna (2001). “Reviving fossil radio plasma in clusters of galaxies by adiabatic compression in environmental shock waves”. In: *Astronomy and Astrophysics* 366, pp. 26–34. DOI: 10.1051/0004-6361:20000198. eprint: astro-ph/0011123.

Ettori, S. (2000). “β-model and cooling flows in X-ray clusters of galaxies”. In: *Monthly Notices of the RAS* 318, pp. 1041–1046. DOI: 10.1046/j.1365-8711.2000.03664.x. eprint: astro-ph/0005224.

Evrard, A. E. and I. M. Gioia (2002). “Clusters, Cosmology and Mergers”. In: *Merging Processes in Galaxy Clusters*. Ed. by L. Feretti, I. M. Gioia, and G. Giovannini. Vol. 272. Astrophysics and Space Science Library, pp. 253–304. DOI: 10.1007/0-306-48096-4_9.

Fanaroff, B. L. and J. M. Riley (1974). “The morphology of extragalactic radio sources of high and low luminosity”. In: *Monthly Notices of the RAS* 167, 31P–36P. DOI: 10.1093/mnras/167.1.31P.

Farnsworth, D. et al. (2013). “Discovery of Megaparsec-scale, Low Surface Brightness Nonthermal Emission in Merging Galaxy Clusters Using the Green Bank Telescope”. In: *Astrophysical Journal* 779, 189, p. 189. DOI: 10.1088/0004-637X/779/2/189. arXiv: 1311.3313.

Felten, J. E. et al. (1966). “X-Rays from the Coma Cluster of Galaxies”. In: *Astrophysical Journal* 146, pp. 955–958. DOI: 10.1086/148972.

Feretti, L. et al. (1995). “The magnetic field in the Coma cluster.” In: *Astronomy and Astrophysics* 302, p. 680.

Feretti, L. et al. (1998). "Electron ageing and polarization in tailed radio galaxies". In: *Astronomy and Astrophysics* 331, pp. 475–484. eprint: `astro-ph/9712041`.

Feretti, L. et al. (2012). "Clusters of galaxies: observational properties of the diffuse radio emission". In: *Astronomy and Astrophysics Reviews* 20, 54, p. 54. DOI: `10.1007/s00159-012-0054-z`. arXiv: `1205.1919`.

Ferrari, C. et al. (2008). "Observations of Extended Radio Emission in Clusters". In: *Space Science Reviews* 134, pp. 93–118. DOI: `10.1007/s11214-008-9311-x`. arXiv: `0801.0985`.

Finoguenov, A. et al. (2010). "XMM-Newton Observation of the Northwest Radio Relic Region in A3667". In: *Astrophysical Journal* 715, pp. 1143–1151. DOI: `10.1088/0004-637X/715/2/1143`. arXiv: `1004.2331`.

Forman, W. et al. (1981). "Einstein imaging observations of clusters with a bimodal mass distribution". In: *Astrophysical Journal, Letters* 243, pp. L133–L136. DOI: `10.1086/183459`.

Forman, W. R. (2017). "Anatomy of a Merger: A Deep Chandra Observation of Abell 115". In: *AAS/High Energy Astrophysics Division No.16*. Vol. 16. AAS/High Energy Astrophysics Division, p. 105.17.

Fruscione, A. et al. (2006). "CIAO: Chandra's data analysis system". In: *Society of Photo-Optical Instrumentation Engineers (SPIE) Conference Series*. Vol. 6270. Proceedings of the SPIE, p. 62701V. DOI: `10.1117/12.671760`.

Fujita, Y., M. Takizawa, and C. L. Sarazin (2003). "Nonthermal Emissions from Particles Accelerated by Turbulence in Clusters of Galaxies". In: *Astrophysical Journal* 584, pp. 190–202. DOI: `10.1086/345599`. eprint: `astro-ph/0210320`.

Fusco-Femiano, R. et al. (1999). "Hard X-Ray Radiation in the Coma Cluster Spectrum". In: *Astrophysical Journal, Letters* 513, pp. L21–L24. DOI: `10.1086/311902`.

Gabici, S. and P. Blasi (2003). "Nonthermal Radiation from Clusters of Galaxies: The Role of Merger Shocks in Particle Acceleration". In: *Astrophysical Journal* 583, pp. 695–705. DOI: `10.1086/345429`.

Gabriel, C. (2017). "XMM-Newton Science Analysis System (SAS): medium and long term strategy". In: *The X-ray Universe 2017*. Ed. by J.-U. Ness and S. Migliari, p. 84.

Gabriel, C. et al. (2006). “The Scientific Analysis System (SAS) and its Evolution Through the Different Stages of the XMM-Newton Project”. In: *IAU Special Session* 6, no.13, no.13.

Garmire, G. P. (1999). “Early Science Results from the ACIS on Board the Chandra X-ray Observatory”. In: *American Astronomical Society Meeting Abstracts*. Vol. 31. Bulletin of the American Astronomical Society, p. 1515.

Garmire, G. P. et al. (1986). “The AXAF CCD imaging spectrometer”. In: *X-ray instrumentation in astronomy*. Ed. by J. L. Culhane. Vol. 597. Proceedings of the SPIE, pp. 261–266. DOI: `10.1117/12.966590`.

Gasperin, Francesco de et al. (2017). “Gentle reenergization of electrons in merging galaxy clusters”. In: *Science Advances* 3.10. DOI: `10.1126/sciadv.1701634`. eprint: `http://advances.sciencemag.org/content/3/10/e1701634.full.pdf`. URL: `http://advances.sciencemag.org/content/3/10/e1701634`.

Gavazzi, G. and W. Jaffe (1987). “50 KPC radio trails behind irregular galaxies in A1367”. In: *Astronomy and Astrophysics* 186, p. L1.

Gavazzi, G. and G. Trinchieri (1983). “Radio and X-ray observations of the radio halo source in A1367”. In: *Astrophysical Journal* 270, pp. 410–416. DOI: `10.1086/161134`.

Geller, M. J. and T. C. Beers (1983). “Substructure in Clusters of Galaxies”. In: *Early Evolution of the Universe and its Present Structure*. Ed. by G. O. Abell and G. Chincarini. Vol. 104. IAU Symposium, p. 231.

Ghizzardi, S., M. Rossetti, and S. Molendi (2010). “Cold fronts in galaxy clusters”. In: *Astronomy and Astrophysics* 516, A32, A32. DOI: `10.1051/0004-6361/200912496`. arXiv: `1003.1051`.

Giacconi, R. et al. (1972). “The Uhuru catalog of X-ray sources.” In: *Astrophysical Journal* 178, pp. 281–308. DOI: `10.1086/151790`.

Giacintucci, S. et al. (2008). “Shock acceleration as origin of the radio relic in A 521?” In: *Astronomy and Astrophysics* 486, pp. 347–358. DOI: `10.1051/0004-6361:200809459`. arXiv: `0803.4127`.

Gioia, I. M. et al. (1990). “The Einstein Observatory Extended Medium-Sensitivity Survey. I - X-ray data and analysis”. In: *Astrophysical Journal, Supplement* 72, pp. 567–619. DOI: `10.1086/191426`.

Giovannini, G. et al. (1993). “The halo radio source Coma C and the origin of halo sources”. In: *Astrophysical Journal* 406, pp. 399–406. DOI: `10.1086/172451`.

Giovannini, G., M. Tordi, and L. Feretti (1999). “Radio halo and relic candidates from the NRAO VLA Sky Survey”. In: *New Astronomy* 4, pp. 141–155. DOI: `10.1016/S1384-1076(99)00018-4`.

Giovannini, G. et al. (2009). “Radio halos in nearby (z < 0.4) clusters of galaxies”. In: *Astronomy and Astrophysics* 507, pp. 1257–1270. DOI: `10.1051/0004-6361/200912667`. arXiv: `0909.0911`.

Giovannini, G. et al. (2011). “A giant radio halo in the low luminosity X-ray cluster Abell 523”. In: *Astronomy and Astrophysics* 530, L5, p. L5. DOI: `10.1051/0004-6361/201116930`. arXiv: `1104.3711`.

Gitti, M., G. Brunetti, and G. Setti (2002). “Reacceleration of Relativistic Electrons in Cooling Flows: the Case of Perseus Cluster”. In: *Tracing Cosmic Evolution with Galaxy Clusters*. Ed. by S. Borgani, M. Mezzetti, and R. Valdarnini. Vol. 268. Astronomical Society of the Pacific Conference Series, p. 373.

Gitti, M. et al. (2004). “Particle acceleration in cooling flow clusters of galaxies: The case of Abell 2626”. In: *Astronomy and Astrophysics* 417, pp. 1–11. DOI: `10.1051/0004-6361:20031750`. eprint: `astro-ph/0311275`.

Gitti, M. et al. (2011). “A Chandra Study of the Large-scale Shock and Cool Filaments in Hydra A: Evidence for Substantial Gas Dredge-up by the Central Outburst”. In: *Astrophysical Journal* 732, 13, p. 13. DOI: `10.1088/0004-637X/732/1/13`. arXiv: `1102.5397`.

Govoni, F. and L. Feretti (2004). “Magnetic Fields in Clusters of Galaxies”. In: *International Journal of Modern Physics D* 13, pp. 1549–1594. DOI: `10.1142/S0218271804005080`.

Govoni, F. et al. (2001). “Radio and X-ray diffuse emission in six clusters of galaxies”. In: *Astronomy and Astrophysics* 376, pp. 803–819. DOI: `10.1051/0004-6361:20011016`. eprint: `astro-ph/0107275`.

Govoni, F. et al. (2005). “A2255: The first detection of filamentary polarized emission in a radio halo”. In: *Astronomy and Astrophysics* 430, pp. L5–L8. DOI: `10.1051/0004-6361:200400113`. eprint: `astro-ph/0411720`.

Gregorini, L. and M. Bondi (1989). “High resolution observations of the narrow angle tail radio galaxy in Abell 115”. In: *Astronomy and Astrophysics* 225, pp. 333–340.

Gursky, H. et al. (1971). “A Strong X-Ray Source in the Coma Cluster Observed by UHURU”. In: *Astrophysical Journal, Letters* 167, p. L81. DOI: `10.1086/180765`.

Gursky, H. et al. (1972). “X-Ray Emission from Rich Clusters of Galaxies”. In: *Astrophysical Journal, Letters* 173, p. L99. DOI: `10.1086/180926`.

Hachenberg, O., B.-H. Grahl, and R. Wielebinski (1973). “The 100-meter radio telescope at Effelsberg.” In: *IEEE Proceedings* 61, pp. 1288–1295.

Hallman, E. J. et al. (2018). “Probing the Curious Case of a Galaxy Cluster Merger in Abell 115 with High-fidelity Chandra X-Ray Temperature and Radio Maps”. In: *Astrophysical Journal* 859, 44, p. 44. DOI: `10.3847/1538-4357/aabf3a`. arXiv: `1804.06493`.

Hamaker, J. P. (2000). “Understanding radio polarimetry. IV. The full-coherency analogue of scalar self-calibration: Self-alignment, dynamic range and polarimetric fidelity”. In: *Astronomy and Astrophysics, Supplement* 143, pp. 515–534. DOI: `10.1051/aas:2000337`.

– (2006). “Understanding radio polarimetry. V. Making matrix self-calibration work: processing of a simulated observation”. In: *Astronomy and Astrophysics* 456, pp. 395–404. DOI: `10.1051/0004-6361:20065145`.

Hamaker, J. P., J. D. Bregman, and R. J. Sault (1996). “Understanding radio polarimetry. I. Mathematical foundations.” In: *Astronomy and Astrophysics, Supplement* 117, pp. 137–147.

Harris, D. E. (1980). “A review of extragalactic non-thermal sources”. In: *Journal of the RAS of Canada* 74, pp. 109–133.

Harrower, G. A. (1962). “Design of radio telescopes for extragalactic surveys”. In: *Canadian Journal of Physics* 40, pp. 226–236. DOI: `10.1139/p62-021`.

Hill, G. J. et al. (2008). “The Hobby-Eberly Telescope Dark Energy Experiment (HETDEX): Description and Early Pilot Survey Results”. In: *Panoramic Views of Galaxy Formation and Evolution*. Ed. by T. Kodama, T. Yamada, and K. Aoki. Vol. 399. Astronomical Society of the Pacific Conference Series, p. 115. arXiv: `0806.0183`.

Hoang, D. N. et al. (2017). “Deep LOFAR observations of the merging galaxy cluster CIZA J2242.8+5301”. In: *Monthly Notices of the RAS* 471, pp. 1107–1125. DOI: `10.1093/mnras/stx1645`.

Hoang, D. N. et al. (2018). “Radio observations of the double-relic galaxy cluster Abell 1240”. In: *Monthly Notices of the RAS*. DOI: `10.1093/mnras/sty1123`.

Hoeft, M. and M. Brüggen (2007). “Radio signature of cosmological structure formation shocks”. In: *Monthly Notices of the RAS* 375, pp. 77–91. DOI: `10.1111/j.1365-2966.2006.11111.x`. eprint: `astro-ph/0609831`.

Hoeft, M. et al. (2008). “Diffuse radio emission from clusters in the MareNostrum Universe simulation”. In: *Monthly Notices of the RAS* 391, pp. 1511–1526. DOI: `10.1111/j.1365-2966.2008.13955.x`. arXiv: `0807.1266`.

Högbom, J. A. (1974). “Aperture Synthesis with a Non-Regular Distribution of Interferometer Baselines”. In: *Astronomy and Astrophysics, Supplement* 15, p. 417.

Hudson, D. S. et al. (2010). “What is a cool-core cluster? a detailed analysis of the cores of the X-ray flux-limited HIFLUGCS cluster sample”. In: *Astronomy and Astrophysics* 513, A37, A37. DOI: `10.1051/0004-6361/200912377`. arXiv: `0911.0409`.

Jaffe, W. J. (1977). “Origin and transport of electrons in the halo radio source in the Coma cluster”. In: *Astrophysical Journal* 212, pp. 1–7. DOI: `10.1086/155011`.

Jansen, F. et al. (2001). “XMM-Newton observatory. I. The spacecraft and operations”. In: *Astronomy and Astrophysics* 365, pp. L1–L6. DOI: `10.1051/0004-6361:20000036`.

Jeltema, T. E. and Fermi LAT Collaboration (2010). “Fermi-LAT Observations of Clusters of Galaxies”. In: *AAS/High Energy Astrophysics Division #11*. Vol. 42. Bulletin of the American Astronomical Society, p. 703.

Jeltema, T. E. and S. Profumo (2011). “Implications of Fermi Observations For Hadronic Models of Radio Halos in Clusters of Galaxies”. In: *Astrophysical Journal* 728, 53, p. 53. DOI: `10.1088/0004-637X/728/1/53`. arXiv: `1006.1648`.

Jeltema, T. E. et al. (2005). “The Evolution of Structure in X-Ray Clusters of Galaxies”. In: *Astrophysical Journal* 624, pp. 606–629. DOI: `10.1086/428940`. eprint: `astro-ph/0501360`.

Jenkins, A. et al. (1998). “Evolution of Structure in Cold Dark Matter Universes”. In: *Astrophysical Journal* 499, pp. 20–40. DOI: `10.1086/305615`.

Johnston-Hollitt, M. et al. (2002). “The Dual Radio Relics of A3667”. In: *The Universe at Low Radio Frequencies*. Ed. by A. Pramesh Rao, G. Swarup, and Gopal-Krishna. Vol. 199. IAU Symposium, p. 157.

Jones, F. C. and D. C. Ellison (1991). “The plasma physics of shock acceleration”. In: *Space Science Reviews* 58, pp. 259–346. DOI: `10.1007/BF01206003`.

Kale, R. et al. (2013). “The Extended GMRT Radio Halo Survey. I. New upper limits on radio halos and mini-halos”. In: *Astronomy and Astrophysics* 557, A99, A99. DOI: `10.1051/0004-6361/201321515`. arXiv: `1306.3102`.

Kale, R. et al. (2015). “The Extended GMRT Radio Halo Survey. II. Further results and analysis of the full sample”. In: *Astronomy and Astrophysics* 579, A92, A92. DOI: `10.1051/0004-6361/201525695`. arXiv: `1503.02415`.

Kang, H. and T. W. Jones (2007). “Self-similar evolution of cosmic-ray-modified quasi-parallel plane shocks”. In: *Astroparticle Physics* 28, pp. 232–246. DOI: `10.1016/j.astropartphys.2007.05.007`. arXiv: `0705.3274`.

Kang, H. and D. Ryu (2011). “Cosmic ray spectrum from diffusive shock acceleration”. In: *Astrophysics and Space Science* 336, pp. 263–268. DOI: `10.1007/s10509-011-0709-7`.

Kempner, J. C. et al. (2004). “Conference Note: A Taxonomy of Extended Radio Sources in Clusters of Galaxies”. In: *The Riddle of Cooling Flows in Galaxies and Clusters of galaxies*. Ed. by T. Reiprich, J. Kempner, and N. Soker. eprint: `astro-ph/0310263`.

Kierdorf, M. et al. (2017). “Relics in galaxy clusters at high radio frequencies”. In: *Astronomy and Astrophysics* 600, A18, A18. DOI: `10.1051/0004-6361/201629570`. arXiv: `1612.01764`.

Kim, K.-T. et al. (1990). “The halo and magnetic field of the Coma cluster of galaxies”. In: *Astrophysical Journal* 355, pp. 29–37. DOI: `10.1086/168737`.

Kim, K.-T., P. C. Tribble, and P. P. Kronberg (1991). “Detection of excess rotation measure due to intracluster magnetic fields in clusters of galaxies”. In: *Astrophysical Journal* 379, pp. 80–88. DOI: `10.1086/170484`.

Kim, M. et al. (2018). “Mapping the Dark Matter Distribution of the Merging Galaxy Cluster Abell 115”. In: *American Astronomical Society Meeting Abstracts No.231*. Vol. 231. American Astronomical Society Meeting Abstracts, no.252.03.

Koester, B. P. et al. (2007). “A MaxBCG Catalog of 13,823 Galaxy Clusters from the Sloan Digital Sky Survey”. In: *Astrophysical Journal* 660, pp. 239–255. DOI: `10.1086/509599`. eprint: `astro-ph/0701265`.

Kolokotronis, V. et al. (2001). “Searching for cluster substructure using APM and ROSAT data”. In: *Monthly Notices of the RAS* 320, pp. 49–60. DOI: `10.1046/j.1365-8711.2001.03924.x`. eprint: `astro-ph/0002432`.

Kraus, J. D. (1956). “Radio telescope designs of large aperture and low cost”. In: *Astronomical Journal* 61, p. 169. DOI: `10.1086/107302`.

Krivonos, R. A. et al. (2003). “A Possible Shock Wave in the Intergalactic Medium of the Cluster of Galaxies A754”. In: *Astronomy Letters* 29, pp. 425–428. DOI: `10.1134/1.1589859`.

Krymskii, G. F. (1977). “A regular mechanism for the acceleration of charged particles on the front of a shock wave”. In: *Akademiia Nauk SSSR Doklady* 234, pp. 1306–1308.

Lazarian, A. (2006). “Theoretical approaches to particle propagation and acceleration in turbulent intergalactic medium”. In: *Astronomische Nachrichten* 327, p. 609. DOI: `10.1002/asna.200610603`.

Legg, T. H. (1998). “A proposed new design for a large radio telescope”. In: *Astronomy and Astrophysics, Supplement* 130, pp. 369–379. DOI: `10.1051/aas:1998230`.

Liang, H. et al. (2000). “A Powerful Radio Halo in the Hottest Known Cluster of Galaxies 1E 0657-56”. In: *Astrophysical Journal* 544, pp. 686–701. DOI: `10.1086/317223`.

Longair, M. S. (1981). *High energy astrophysics.*

Lumb, D. H. and A. D. Holland (1988). “Event recognition techniques in CCD X-ray detectors for astronomy”. In: *Nuclear Instruments and Methods in Physics Research A* 273, pp. 696–700. DOI: `10.1016/0168-9002(88)90081-2`.

Markevitch, M. et al. (2000). “Chandra Observation of Abell 2142: Survival of Dense Subcluster Cores in a Merger”. In: *Astrophysical Journal* 541, pp. 542–549. DOI: `10.1086/309470`. eprint: `astro-ph/0001269`.

Markevitch, M. et al. (2002). “A Textbook Example of a Bow Shock in the Merging Galaxy Cluster 1E 0657-56”. In: *Astrophysical Journal, Letters* 567, pp. L27–L31. DOI: `10.1086/339619`. eprint: `astro-ph/0110468`.

Markevitch, M. et al. (2005). “Bow Shock and Radio Halo in the Merging Cluster A520”. In: *Astrophysical Journal* 627, pp. 733–738. DOI: `10.1086/430695`. eprint: `astro-ph/0412451`.

McMullin, J. P. et al. (2007). “CASA Architecture and Applications”. In: *Astronomical Data Analysis Software and Systems XVI.* Ed. by R. A. Shaw, F. Hill, and D. J. Bell. Vol. 376. Astronomical Society of the Pacific Conference Series, p. 127.

Miley, G. K. et al. (1972). “Active Galaxies with Radio Trails in Clusters”. In: Nature 237, pp. 269–272. DOI: `10.1038/237269a0`.

Miniati, F. (2002). “Intergalactic shock acceleration and the cosmic gamma-ray background”. In: *Monthly Notices of the RAS* 337, pp. 199–208. DOI: `10.1046/j.1365-8711.2002.05903.x`. eprint: `astro-ph/0203014`.

Miniati, F. et al. (2001). “Cosmic-Ray Electrons in Groups and Clusters of Galaxies: Primary and Secondary Populations from a Numerical Cosmological Simulation”. In: *Astrophysical Journal* 562, pp. 233–253. DOI: `10.1086/323434`.

Mohr, J. J. et al. (1995). “Cosmological Constraints from Observed Cluster X-Ray Morphologies”. In: *Astrophysical Journal* 447, p. 8. DOI: `10.1086/175852`. eprint: `astro-ph/9501011`.

Mol, Jan David and John W. Romein (2011). “The LOFAR Beam Former: Implementation and Performance Analysis”. In: *Proceedings of the 17th International Conference on Parallel Processing - Volume Part II*. Euro-Par’11. Bordeaux, France: Springer-Verlag, pp. 328–339. ISBN: 978-3-642-23396-8. URL: `http://dl.acm.org/citation.cfm?id=2033408.2033448`.

Molendi, S. and F. Pizzolato (2001). “Is the Gas in Cooling Flows Multiphase?” In: *Astrophysical Journal* 560, pp. 194–200. DOI: `10.1086/322387`.

Morandi, A. et al. (2015). “The galaxy cluster outskirts probed by Chandra”. In: *Monthly Notices of the RAS* 450, pp. 2261–2278. DOI: `10.1093/mnras/stv660`. arXiv: `1501.04095`.

Müller, P. et al. (2017). “The NOD3 software package: A graphical user interface-supported reduction package for single-dish radio continuum and polarisation observations”. In: *Astronomy and Astrophysics* 606, A41, A41. DOI: `10.1051/0004-6361/201731257`. arXiv: `1707.05573 [astro-ph.IM]`.

“Effelsberg Radio Telescope” (2000). In: *Encyclopedia of Astronomy and Astrophysics*. Ed. by P. Murdin, p. 4191. DOI: `10.1888/0333750888/4191`.

Napier, P. J., A. R. Thompson, and R. D. Ekers (1983). “The Very Large Array - Design and performance of a modern synthesis radio telescope”. In: *IEEE Proceedings* 71, pp. 1295–1320.

Offringa, A. R. (2010). *AOFlagger: RFI Software*. Astrophysics Source Code Library. ascl: `1010.017`.

Offringa, A. R. and O. Smirnov (2017). “An optimized algorithm for multiscale wideband deconvolution of radio astronomical images”. In: *Monthly Notices of the RAS* 471.1, pp. 301–316. DOI: `10.1093/mnras/stx1547`.

Offringa, A. R., J. J. van de Gronde, and J. B. T. M. Roerdink (2012). “A morphological algorithm for improving radio-frequency interference detection”. In: *Astronomy and Astrophysics* 539, A95, A95. DOI: `10.1051/0004-6361/201118497`. arXiv: `1201.3364 [astro-ph.IM]`.

Offringa, A. R., B. McKinley, Hurley-Walker, et al. (2014). “WSClean: an implementation of a fast, generic wide-field imager for radio astronomy”. In: *Monthly Notices of the RAS* 444.1, pp. 606–619. DOI: `10.1093/mnras/stu1368`.

Ogrean, G. et al. (2016). “No Shock Across Part of a Radio Relic?” In: *American Astronomical Society Meeting Abstracts #228*. Vol. 228. American Astronomical Society Meeting Abstracts, p. 110.03.

O’Hara, T. B. et al. (2006). “Effects of Mergers and Core Structure on the Bulk Properties of Nearby Galaxy Clusters”. In: *Astrophysical Journal* 639, pp. 64–80. DOI: `10.1086/499327`. eprint: `astro-ph/0510064`.

Okabe, A., ed. (2000). *Spatial tessellations : concepts and applications of voronoi diagrams*.

Okabe, N. et al. (2010). “LoCuSS: Calibrating Mass-observable Scaling Relations for Cluster Cosmology with Subaru Weak-lensing Observations”. In: *Astrophysical Journal* 721, pp. 875–885. DOI: `10.1088/0004-637X/721/1/875`. arXiv: `1007.3816`.

Owen, F. N., J. A. Eilek, and N. E. Kassim (2000). “M87 at 90 Centimeters: A Different Picture”. In: *Astrophysical Journal* 543, pp. 611–619. DOI: `10.1086/317151`. eprint: `astro-ph/0006150`.

Parekh, V. et al. (2015). “Morphology parameters: substructure identification in X-ray galaxy clusters”. In: *Astronomy and Astrophysics* 575, A127, A127. DOI: `10.1051/0004-6361/201424123`. arXiv: `1411.6525`.

Pearce, C. J. J. et al. (2017). “VLA Radio Observations of the HST Frontier Fields Cluster Abell 2744: The Discovery of New Radio Relics”. In: *Astrophysical Journal* 845, 81, p. 81. DOI: `10.3847/1538-4357/aa7e2f`.

Peebles, P. J. E. (1970). “Structure of the Coma Cluster of Galaxies”. In: *Astronomical Journal* 75, p. 13. DOI: `10.1086/110933`.

– (1993). “The Mass Puzzle in Cosmology”. In: *American Astronomical Society Meeting Abstracts #182*. Vol. 25. Bulletin of the American Astronomical Society, p. 896.

Perley, R. A. and B. J. Butler (2013). “An Accurate Flux Density Scale from 1 to 50 GHz”. In: *Astrophysical Journal, Supplement* 204, 19, p. 19. DOI: 10.1088/0067-0049/204/2/19. arXiv: 1211.1300 [astro-ph.IM].

Petrosian, V. (2001). “On the Nonthermal Emission and Acceleration of Electrons in Coma and Other Clusters of Galaxies”. In: *Astrophysical Journal* 557, pp. 560–572. DOI: 10.1086/321557. eprint: astro-ph/0101145.

Pfrommer, C. and L. J. Dursi (2010). “Detecting the orientation of magnetic fields in galaxy clusters”. In: *Nature Physics* 6, pp. 520–526. DOI: 10.1038/nphys1657. arXiv: 0911.2476.

Pfrommer, C. and T. A. Enßlin (2004). “Constraining the population of cosmic ray protons in cooling flow clusters with γ-ray and radio observations: Are radio mini-halos of hadronic origin?” In: *Astronomy and Astrophysics* 413, pp. 17–36. DOI: 10.1051/0004-6361:20031464.

Pfrommer, C., T. A. Enßlin, and V. Springel (2008). “Simulating cosmic rays in clusters of galaxies - II. A unified scheme for radio haloes and relics with predictions of the γ-ray emission”. In: *Monthly Notices of the RAS* 385, pp. 1211–1241. DOI: 10.1111/j.1365-2966.2008.12956.x. arXiv: 0707.1707.

Piffaretti, R. et al. (2011). “The MCXC: a meta-catalogue of x-ray detected clusters of galaxies”. In: *Astronomy and Astrophysics* 534, A109, A109. DOI: 10.1051/0004-6361/201015377. arXiv: 1007.1916.

Pizzo, R. F. et al. (2011). “Deep multi-frequency rotation measure tomography of the galaxy cluster A2255”. In: *Astronomy and Astrophysics* 525, A104, A104. DOI: 10.1051/0004-6361/201014158. arXiv: 1008.3530.

Planck Collaboration et al. (2014a). “Planck 2013 results. XXIX. The Planck catalogue of Sunyaev-Zel’dovich sources”. In: *Astronomy and Astrophysics* 571, A29, A29. DOI: 10.1051/0004-6361/201321523. arXiv: 1303.5089.

Planck Collaboration et al. (2014b). “Planck 2013 results. XXVI. Background geometry and topology of the Universe”. In: *Astronomy and Astrophysics* 571, A26, A26. DOI: 10.1051/0004-6361/201321546. arXiv: 1303.5086.

Planck Collaboration et al. (2015). “Planck intermediate results. XXVII. High-redshift infrared galaxy overdensity candidates and lensed sources discovered by Planck and confirmed by Herschel-SPIRE”. In: *Astronomy and Astrophysics* 582, A30, A30. DOI: 10.1051/0004-6361/201424790. arXiv: 1503.08773.

Plummer, D. A. and S. Subramanian (2001). “The Chandra Automatic Data Processing Infrastructure”. In: *Astronomical Data Analysis Software and Systems X*. Ed. by F. R. Harnden Jr., F. A. Primini, and H. E. Payne. Vol. 238. Astronomical Society of the Pacific Conference Series, p. 475.

Popesso, P. et al. (2004). “RASS-SDSS Galaxy clusters survey. I. The catalog and the correlation of X-ray and optical properties”. In: *Astronomy and Astrophysics* 423, pp. 449–467. DOI: `10.1051/0004-6361:20035818`. eprint: `astro-ph/0403354`.

Rajiva, S. (1999). “Chandra X-ray observatory (AXAF) - NASA’s most powerful X-ray space telescope”. In: *Bulletin of the Astronomical Society of India* 27, p. 231.

Rajpurohit, K. et al. (2018). “Deep VLA Observations of the Cluster 1RXS J0603.3+4214 in the Frequency Range of 1-2 GHz”. In: *Astrophysical Journal* 852, 65, p. 65. DOI: `10.3847/1538-4357/aa9f13`. arXiv: `1712.01327`.

Rajpurohit, Kamlesh (2018). “Diffuse radio emission and magnetic fields in galaxy clusters”. Dissertation, Friedrich-Schiller-Universität Jena, 2018. PhD thesis. Jena. DOI: `10.22032/dbt.35127`. URL: `https://www.db-thueringen.de/receive/dbt_mods_00035127`.

Rakos, K. D. et al. (2000). “Cluster Populations in A115 and A2283”. In: *Astrophysical Journal* 540, pp. 715–725. DOI: `10.1086/309344`. eprint: `astro-ph/0004346`.

Rasia, E., M. Meneghetti, and S. Ettori (2013). “X-ray Morphological Estimators for Galaxy Clusters”. In: *The Astronomical Review* 8.1, pp. 40–70. DOI: `10.1080/21672857.2013.11519713`. arXiv: `1211.7040 [astro-ph.CO]`.

Reimer, O. et al. (2003). “EGRET Upper Limits on the High-Energy Gamma-Ray Emission of Galaxy Clusters”. In: *Astrophysical Journal* 588, pp. 155–164. DOI: `10.1086/374046`.

Röttgering, H. (2003). “LOFAR, a new low frequency radio telescope”. In: *New Astronomy Review* 47, pp. 405–409. DOI: `10.1016/S1387-6473(03)00057-5`. eprint: `astro-ph/0309537`.

Rottgering, H. J. A. et al. (1997). “The extended radio emission in the luminous X-ray cluster A3667”. In: *Monthly Notices of the RAS* 290, pp. 577–584. DOI: `10.1093/mnras/290.4.577`.

Roy, J. et al. (2010). “A real-time software backend for the GMRT”. In: *Experimental Astronomy* 28, pp. 25–60. DOI: `10.1007/s10686-010-9187-0`. arXiv: `0910.1517 [astro-ph.IM]`.

Rozo, E. et al. (2015). “redMaPPer - III. A detailed comparison of the Planck 2013 and SDSS DR8 redMaPPer cluster catalogues”. In: *Monthly Notices of the RAS* 450, pp. 592–605. DOI: `10.1093/mnras/stv605`. arXiv: `1401.7716`.

Rudnick, L. and J. A. Lemmerman (2009). “An Objective Survey of Mpc-scale Radio Emission in 0.03 < z < 0.3 Bright X-ray Clusters”. In: *Astrophysical Journal* 697, pp. 1341–1357. DOI: `10.1088/0004-637X/697/2/1341`. arXiv: `0903.0335 [astro-ph.CO]`.

Rudnick, L. and F. N. Owen (1976). “Head-tail radio sources in clusters of galaxies”. In: *Astrophysical Journal, Letters* 203, pp. L107–L111. DOI: `10.1086/182030`.

Rudnick, L., K. M. Delain, and J. A. Lemmerman (2006). “Unbiased studies of diffuse extragalactic radio sources”. In: *Astronomische Nachrichten* 327, p. 549. DOI: `10.1002/asna.200610585`. eprint: `astro-ph/0511113`.

Russel, H. (2010). “Two shock fronts in the merging cluster Abell 2146”. In: *Galaxy Clusters: Observations, Physics and Cosmology*, p. 25.

Ryu, D. and H. Kang (2003). “Clusters of Galaxies: Shock Waves and Cosmic Rays”. In: *Journal of Korean Astronomical Society* 36, pp. 105–110. DOI: `10.5303/JKAS.2003.36.3.105`. eprint: `astro-ph/0211365`.

Ryu, D. et al. (2008). “Turbulence and Magnetic Fields in the Large-Scale Structure of the Universe”. In: *Science* 320, p. 909. DOI: `10.1126/science.1154923`. arXiv: `0805.2466`.

Sanders, J. S., A. C. Fabian, and R. J. H. Dunn (2005). “Non-thermal X-rays, a high-abundance ridge and fossil bubbles in the core of the Perseus cluster of galaxies”. In: *Monthly Notices of the RAS* 360, pp. 133–140. DOI: `10.1111/j.1365-2966.2005.09016.x`.

Santos, J. S. et al. (2008). “Searching for cool core clusters at high redshift”. In: *Astronomy and Astrophysics* 483, pp. 35–47. DOI: `10.1051/0004-6361:20078815`. arXiv: `0802.1445`.

Sarazin, C. L. (1986). “X-ray emission from clusters of galaxies”. In: *Reviews of Modern Physics* 58, pp. 1–115. DOI: `10.1103/RevModPhys.58.1`.

– (1999). “The Energy Spectrum of Primary Cosmic-Ray Electrons in Clusters of Galaxies and Inverse Compton Emission”. In: *Astrophysical Journal* 520, pp. 529–547. DOI: `10.1086/307501`. eprint: `astro-ph/9901061`.

– (2002). “The Physics of Cluster Mergers”. In: *Merging Processes in Galaxy Clusters*. Ed. by L. Feretti, I. M. Gioia, and G. Giovannini. Vol. 272. Astrophysics and Space Science Library, pp. 1–38. DOI: `10.1007/0-306-48096-4_1`. eprint: `astro-ph/0105418`.

Sault, R. J., J. P. Hamaker, and J. D. Bregman (1996). “Understanding radio polarimetry. II. Instrumental calibration of an interferometer array.” In: *Astronomy and Astrophysics, Supplement* 117, pp. 149–159.

Scaife, A. M. M. and G. H. Heald (2012). “A broad-band flux scale for low-frequency radio telescopes”. In: *Monthly Notices of the RAS* 423, pp. L30–L34. DOI: `10.1111/j.1745-3933.2012.01251.x`. arXiv: `1203.0977 [astro-ph.IM]`.

Schade, D. et al. (1995). “Canada-France Redshift Survey: Hubble Space Telescope Imaging of High-Redshift Field Galaxies”. In: *Astrophysical Journal, Letters* 451, p. L1. DOI: `10.1086/309677`. eprint: `astro-ph/9507028`.

Schlickeiser, R., A. Sievers, and H. Thiemann (1987). “The diffuse radio emission from the Coma cluster”. In: *Astronomy and Astrophysics* 182, pp. 21–35.

Sclocco, A. et al. (2012). “Radio Astronomy Beam Forming on Many-Core Architectures”. In: *2012 IEEE 26th International Parallel and Distributed Processing Symposium*, pp. 1105–1116. DOI: `10.1109/IPDPS.2012.102`.

Semler, D. R. et al. (2012). “High-redshift Cool-core Galaxy Clusters Detected via the Sunyaev-Zel’dovich Effect in the South Pole Telescope Survey”. In: *Astrophysical Journal* 761, 183, p. 183. DOI: `10.1088/0004-637X/761/2/183`. arXiv: `1208.3368 [astro-ph.CO]`.

Senechal, M. (1993). “Mathematical Structures. (Book Reviews: Spatial Tessellations. Concepts and Applications of Voronoi Diagrams.)” In: *Science* 260, p. 1170. DOI: `10.1126/science.260.5111.1170`.

Shibata, R. et al. (1999). “Temperature Variation in the Cluster of Galaxies Abell 115 Studied with ASCA”. In: *Astrophysical Journal* 524, pp. 603–611. DOI: `10.1086/307819`. eprint: `astro-ph/9906357`.

Shimwell, T. W. et al. (2017). “The LOFAR Two-metre Sky Survey. I. Survey description and preliminary data release”. In: *Astronomy and Astrophysics* 598, A104, A104. DOI: `10.1051/0004-6361/201629313`.

Sijbring, L. G. (1993). *A radio continuum and HI line study of the perseus cluster.*

Slee, O. B. et al. (2001). “Four Extreme Relic Radio Sources in Clusters of Galaxies”. In: *Astronomical Journal* 122, pp. 1172–1193. DOI: 10.1086/322105.

Springel, V. et al. (2005). “Simulations of the formation, evolution and clustering of galaxies and quasars”. In: *Nature* 435, pp. 629–636. DOI: 10.1038/nature03597. eprint: astro-ph/0504097.

Staniszewski, Z. et al. (2009). “Galaxy Clusters Discovered with a Sunyaev-Zel’dovich Effect Survey”. In: *Astrophysical Journal* 701, pp. 32–41. DOI: 10.1088/0004-637X/701/1/32. arXiv: 0810.1578.

Stroe, A. et al. (2013). “Discovery of spectral curvature in the shock downstream region: CIZA J2242.8+5301”. In: *Astronomy and Astrophysics* 555, A110, A110. DOI: 10.1051/0004-6361/201321267. arXiv: 1305.0005.

Stroe, A. et al. (2016). “The widest frequency radio relic spectra: observations from 150 MHz to 30 GHz”. In: *Monthly Notices of the RAS* 455, pp. 2402–2416. DOI: 10.1093/mnras/stv2472. arXiv: 1510.06739.

Struble, M. F. and H. J. Rood (1999). “A Compilation of Redshifts and Velocity Dispersions for ACO Clusters”. In: *Astrophysical Journal, Supplement* 125, pp. 35–71. DOI: 10.1086/313274.

Subrahmanyan, R. et al. (2003). “PKS B1400-33: An Unusual Radio Relic in a Poor Cluster”. In: *Astronomical Journal* 125, pp. 1095–1106. DOI: 10.1086/367797. eprint: astro-ph/0212154.

Subramanian, K., A. Shukurov, and N. E. L. Haugen (2006). “Evolving turbulence and magnetic fields in galaxy clusters”. In: *Monthly Notices of the RAS* 366, pp. 1437–1454. DOI: 10.1111/j.1365-2966.2006.09918.x.

Sunyaev, R. A. and Y. B. Zel’dovich (1972). “The Observations of Relic Radiation as a Test of the Nature of X-Ray Radiation from the Clusters of Galaxies”. In: *Comments on Astrophysics and Space Physics* 4, p. 173.

Suwa, T. et al. (2003). “Cluster Morphology as a Test of Different Cosmological Models”. In: *Astrophysical Journal* 588, pp. 7–17. DOI: 10.1086/368375. eprint: astro-ph/0108308.

Swarup, G. (1990). “Giant metrewave radio telescope (GMRT) - Scientific objectives and design aspects”. In: *Indian Journal of Radio and Space Physics* 19, pp. 493–505.

Thierbach, M., U. Klein, and R. Wielebinski (2003). “The diffuse radio emission from the Coma cluster at 2.675 GHz and 4.85 GHz”. In: *Astronomy and*

Astrophysics 397, pp. 53–61. DOI: 10.1051/0004-6361:20021474. eprint: astro-ph/0210147.

Tribble, P. C. (1993). “Radio haloes, cluster mergers, and cooling flows”. In: *Monthly Notices of the RAS* 263, pp. 31–36. DOI: 10.1093/mnras/263.1.31.

Tucker, W. et al. (1998). “1E 0657-56: A Contender for the Hottest Known Cluster of Galaxies”. In: *Astrophysical Journal, Letters* 496, pp. L5–L8. DOI: 10.1086/311234.

V. Cappellen, W. a., S. J. Wijnholds, and J. D. Bregman (2006). “Sparse antenna array configurations in large aperture synthesis radio telescopes”. In: *2006 European Radar Conference*, pp. 76–79. DOI: 10.1109/EURAD.2006.280277.

Vacca, V. et al. (2012). “The intracluster magnetic field power spectrum in A2199”. In: *Astronomy and Astrophysics* 540, A38, A38. DOI: 10.1051/0004-6361/201116622.

Valentijn, E. A. (1979). “Evidence of an intra cluster medium in the Hercules supercluster”. In: *Astronomy and Astrophysics* 78, pp. 362–366.

Vallee, J. P. (1990). “Detecting the largest magnets - The universe and the clusters of galaxies”. In: *Astrophysical Journal* 360, pp. 1–6. DOI: 10.1086/169089.

van Diepen, G. and T. J. Dijkema (2018). *DPPP: Default Pre-Processing Pipeline*. Astrophysics Source Code Library. ascl: 1804.003.

van Haarlem, M. P. et al. (2013). “LOFAR: The LOw-Frequency ARray”. In: *Astronomy and Astrophysics* 556, A2, A2. DOI: 10.1051/0004-6361/201220873. arXiv: 1305.3550 [astro-ph.IM].

van Weeren, R. J. et al. (2009). “Radio observations of ZwCl 2341.1+0000: a double radio relic cluster”. In: *Astronomy and Astrophysics* 506, pp. 1083–1094. DOI: 10.1051/0004-6361/200912287.

van Weeren, R. J. et al. (2010). “Particle Acceleration on Megaparsec Scales in a Merging Galaxy Cluster”. In: *Science* 330, p. 347. DOI: 10.1126/science.1194293. arXiv: 1010.4306 [astro-ph.CO].

van Weeren, R. J. et al. (2011). “Radio continuum observations of new radio halos and relics from the NVSS and WENSS surveys. Relic orientations, cluster X-ray luminosity, and redshift distributions”. In: *Astronomy and Astrophysics* 533, A35, A35. DOI: 10.1051/0004-6361/201117149. arXiv: 1107.5597.

van Weeren, R. J. et al. (2012a). “Diffuse radio emission in MACS J1752.0+4440”. In: *Monthly Notices of the RAS* 425, pp. L36–L40. DOI: `10.1111/j.1745-3933.2012.01301.x`.

van Weeren, R. J. et al. (2012b). “The “toothbrush-relic”: evidence for a coherent linear 2-Mpc scale shock wave in a massive merging galaxy cluster?” In: *Astronomy and Astrophysics* 546, A124, A124. DOI: `10.1051/0004-6361/201219000`. arXiv: `1209.2196`.

van Weeren, R. J. et al. (2016). “LOFAR Facet Calibration”. In: *Astrophysical Journal, Supplement* 223, 2, p. 2. DOI: `10.3847/0067-0049/223/1/2`. arXiv: `1601.05422 [astro-ph.IM]`.

Vazza, F. and M. Brüggen (2014). “Do radio relics challenge diffusive shock acceleration?” In: *Monthly Notices of the RAS* 437, pp. 2291–2296. DOI: `10.1093/mnras/stt2042`. arXiv: `1310.5707`.

Vazza, F., G. Brunetti, and C. Gheller (2009a). “Shock waves in Eulerian cosmological simulations: main properties and acceleration of cosmic rays”. In: *Monthly Notices of the RAS* 395, pp. 1333–1354. DOI: `10.1111/j.1365-2966.2009.14691.x`. arXiv: `0808.0609`.

Vazza, F. et al. (2009b). “Turbulent motions and shocks waves in galaxy clusters simulated with adaptive mesh refinement”. In: *Astronomy and Astrophysics* 504, pp. 33–43. DOI: `10.1051/0004-6361/200912535`. arXiv: `0905.3169`.

Vazza, F. et al. (2012). “Why are central radio relics so rare?” In: *Monthly Notices of the RAS* 421, pp. 1868–1873. DOI: `10.1111/j.1365-2966.2011.20160.x`. arXiv: `1111.1720`.

Vazza, F. et al. (2015). “Electron and proton acceleration efficiency by merger shocks in galaxy clusters”. In: *Monthly Notices of the RAS* 451, pp. 2198–2211. DOI: `10.1093/mnras/stv1072`. arXiv: `1505.02782 [astro-ph.HE]`.

Vazza, F. et al. (2016). “Constraining the efficiency of cosmic ray acceleration by cluster shocks”. In: *Monthly Notices of the RAS* 459, pp. 70–83. DOI: `10.1093/mnras/stw584`. arXiv: `1603.02688`.

Venturi, T. et al. (2007). “GMRT radio halo survey in galaxy clusters at z = 0.2-0.4. I. The REFLEX sub-sample”. In: *Astronomy and Astrophysics* 463, pp. 937–947. DOI: `10.1051/0004-6361:20065961`. eprint: `astro-ph/0610271`.

Venturi, T. et al. (2008). “GMRT radio halo survey in galaxy clusters at z = 0.2-0.4. II. The eBCS clusters and analysis of the complete sample”. In: *Astronomy* *and Astrophysics* 484, pp. 327–340. DOI: 10.1051/0004-6361:200809622. arXiv: 0803.4084.

Vikhlinin, A. et al. (2005). "Chandra Temperature Profiles for a Sample of Nearby Relaxed Galaxy Clusters". In: *Astrophysical Journal* 628, pp. 655–672. DOI: 10.1086/431142. eprint: astro-ph/0412306.

Voges, W. (1992). "Scientific Results from the ROSAT All-Sky X-Ray Survey". In: *European Southern Observatory Conference and Workshop Proceedings*. Ed. by A. Heck and F. Murtagh. Vol. 43. European Southern Observatory Conference and Workshop Proceedings, p. 139.

Weisskopf, M. C. (1999). "The Chandra X-Ray Observatory - Overview and Status". In: *American Astronomical Society Meeting Abstracts*. Vol. 31. Bulletin of the American Astronomical Society, p. 1514.

Weißmann, A. et al. (2013). "Studying the properties of galaxy cluster morphology estimators". In: *Astronomy and Astrophysics* 549, A19, A19. DOI: 10.1051/0004-6361/201219333. arXiv: 1210.6445 [astro-ph.CO].

Wielebinski, R., N. Junkes, and B. H. Grahl (2011). "The Effelsberg 100-m Radio Telescope: Construction and Forty Years of Radio Astronomy". In: *Journal of Astronomical History and Heritage* 14, pp. 3–21.

Williams, W. L. et al. (2016). "LOFAR 150-MHz observations of the Boötes field: catalogue and source counts". In: *Monthly Notices of the RAS* 460, pp. 2385–2412. DOI: 10.1093/mnras/stw1056. arXiv: 1605.01531.

Willson, M. A. G. (1970). "Radio observations of the cluster of galaxies in Coma Berenices - the 5C4 survey." In: *Monthly Notices of the RAS* 151, pp. 1–44. DOI: 10.1093/mnras/151.1.1.

Wright, E. L. (2006). "A Cosmology Calculator for the World Wide Web". In: *Publications of the ASP* 118, pp. 1711–1715. DOI: 10.1086/510102. eprint: astro-ph/0609593.

Yang, D. et al. (2003). "Design of a 50-m pulsar radio telescope". In: *Millimeter and Submillimeter Detectors for Astronomy*. Ed. by T. G. Phillips and J. Zmuidzinas. Vol. 4855. Proceedings of the SPIE, pp. 528–539. DOI: 10.1117/12.459174.